2005-03-18

# Phase Locked Flow Measurements of Steady and Unsteady Vortex Generator Jets in a Separating Boundary Layer

Laura C. Hansen
*Brigham Young University - Provo*

# PHASE LOCKED FLOW MEASUREMENTS OF STEADY AND UNSTEADY VORTEX GENERATOR JETS IN A SEPARATING BOUNDARY LAYER

by

Laura Hansen

A thesis submitted to the faculty of

Brigham Young University

in partial fulfillment of the requirements for the degree of

Master of Science

Department of Mechanical Engineering

Brigham Young University

April 2005

BRIGHAM YOUNG UNIVERSITY

GRADUATE COMMITTEE APPROVAL

of a thesis submitted by

Laura Hansen

This thesis has been read by each member of the following graduate committee and by majority vote has been found to be satisfactory.

| | |
|---|---|
| Date | Jeffrey P. Bons, Chair |
| Date | R. Daniel Maynes |
| Date | Brent W. Webb |

BRIGHAM YOUNG UNIVERSITY

As chair of the candidate's graduate committee, I have read the thesis of Laura Hansen in its final form and have found that (1) its format, citations, and bibliographical style are consistent and acceptable and fulfill university and department style requirements; (2) its illustrative materials including figures, tables, and charts are in place; and (3) the final manuscript is satisfactory to the graduate committee and is ready for submission to the university library.

_____ _____

Date

Jeffrey P. Bons
Chair, Graduate Committee

Accepted for the Department

_____

Matthew R. Jones
Graduate Coordinator

Accepted for the College

_____

Douglas M. Chabries
Dean, Ira A. Fulton College of Engineering and Technology

ABSTRACT

PHASE LOCKED FLOW MEASUREMENTS OF STEADY
AND UNSTEADY VORTEX GENERATOR JETS
IN A SEPARATING BOUNDARY LAYER

Laura Hansen

Department of Mechanical Engineering

Master of Science

Vortex generator jets (VGJs) have been found to be an effective method of active separation control on the suction side of a low pressure turbine (LPT) blade at low Reynolds numbers. The flow mechanisms responsible for this control were studied and documented in order to provide a basis for future improvements in LPT design. Data were collected using a stereo PIV system that enabled all three components of velocity to be measured.

Steady VGJs were injected into a laminar boundary layer on a flat plate (non-separating boundary layer) in order to more fully understand the characteristics and behavior of the produced vortices. Both normal (injected normal to the wall) and angled (injected at 30° pitch and 90° skew angles to the freestream) jets were studied. The steady jets were found to create vortices that swept the low momentum fluid up from the

boundary layer while transporting high momentum freestream fluid towards the wall, a phenomenon that provides the ingredients for flow control.

Pulsed VGJs were then injected on a flat plate with an applied adverse pressure gradient equivalent to that experienced by a commonly tested LPT blade. This configuration was used to study the effectiveness of the flow control exhibited by both normal and angled jets on a separating boundary layer. Time averaged results showed similar boundary layer separation reduction for both normal and angled jets; however, individual characteristics suggested that the control mechanism of the two injection angles is distinct.

Steady and pulsed VGJs were then applied to a new aggressive LPT blade design to explore the effect of the jets on a separating boundary layer along the curved blade surface. Steady injection provided flow control through freestream entrainment, while pulsed jets created a two-dimensional, spanwise disturbance that reduced the separated area as it traveled downstream. A detailed fluid analysis of the uncontrolled flow around the blade was performed in order to identify the separation and reattachment points and the area of transition. This information was used as a basis for comparison with the VGJ cases to determine flow control effectiveness.

# ACKNOWLEDGEMENTS

The research conducted for this thesis would not have been possible without the support of several others. The sponsorship of the Air Force Office of Scientific Research, with Dr. Thomas Beutner as contract manager, is gratefully acknowledged. Thanks to Dr. Steven Anderson of LaVision, Inc. for his instruction on using the PIV system; to Richard Eldredge for his preliminary research that led to mine; to Kevin Cole and Robert Perry for their help constructing the research facility; and to my friends Ken Engan, Dan Reimann, Matt Bloxham, and Dave Olson for their hard work in the machine shop. The new blade design was available to me through the efforts of John Clark, Peter Koch, and Rolf Sondergaard at the Wright-Patterson Air Force Base in Dayton, Ohio. And of course, special thanks to my advisor Dr. Jeffrey Bons, for his patient guidance and wise counsel that enabled me to succeed.

TABLE OF CONTENTS

LIST OF FIGURES

NOMENCLATURE

| | | |
|---|---|---|
| $B$ | = | jet blowing ratio ($U_j/U_e$) |
| $c_p$ | = | pressure coefficient [Eq. 1] |
| $c_x$ | = | axial chord [m] |
| $d$ | = | jet hole diameter |
| $f$ | = | forcing frequency [Hz] |
| $F^+$ | = | dimensionless forcing frequency ($f/(U_e/L_{ss})$) |
| H | = | shape factor |
| $L$ | = | plate length [m] |
| $L_{ss}$ | = | suction surface length [m] |
| $P$ | = | pressure [Pa] |
| $Re_{cx}$ | = | inlet Reynolds number ($\rho U_i c_x/\mu$) |
| $Re_{Lss}$ | = | exit Reynolds number ($\rho U_e L_{ss}/\mu$) |
| $Re_\theta$ | = | momentum thickness Reynolds number ($\rho U_\infty \theta/\mu$) |
| $T$ | = | forcing period [s] |
| $\|V\|$ | = | velocity magnitude [m/s] |
| $t$ | = | time [s] |
| $u$ | = | streamwise velocity [m/s] |
| $u'$ | = | turbulent fluctuating component of velocity [Eq. 6] |
| $v$ | = | wall-normal velocity [m/s] |
| $w$ | = | spanwise velocity [m/s] |
| $x$ | = | streamwise direction |
| $y$ | = | wall normal direction |
| $z$ | = | spanwise direction |
| $\delta$ | = | boundary layer thickness [m] |
| $\delta^*$ | = | boundary layer displacement thickness [Eq. 4] |
| $\phi$ | = | integrated wake pressure loss coefficient [Eq. 2] |
| $\Gamma$ | = | integrated boundary layer momentum flux loss coefficient [Eq. 3] |
| $\mu$ | = | dynamic viscosity [kg/m·s] |
| $\theta$ | = | boundary layer momentum thickness [Eq. 5] |
| $\rho$ | = | density [$kg/m^3$] |
| $\omega$ | = | vorticity [1/s] |

subscripts

| | | |
|---|---|---|
| *avg* | = | average |
| *e* | = | local boundary layer edge |
| *ex* | = | tunnel exit |
| *ext* | = | extrapolated |
| *in* | = | tunnel inlet |
| *j* | = | jet |

| | | |
|---|---|---|
| *max* | = | maximum |
| *o* | = | uncontrolled (B = 0 case) |
| *s* | = | static |
| *ss* | = | suction surface |
| *tot* | = | total |
| *w* | = | wake |

# 1. INTRODUCTION

## 1.1. Background

Low pressure turbine (LPT) blades must be carefully designed in order to perform well under demanding operating conditions. They require a very aggressive turning angle (Figure 1-1a) to provide maximum power during take-off and sufficient power for auxiliary systems during flight. At very high altitudes, the flight Reynolds number drops significantly, which can produce a laminar boundary layer along the surface of the blade. This laminar boundary layer is susceptible to separation, a condition that greatly diminishes the efficiency of the turbine (Figure 1-1b). For example, Sharma et al.[1] reported an increase in blade loss coefficient of 300% as a result of the boundary layer separation.

Much research has been conducted in an effort to find a method of reducing the laminar boundary layer separation in LPTs. Lake et al.[2] determined that a modification of the actual blade surface (for example, by adding dimples) successfully decreased the separation-induced losses. Volino[3] experimented with 2D spanwise bars that act as boundary layer trips and thus prevent suction surface separation. However, passive methods of flow control such as these may inhibit proper turbine performance at design conditions and/or increase blade heat transfer. Active methods of flow control, although

more difficult to implement, are preferred as they can be adapted in-flight according to the current flight conditions.

One such method of active flow control is the use of vortex generator jets (VGJs) to inject a small amount of airflow into the separating boundary layer (Figure 1-1c). It has been suggested that VGJs cause the separated boundary layer to reattach by mixing high momentum freestream fluid with low momentum boundary layer fluid[4]. This process of freestream entrainment effectively reenergizes the flow and reduces the incurred losses. For example, Sondergaard et al.[5] determined that the use of VGJs reduced the separation induced wake losses by up to 60%. However, before VGJs can be successfully implemented in LPT design, a more thorough understanding of the physical mechanisms involved in the reduction of the boundary layer must be obtained.

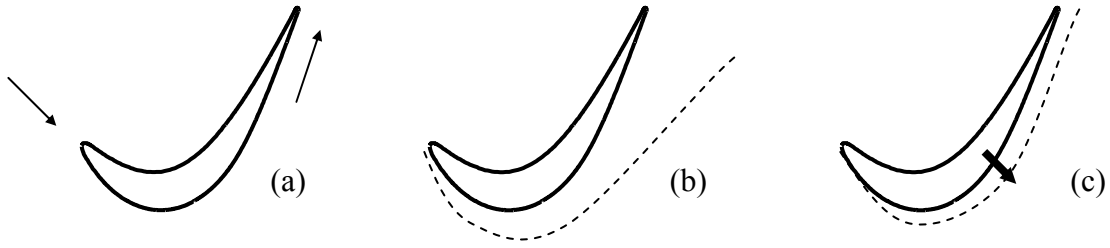


**Figure 1-1**. Air flow around a turbine blade: (a) turning angle, (b) separated boundary layer, (c) attached boundary layer with VGJ

Khan and Johnston[6] studied the growth of the vortex itself, by injecting steady jets at various orientations into a turbulent boundary layer. They noted the development of the vortex, and its effect on the surrounding boundary layer fluid. The vortical motion caused by the jet fluid produced a thickening of the boundary layer on the upwash side of the vortex, with a corresponding thinning of the boundary layer on the opposite side

Eldredge and Bons[7] also performed detailed flow measurements of steady VGJs. They investigated the effects of VGJs on both separating and non-separating boundary layers on a flat plate and a scaled LPT blade. They likewise reported the development of streamwise vortices and measured their movement and downstream decay. They determined that the streamwise vortex was the dominant characteristic of the flow, lending validity to the freestream entrainment theory.

This result is corroborated by the detailed flow measurements of Johari and Rixon[8] for steady jet injection into a turbulent boundary layer. Though their experiments were conducted without a freestream pressure gradient (and thus without separation), streamwise vortices are clearly evident.

The flow control benefits of VGJs can be improved by pulsing the jet air as it is introduced into the flow domain. A pulsed jet requires only a small fraction of the mass flow required for steady jet injection, which greatly reduces the amount of air that must be redirected from the compressor. Thus, the use of pulsed jets can reduce the overall losses of the entire turbine engine.

Johari and Rixon[9] performed studies of pulsed VGJs introduced into a turbulent boundary layer on a flat plate. They compared the development and strength of the vortex created by the pulsed jet to their previous steady jet measurements. They determined that the streamwise vortices were weaker and located farther out in the boundary layer than those created by steady jets.

The study of Bons et al.[10] on a LPT blade showed that pulsed VGJs produced a comparable reduction in boundary layer separation while employing only a small fraction of the mass flow necessary for steady flow VGJS. They further determined that the

control of the boundary layer was due to the mechanism associated with the starting and ending of the jet pulse rather than the jet fluid itself. This suggests that separation can be reduced not only through freestream entrainment, but also as a result of the disturbance caused by a pulsed jet.

Complementary to these experimental studies are the time-accurate CFD calculations performed by Postl et al.[11,12] They explored the effects of both steady and pulsed VGJs introduced on a flat wall with the proper applied streamwise pressure gradient as well as on the same blade profile studied by Bons et al.[10,13] Their results suggest that the mechanisms responsible for reattachment are distinct for the steady and pulsed jets. Steady VGJs were shown to reduce separation by momentum entrainment of the streamwise vortices. It was found, however, that the pulsed VGJs tripped the flow to turbulent, and introduced a two-dimensional, spanwise, unsteady wave into the flow.

Postl et al.[11,12] also studied the effect of the jet injection angle. They suggested that for the steady VGJs a skewed injection angle of 90º to the freestream flow (with low pitch angle) was more effective than the normal injection since it increases freestream entrainment. However, for pulsed VGJs the opposite was found to be true since normal jets were more effective in the formation of spanwise vorticity than angled jets (for the same blowing ratio).

Although extensive research has been conducted on the mechanisms involved in steady VGJ flow control, and analytical studies have been performed on pulsed VGJs, there are still many unanswered questions. For instance, Bons et al.[13] documented the effect of reducing the duty cycle of jet forcing and discovered a considerable phase lag in the relaxation of the suction surface boundary layer as it returned to its separated state.

The fluid mechanics responsible for this are as yet unclear. Volino[14] also studied the effect of oscillating (synthetic) VGJs on boundary layer separation and observed the presence of streamwise vortices. In addition, Volino suggested that the disturbance caused by these vortices resembled turbulent spots, as the leading edge of the disturbance traveled faster than the trailing edge. A calmed region that was resistant to separation followed the disturbance. Thus, the different roles of boundary layer transition and freestream entrainment must still be sorted out. As such, more detailed flow analyses are necessary to establish a basis for future analytical models for LPT design.

## 1.2. Objective

The objective of this research is to provide the needed detailed flow analysis of the effects of steady and pulsed vortex generator jets on boundary layer separation. The more thorough understanding of the physical mechanisms responsible for the flow control gleaned from this research will allow for better analytical models in future LPT designs.

# 2. EXPERIMENTAL FACILITY

## 2.1. Wind Tunnel

A new wind tunnel was constructed to enable data collection for this research. It was built according to the specifications outlined by Reshotko et al.[15] to ensure proper flow uniformity and development. The tunnel is an open loop wind tunnel operated by a centrifugal blower with a capacity of 3 kg/s. A heat exchanger regulates the temperature, maintaining a constant air temperature in the tunnel. The air travels through a 9m long, 0.67m diameter duct before entering the plenum. The plenum is 1.83m long with a diameter of 1.07m and is designed to straighten the flow. It contains a perforated plate and a 76.2mm wide honeycomb (both with 6.35mm diameter holes), followed by 2 coarse and 3 fine screens. A foam nozzle, formed to a $5^{th}$ order polynomial provides the transition from the plenum to the acrylic duct. This configuration (shown below in Figure 2-1) conditions the air, providing a flow uniformity of ±2% and background freestream turbulence levels below 0.3%. The acrylic duct has a square cross section with a side dimension of 0.381m and a length of 1.83m. The modular wind tunnel construction allows the streamwise pressure gradient and wall curvature to be independently varied.

Three separate test sections were used in this research to explore the effectiveness of VGJ flow control. First, VGJs were injected into a laminar boundary layer on a flat plate with no pressure gradient (Figure 2-2). The relative simplicity of this flow allowed

for a better characterization of the development and movement of the jet vortices. Then, a wedge was inserted into the same flat plate configuration in order to apply a streamwise

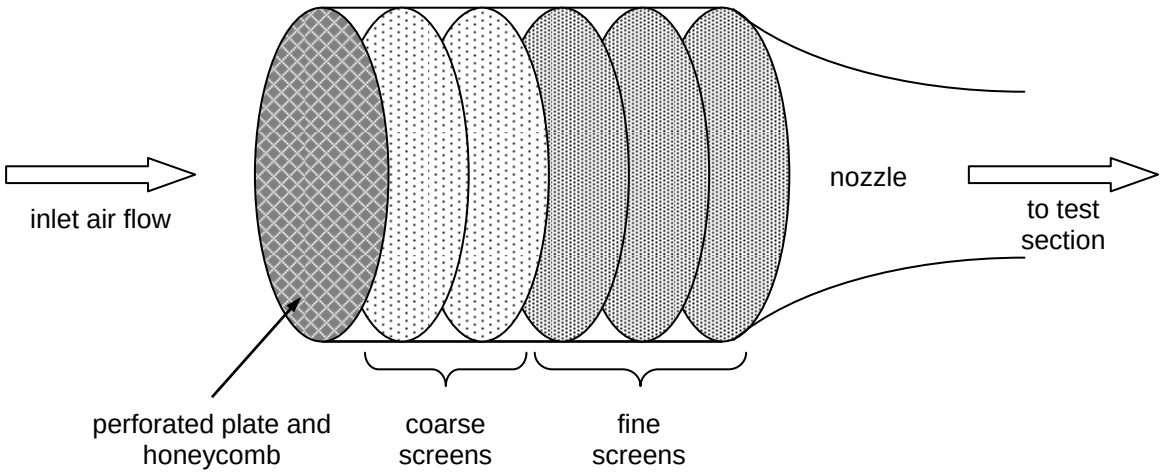


**Figure 2-1**. Schematic of the wind tunnel plenum.

pressure gradient comparable to that experienced by LPT blades (Figure 2-3). The adverse pressure gradient imposed by the wedge on the downstream half of the flat plate produced conditions susceptible to boundary layer separation. Thus, unlike the flat plate, this configuration enabled the previously determined vortex behavior to be used to study its effect on a separating boundary layer. Finally, a three-blade cascade was produced to observe the flow control on a Reynolds number-scaled LPT blade (Figure 2-5). The blade cascade included the additional complexity of surface curvature in addition to an adverse pressure gradient.

### 2.1.1. Flat Plate (Zero Pressure Gradient)

Figure 2-2 shows the flat plate test section. A boundary layer bleed is employed at the leading edge to create a new, laminar boundary layer. A row of 4mm diameter cylindrical holes was created to introduce the VGJs; vertical holes aligned normal to the freestream direction, and angled holes with 30º pitch and 90º skew angles. These angles were shown by Johnston[4] to be in the range where VGJs are most effective in reducing flow separation. The holes are placed approximately 10 diameters apart at 0.36m from the boundary layer bleed. The holes were drilled through a 2cm thick acrylic sheet and have a length-to-diameter ratio of 5 and 10 for the normal and angled holes, respectively.

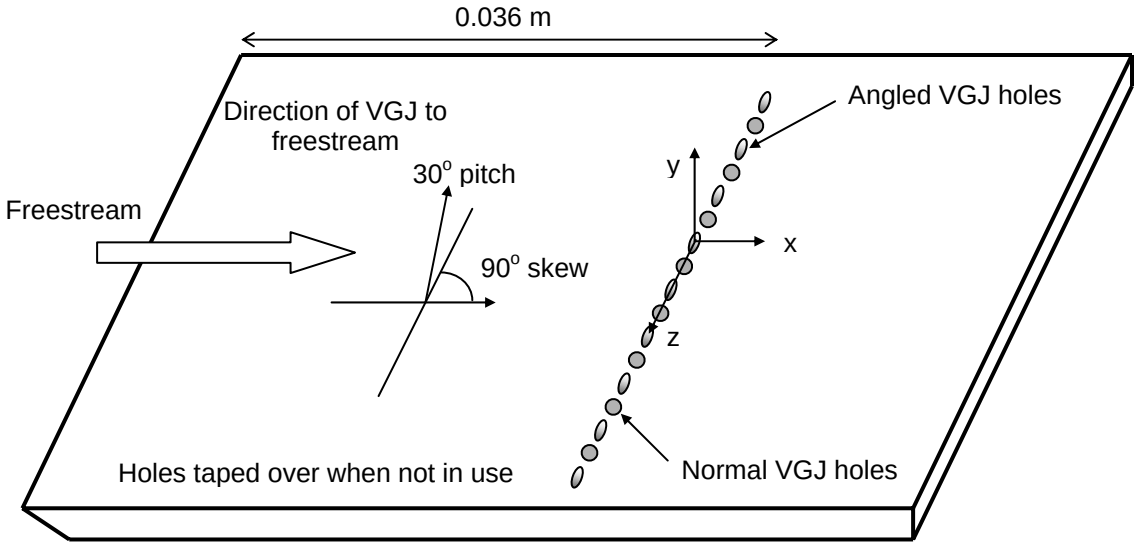


**Figure 2-2**. Flat plate test section schematic

### 2.1.2. Flat Plate with Applied Pressure Gradient (Wedge)

To create a streamwise pressure gradient without modifying the wall curvature, a wedge was inserted into the wall opposite the flat plate. Sandpaper along the surface of

the upstream portion of the wedge encouraged transition. Suction was applied near the trailing edge of the wedge to ensure proper diffusion of the main flow and facilitate separation on the flat plate test section. For this configuration, the length-to-diameter ratio was 3.75 and 7.5, respectively, for the normal and angled holes. The wedge and its position with respect to the area of data collection are shown in Figure 2-3.

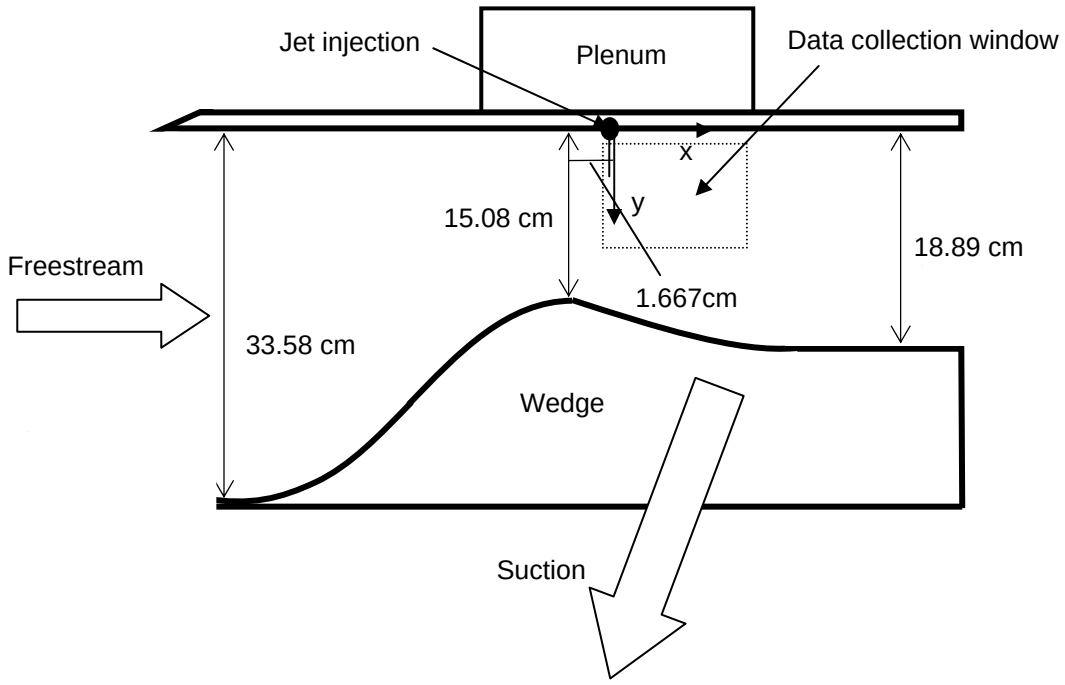


**Figure 2-3**. Wedge test section schematic.

The wedge was carefully constructed and positioned in order to create an adverse pressure gradient similar to that experienced on the suction surface of a LPT blade at low Reynolds number. The blade design chosen to be modeled was the Pratt and Whitney Pack-B blade. This two-dimensional blade shape is a low Mach number scaled version of a highly loaded LPT blade. The Pack-B was selected due to its frequent use among

other researchers (specifically Eldredge and Bons[7]), thus allowing for a better comparison of results. The wedge was designed according to the specifications outlined by Volino and Hultgren[16], who documented its performance using a pressure coefficient based on tunnel exit velocity:

$$c_p = 1 - \left( \frac{U_e}{U_{ex}} \right)^2 \tag{1}$$

The position of the wedge in the wind tunnel and the amount of suction applied to the trailing edge were adjustable, thus allowing the pressure gradient to be matched to the theoretical CFD calculation of the Pack-B blade profile performed by Volino and Hultgren[16]. Velocity data were taken while adjusting the position of the wedge and the amount of suction until acceptable agreement between the data and the design condition was reached. A single element hot-wire was placed at y/d = 15 from the wall and mid-height of the tunnel to collect velocity data at varying x positions in the tunnel. The y/d position was selected as it was close enough to the wall to determine an accurate boundary layer edge velocity, $U_e$, while far enough out from the wall that the measurements were not affected by the developing boundary layer. The velocity data were used to calculate the pressure coefficient according to Eq. 1. The uncertainty in the velocity measurements corresponded to an uncertainty in the pressure coefficient of ±0.25.

Figure 2-4 shows a plot of the pressure coefficient as a function of streamwise distance (x) normalized by the test section (suction surface) length ($L_{ss}$), for the

uncontrolled (B = 0) case compared to the ideal (unseparated) flow calculation. The exit Reynolds number based on $L_{ss}$ and $U_{ex}$ for the wedge configuration is 90,000. For the Pack B blade, $L_{ss}/c_x = 1.67$ and $U_{ex}/U_{in} = 1.25$. This implies an equivalent inlet Reynolds number (based on $c_x$ and $U_{in}$) of 40,000 for the blade profile used by Eldredge and Bons[7].

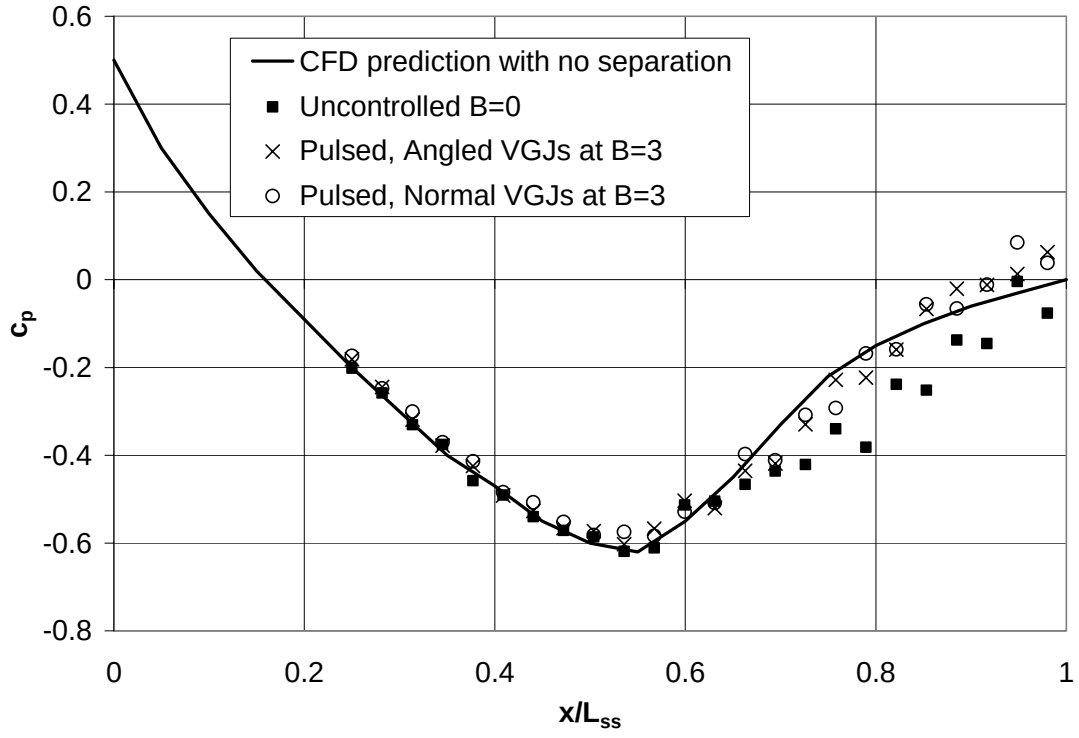


**Figure 2-4**. $c_p$ distribution for wedge configuration showing uncontrolled and controlled pressure distribution compared to the theoretical unseparated prediction.

The plot shows agreement between the theory and data on the upstream side of the wedge for both the uncontrolled and controlled cases. The downstream portion of the wedge, however, shows a deviation between the CFD prediction and uncontrolled case. Here the flow enters the diverging portion of the tunnel, and should be accompanied by a

deceleration as the flow expands. However, the desired flow deceleration is not achieved, as evidenced by the lower $c_p$ for $0.6 < x/L_{ss} < 1$, indicating an area of boundary layer separation. Correction of the flow separation is also evident for both normal and angled pulsed jets, as the $c_p$ values approach the unseparated prediction.

### 2.1.3. Three-Blade Cascade

There has been much previous testing of the effects of VGJs imposed on the Pack-B blade profile. This previous research has explored how VGJs affect the flow separation on an existing LPT blade design. However, the ultimate goal of the VGJ testing is to gain an understanding of how the VGJs control the flow so that future blades can be made with VGJs inherent in the design. This would allow for a more advanced design that relies on the VGJs for proper operation. In an effort to advance the LPT blade design, the traditional Pack-B blade was modified through the joint efforts of BYU and the Wright-Patterson Air Force Base in Dayton, Ohio. The new blade, named L1M, employed VGJs to allow for more aggressive turning while reducing losses. Although using the Pack-B blade in this study would have allowed for a more complete comparison between the results of the wedge and the cascade, it was decided to use the L1M blade for the cascade testing, as it was the most realistic and current design available. Thus, the streamwise pressure gradient and wall curvature of the L1M blade do not correlate directly to the wedge design; however, comparisons can still be drawn in terms of the physical structures that develop in the flow.

The cascade configuration is shown below in Figure 2-5. Three blades were machined from acrylic, with axial chord and span dimensions of 0.22m and 0.38m,

respectively. Fifteen VGJ holes were drilled on the inside blade at 50% $c_x$. The simulations of Sondergaard et al.[17] found that adequate control could be attained by VGJs placed at 45% $c_x$, a position just upstream of the calculated separation point. However, if the calculations had underpredicted the separation position, the VGJs would have proved less effective if they were located too far upstream of the actual separation point. Therefore, the VGJs were moved to 50% $c_x$, since it was unlikely that separation would occur before the point of maximum $c_p$ at 47% $c_x$. The VGJs were placed on the inside blade to ensure that the suction surface would experience uncovered turning as in a full linear cascade. The holes are 2.3mm in diameter and spaced 10 diameters apart, and are oriented at 30º pitch and 90º skew angles as before. A pressurized plenum inside the blade allows for both steady and pulsed injection at a variety of blowing ratios.

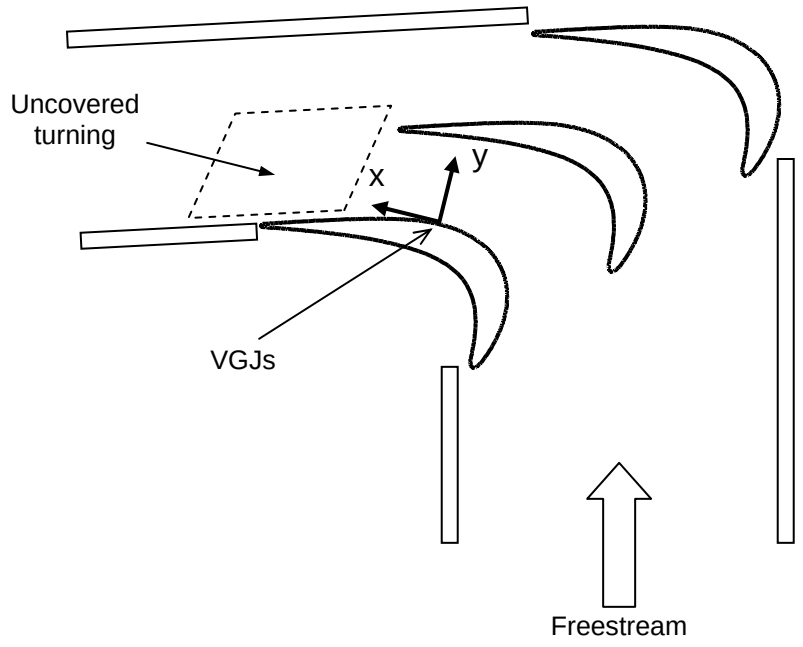


**Figure 2-5**. Three-blade cascade test section schematic.

Static pressure taps (0.64mm diameter) were also added to allow the measurement of $c_p$: fourteen on the suction surface of the controlled blade and seven on the pressure surface of the center blade. Nylon tubing connected the taps to a set of valves and a single Druck pressure transducer. Also, a total pressure probe was inserted upstream as a reference point. The pressure taps allowed the $c_p$ distribution in the tunnel to be verified. Adjustable inlet bleeds and exit tailboards allowed for the $c_p$ distribution to be modified to achieve the desired condition as well as provide periodic flow.

The measured $c_p$ distributions for Reynolds numbers of 50,000 and 20,000 are compared to the computational prediction for both uncontrolled and controlled conditions in Figure 2-6. The predicted $c_p$ distribution was determined using the MISES code developed by Youngren[18] who modified the ISIS airfoil design code of Giles et al.[19] MISES is a two-dimensional coupled Euler/integrated boundary layer analysis code used for separated flows. The uncertainty associated with the pressure data translates to an equivalent $c_p$ uncertainty of ±0.25.

Figure 2-6 shows excellent agreement between the experimental and computational results for the pressure surface and the first half of the suction surface of the blade. The $c_p$ values steadily increase between 0% and 50% $c_x$ along the suction surface as the flow accelerates. Separation is evident as $c_p$ values level off (at about 65% $c_x$ for Re = 50,000 and 60% $c_x$ for Re = 20,000) and the flow deceleration is inhibited. The disappearance of the separation bubble, as seen by an abrupt drop in $c_p$, occurs at 79% and 86% $c_x$ for the 50,000 and 20,000 Reynolds number cases, respectively.

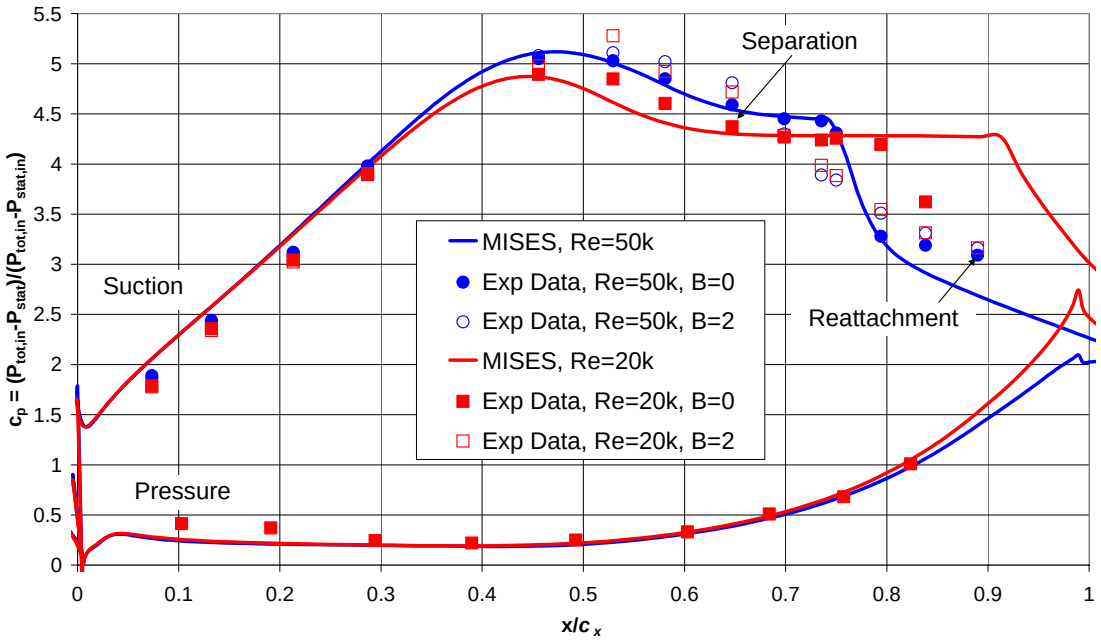


**Figure 2-6.** cp distribution for the L1M blade. Lines indicate the results of theoretical predictions, while points represent data points extracted from the experimental setup.

## 2.2. Instrumentation

### 2.2.1. PIV (Particle Imaging Velocimetry)

The data for this research were collected using a particle imaging velocimetry system, which measures all three velocity components in a planar laser sheet in the flow. PIV systems operate in the following manner. First, many tiny, light-reflecting particles (called seed particles) are introduced into the wind tunnel. These particles flow through the tunnel to the area of interest, where a laser illuminates the flow field twice in rapid succession. The light from the laser is reflected off the seed, creating two images that are captured by two digital cameras. These images are then sent to a computer, where the displacement of the particles between both images is determined through a cross

correlation function. The computer then uses this displacement and the known time lapse between the laser pulses to calculate the velocity vectors.

There are several parameters that need to be carefully monitored in order to produce accurate results with a PIV system. For example, the thickness of the laser sheet must be large enough so a significant number of particles remain in the laser sheet between the laser pulses; however, a laser sheet that is too thick introduces error into the velocity calculations because of the difficulty of projecting three-dimensional motion on to a two-dimensional plane. A laser sheet that is too thick also reduces the spatial resolution of the image in strong gradients. The size of the seed particles is important, as particles that are too large will reduce the accuracy of the displacement measurement and may not necessarily follow the flow. The time interval between laser pulses must also be carefully determined. It must be short enough so that the displacements of the seed particles remain small and that the majority stay in the sheet for the second laser pulse, yet large enough to be measured accurately.

In this research, three-dimensional flow measurements were made using a LaVision 3 component stereo PIV system. This system was mounted on a 3-axis traverse located below the transparent acrylic test section to enable a full mapping of the flow field. An Nd:YAG laser illuminated the flow field with a light sheet approximately 1mm in thickness. The flow was seeded with oil particles that were 1-2μm in diameter. Images were recorded by two digital cameras with a resolution of 1376 by 1040 pixels. Photographs of the setup are shown in Figure 2-7 (for the flat plate and wedge configurations) and Figure 2-8 (for the cascade configuration). For the steady VGJs, the

cameras and lasers were synchronized internally; however, the pulsed VGJs required that the cameras and lasers be externally synchronized to the pulsed VGJ flow.

For the flat plate and wedge configurations, the available data collection window measured about 70mm (y, wall normal) by 90mm (x, streamwise). The cameras were aligned so that the data collection window was positioned to include the region including $-1<x/d<21$ and $1<y/d<16$ (see Figure 2-3). In order to determine the distance between the wall and the nearest velocity vector, a ruler was placed flush to the wall and imaged by the cameras. This allowed the distance between the actual wall surface and the edge of the camera image to be measured. When the velocity vectors were calculated, the gap between the edge of the image and the position of the velocity vectors was also determined. These two distances (from the wall to the edge of the image, and from the edge of the image to the closest velocity vector) were summed to find the total gap between the wall and the velocity data points.

A schematic of the three-blade cascade is shown in Figure 2-9. The data collection window was slightly larger than before, reaching about 80mm in the y direction and 105 mm in the x-direction. Because of the curvature of the blade surface, the x- and y-directions could no longer be easily defined by wall position. The x-direction is still in the general streamwise direction; however, the y-direction is no longer wall-normal. These coordinate directions are shown in Figure 2-5. Two separate overlapping data collection window positions were used to completely encompass the area of separation created by the blade.

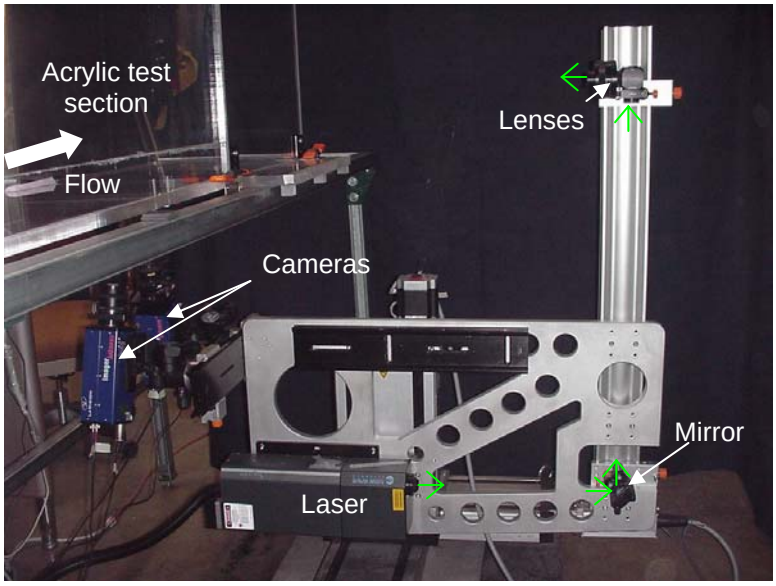


**Figure 2-7**. Photograph of PIV system. The laser path is indicated by green arrows.

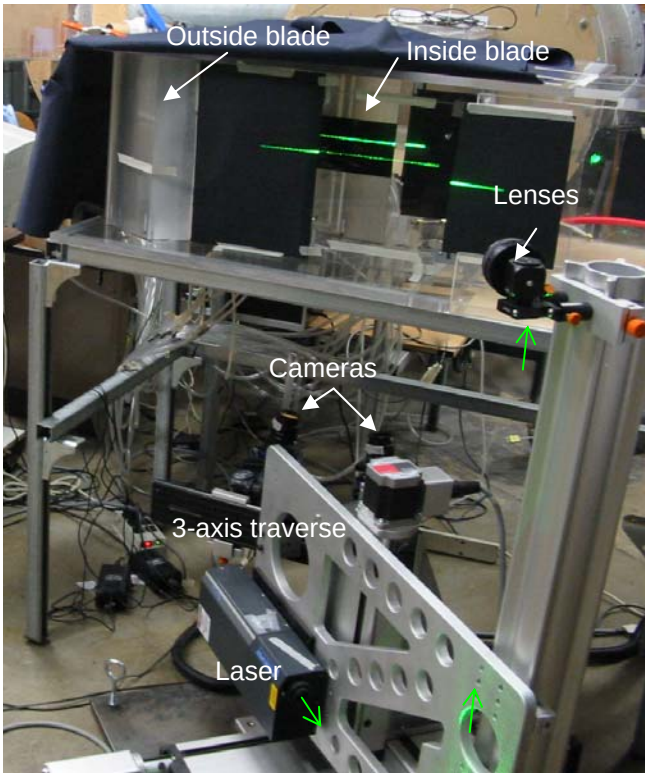


**Figure 2-8**. Photograph of three-blade cascade configuration. The laser path is indicated by green arrows.

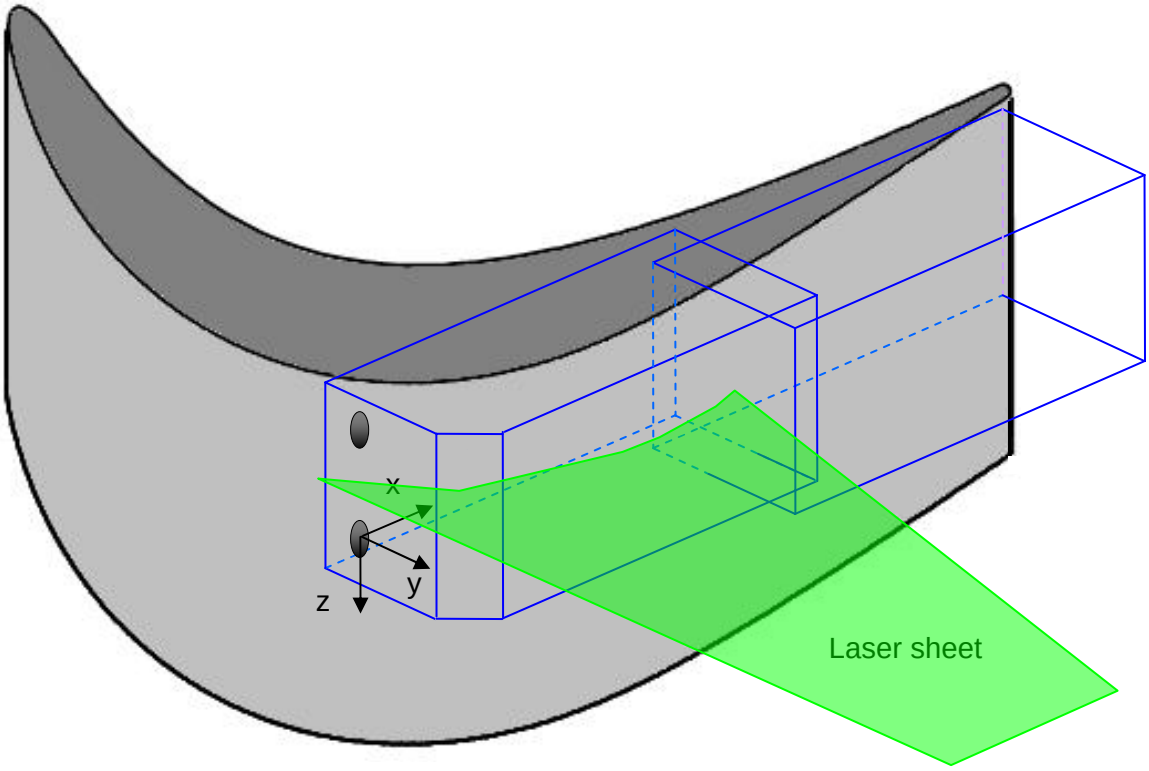


**Figure 2-9**. Schematic of PIV data collection areas relative to the L1M blade.

To collect the data, the laser sheet was oriented in the x-y plane. Forty separate images at each z location were recorded, processed and averaged. A study was done by collecting and averaging successively larger numbers of images (from 10 images up to 50 images) and then calculating the average u, v, and w components of velocities. The change in the velocity values from this value is shown below in Figure 2-10.

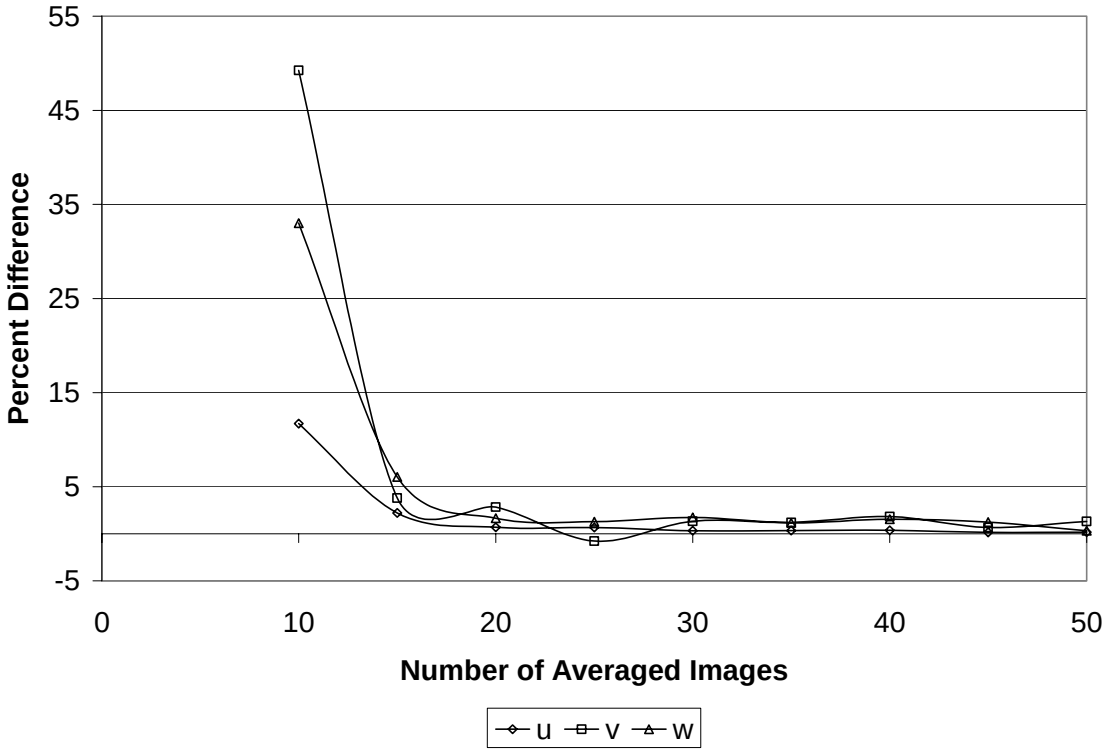


**Figure 2-10**. Percent difference of averaged u, v and w velocity components between successively larger numbers of images.

Figure 2-10 clearly shows that the values of the velocity vectors change significantly between an average of 10 and 15 images. However, the difference reduces to about 1% after passing the 40 image mark. For this reason 40 images were collected and averaged for this research.

The steady jet measurements were taken at an internal framing rate of 9.9 Hz, while the pulsed jet measurements were phase-locked with the jet forcing. Vector processing was first completed using 64 by 64 pixels with subsequent processing refinements resulting in vectors for every 32 by 32 pixels in the camera frame. The use of two cameras (stereo PIV) allowed the measurement of u, v and w components of velocity. This procedure was repeated at increments of 2mm in z for the flat plate and

wedge configurations and 1mm in z for the cascade configuration in order to generate a three-dimensional block of velocity data. LaVision states the uncertainty of the seed particle displacement determination to be on the order of 0.1 pixels, depending on how easily a peak can be found in the cross correlation function. This uncertainty in displacement corresponds to a velocity uncertainty of less than 0.1 m/s (about ±3% of the freestream velocity) for the flat plate and wedge configurations, and 0.25m/s (about ±7% of the local velocity) for the cascade configuration.

### 2.2.2. Blowing Ratio

One of the important parameters in this study is the blowing ratio, B, which is defined as the ratio of the jet velocity to the local velocity of the air passing the jet holes. A blowing ratio of 2 was selected for the experiments conducted in this research. This blowing ratio was selected for several reasons. First, Bons et al.[10] recommended blowing ratios between 2 and 4 for effective separation control, which was corroborated by the research of Eldredge and Bons[7]. The lower limit of these recommendations was chosen in order to reduce the necessary mass flow of compressed air. Also, a jet velocity twice that of the local fluid was found to be strong enough to create coherent vortical structures that remained close enough to the boundary layer to affect the separation.

A single element hot-wire was used to determine the blowing ratio. For the flat plate and wedge configurations, a high pressure air line was connected to the plenum (see Figure 2-3), with a valve allowing the inlet air pressure to be regulated. The hot-wire was oriented at the jet hole exit such that it measured the point of maximum jet velocity: at the center of the normal hole and at the top of the angled hole (Figure 2-11). The exiting

jet velocity was measured for several varying pressures, so that the proper pressure could be selected during testing that would yield the desired blowing ratio, depending on the inlet velocity in the wind tunnel. The hot-wire measurements were taken without freestream flow in the tunnel, thus creating a slight difference in total pressure between the conditions of the blowing ratio measurements and those of actual operation. This change in pressure was corrected during testing to ensure that the blowing ratio was accurate.

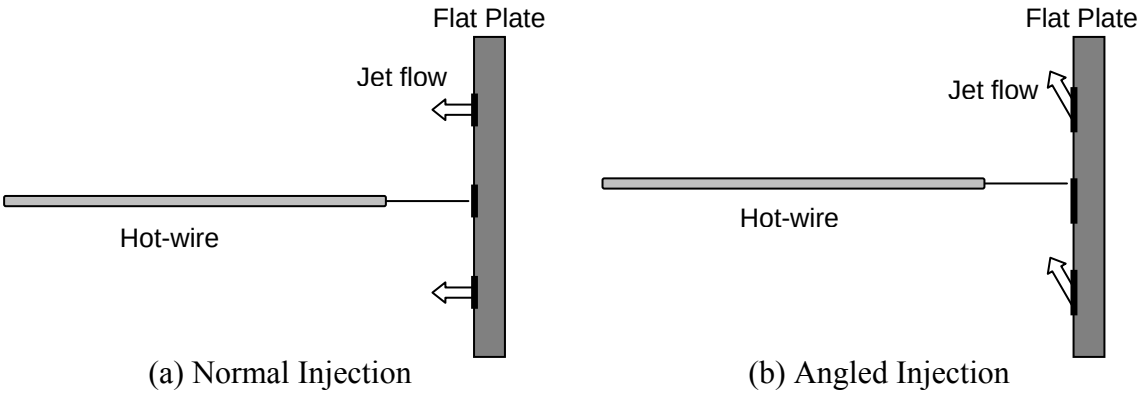


**Figure 2-11**. Hot-wire orientation relative to normal and angled jet holes for blowing ratio measurement for the flat plate and wedge testing configurations.

### 2.2.3. Pulsing Cycle

For the pulsed testing, the high pressure air line was connected to a Parker-Hannefin pulsed valve to create a pulsed jet of air. The valve was operated at a frequency of 5Hz with a 25% duty cycle (ratio of jet on time to total time). This valve fed the air into the plenum to produce modulated air through the jet holes.

A hot-wire was again used to measure the velocity of the air pulse, which is essentially a step-function. Some attenuation occurred in the plenum resulting in a slightly modified jet waveform, as shown in Figure 2-12. This figure shows the jet hole exit blowing ratio time history measured by the hot-wire for the wedge configuration. The peak value of B is approximately 2.5 and the mean value is 0.75 for this case. PIV data were collected at eight points (called phases) within the pulsing period. The timing of these points is shown by arrows in Figure 2-12, and was selected in order to obtain data during the beginning, middle, and end of the pulse, as well as during the time that the pulse was off.

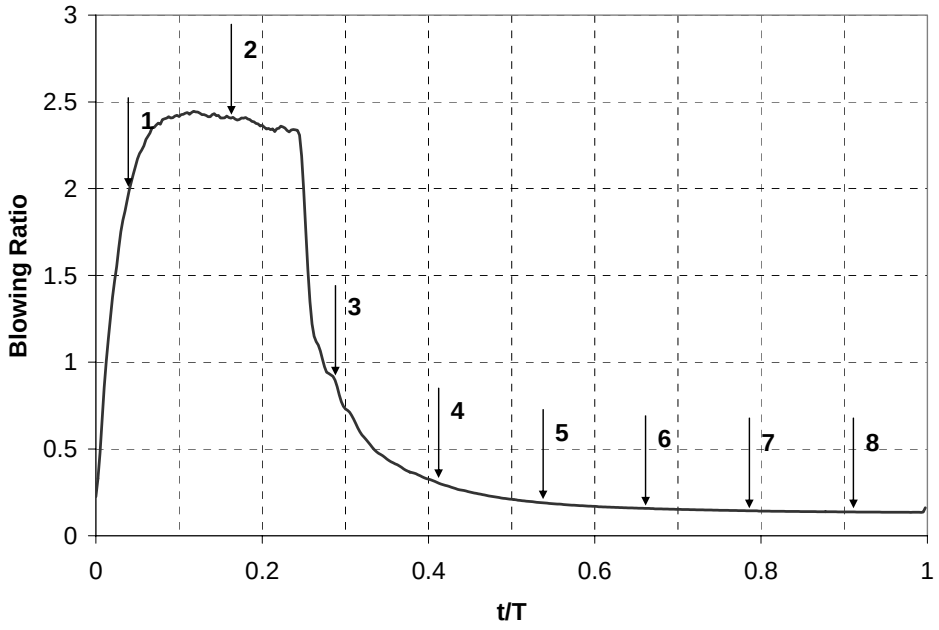


**Figure 2-12**. Jet hole exit blowing ratio time history for VGJ operation at 5Hz and 25% duty cycle for the flat plate and wedge configurations. Arrows indicate PIV data collection points.

For the cascade configuration, the pulsing cycle in Figure 2-13 was modified slightly. Although the general shape and timing of the cycle remained the same as for the flat plate and wedge, the magnitude was reduced. The peak value of B was approximately 2, with a mean value of 0.7.

A time lag of about 2.5ms was experienced between the initiation of the jet pulse and the peak VGJ flow. To account for this time lag, the start of the pulse (t/T = 0) was redefined at the beginning of the step function, and the eight phases were then selected in reference to that point.

## 2.3. Data Postprocessing

The capability of the PIV system to produce very large amounts of data within a relatively short amount of time required that the data be refined and organized before the analysis could be done. Data were collected in several x-y planes at varying elevations, creating a raw data set consisting of a three-dimensional block containing thousands of points of velocity data (Figure 2-13a). In order to observe the changes in the flow field, a postprocessing program was written in Matlab that allowed the block of data to be "sliced" in any of the 3 coordinate directions at any position in the data domain. Three components of vorticity were also calculated using centered differences. Graphical capabilities were included so that all components of velocity and vorticity could be plotted in any plane (Figure 2-13b). This Matlab program (included in the Appendix) became a very powerful tool for the analysis and interpretation of the data.

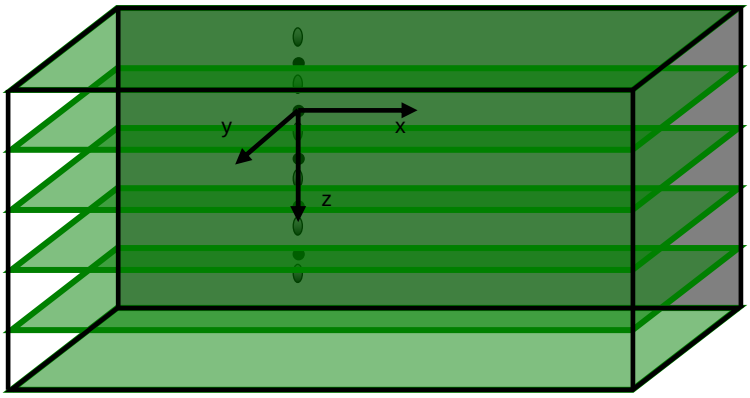


(a) Data collection planes

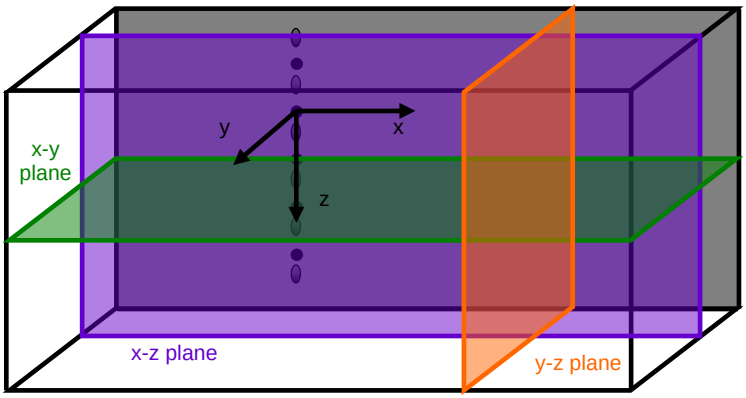


(b) Plotting planes

**Figure 2-13**. Schematic of postprocessing planes

It was also found that three-dimensional surface plots were extremely effective in tracking the movement of the flow. While the two-dimensional contour plots showed more detail at specific positions in the flow field, the surface plots provided a larger overview of the flow for the entire length of the flow field. The surface plots were generated by traversing the three-dimensional space of velocity data in the negative y-direction from the freestream to the wall or blade. The surface was then identified as the first occurrence of a specified velocity value (Figure 2-14).

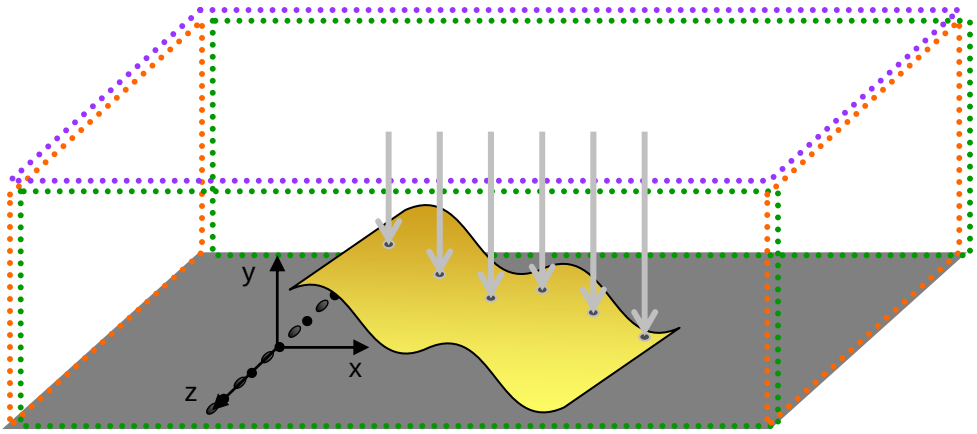


**Figure 2-14**. Schematic of 3-D surface plot generation

Further postprocessing was necessary for the cascade configuration. Because of its increased length, two separate data domains (one upstream and one downstream) were necessary in order to capture the flow from the jet injection point to the trailing edge of the blade. The Matlab program was modified so that the upstream and downstream domains could be merged to produce one continuous flow field. Also, the y-coordinate of the blade contour was subtracted from the three-dimensional velocity surface to assist in the visualization of the flow separation. The resulting velocity surface elevations are relative to the surface of the blade.

# 3. FLAT PLATE (ZERO PRESSURE GRADIENT)

## 3.1. Steady Jet Injection

### 3.1.1. Normal Injection

Contour maps of streamwise and wall-normal velocity, as well as streamwise vorticity, plotted in z-y planes at five different downstream positions, are shown in Figure 3-1. Velocities are normalized by $U_{inf}$ and data were taken over two hole pitches. The reader is referred to Figure 2-2 for the orientation of the Cartesian axes. x/d = 0 is at the centerline of the hole row, y/d = 0 is at the wall, and z/d = 0 is at the center of the hole.

Several important characteristics of the flow are evident from Figure 3-1. First, the lobes of low u-velocity fluid (left column) denote the position of the jet fluid that is injected with no streamwise momentum. This low velocity lobe gradually moves out from the wall as it travels downstream, ultimately reaching a maximum y/d position of 4.5 (wall distance to the center of the lobe) at x/d = 20. The jet trajectory is evident in the x-y plane of streamwise vorticity shown in Figure 3-2. Since there is zero skew to the injection, the jet remains at the same z position throughout its trajectory (Figure 3-3).

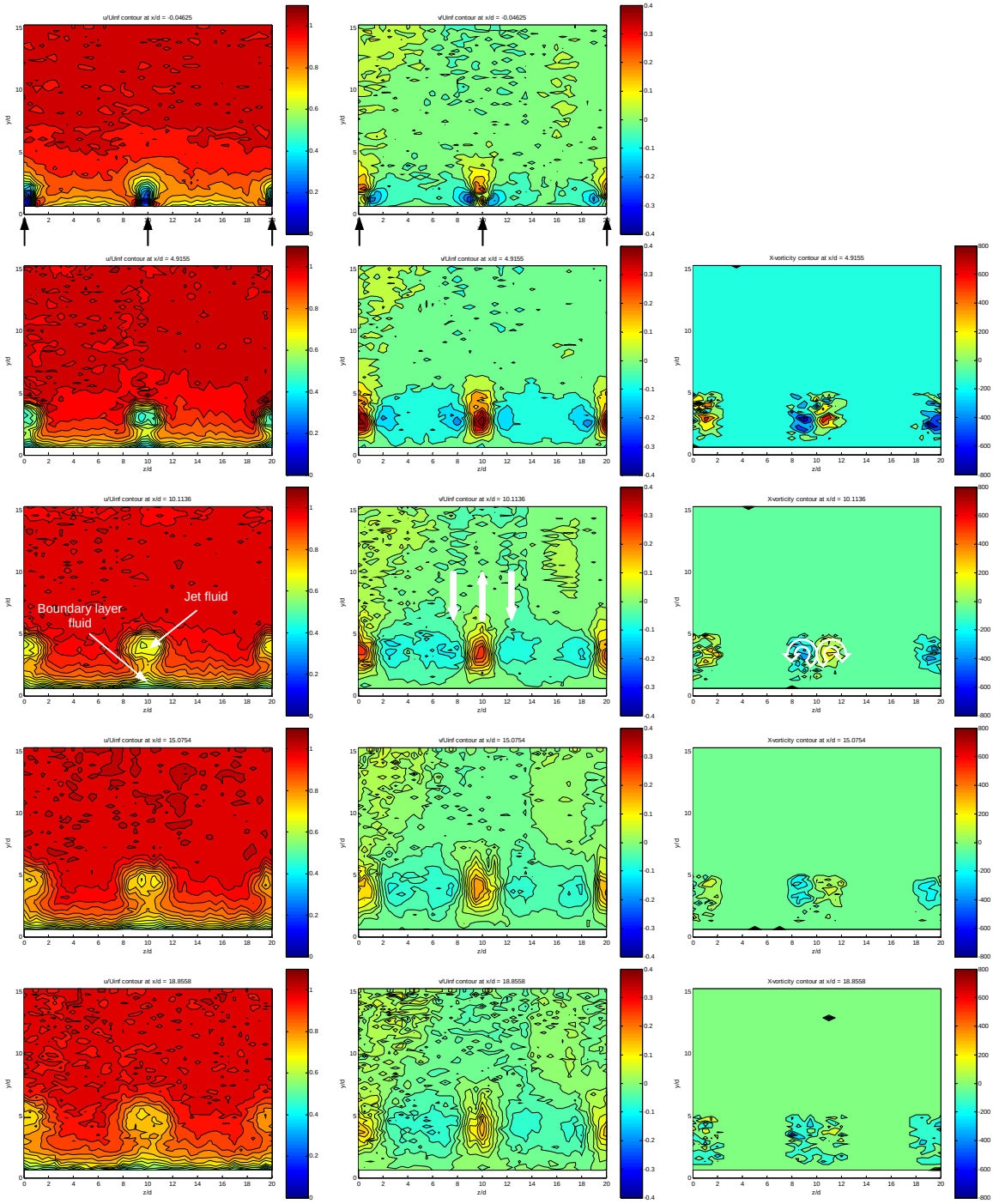


**Figure 3-1**. Contour maps of streamwise velocity (left column), wall normal velocity (center column) and out-of-plane vorticity (right column) showing vortex development at streamwise positions of x/d ≈ 0, 5, 10, 15 and 20. Steady, normal jet injection into zero pressure gradient with B = 2. Looking in the positive x direction. Black arrows indicate jet injection points.

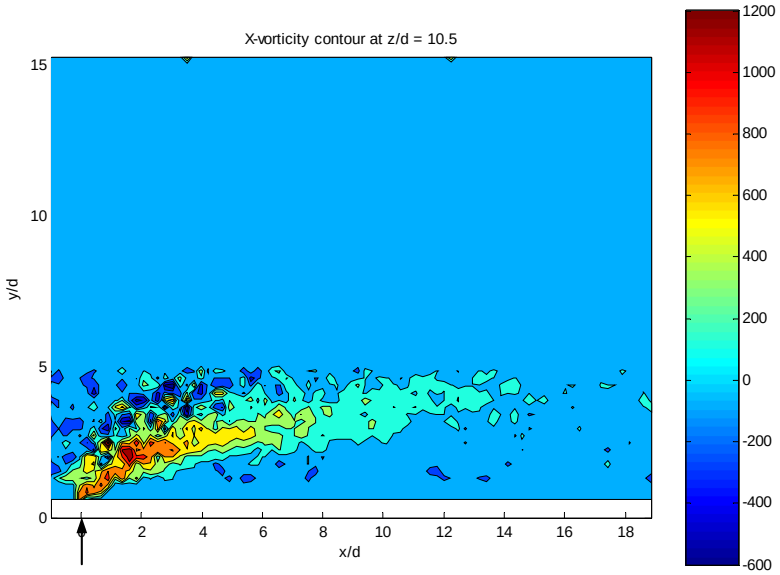


**Figure 3-2**. Streamwise vorticity contour shown in the x-y plane at z/d ≈ 10. Steady, normal jet injection into zero pressure gradient with B = 2. Looking in the negative z direction. The black arrow indicates the jet injection position.

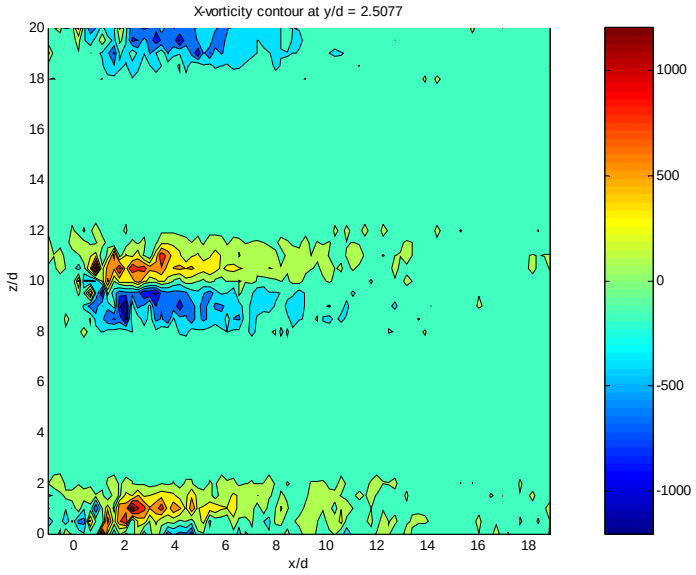


**Figure 3-3**. Streamwise vorticity contour shown in the x-z plane at y/d = 2.5. Steady, normal jet injection into zero pressure gradient with B = 2. Looking in the positive y direction.

Likewise observed from Figure 3-1 is the development of streamwise vortices. The $v/U_{inf}$ contour plots (center column) show that these vortices develop as fluid is forced outward normal from the wall at the injection point and then cycled back on both sides. This effect is promulgated downstream as the double vortex grows in size while decreasing in magnitude. After traveling 15 diameters downstream, the magnitude of the vorticity is reduced by 75% (see x-z plot of streamwise vorticity in Figure 3-3). This double vortex induces the expected mushroom shaped $u/U_{inf}$ contour visible in Figure 3-1, as documented by Khan and Johnston[6].

### 3.1.2. Angled Injection

Similar results were obtained for the angled jets. Figure 3-4 again shows streamwise and wall-normal velocity and out of plane (streamwise) vorticity contours in the z-y plane at the same downstream location of x/d = 10. Figures 3-5 and 3-6 show the corresponding x-y and x-z planes of streamwise vorticity. The velocity is again normalized by the freestream value.

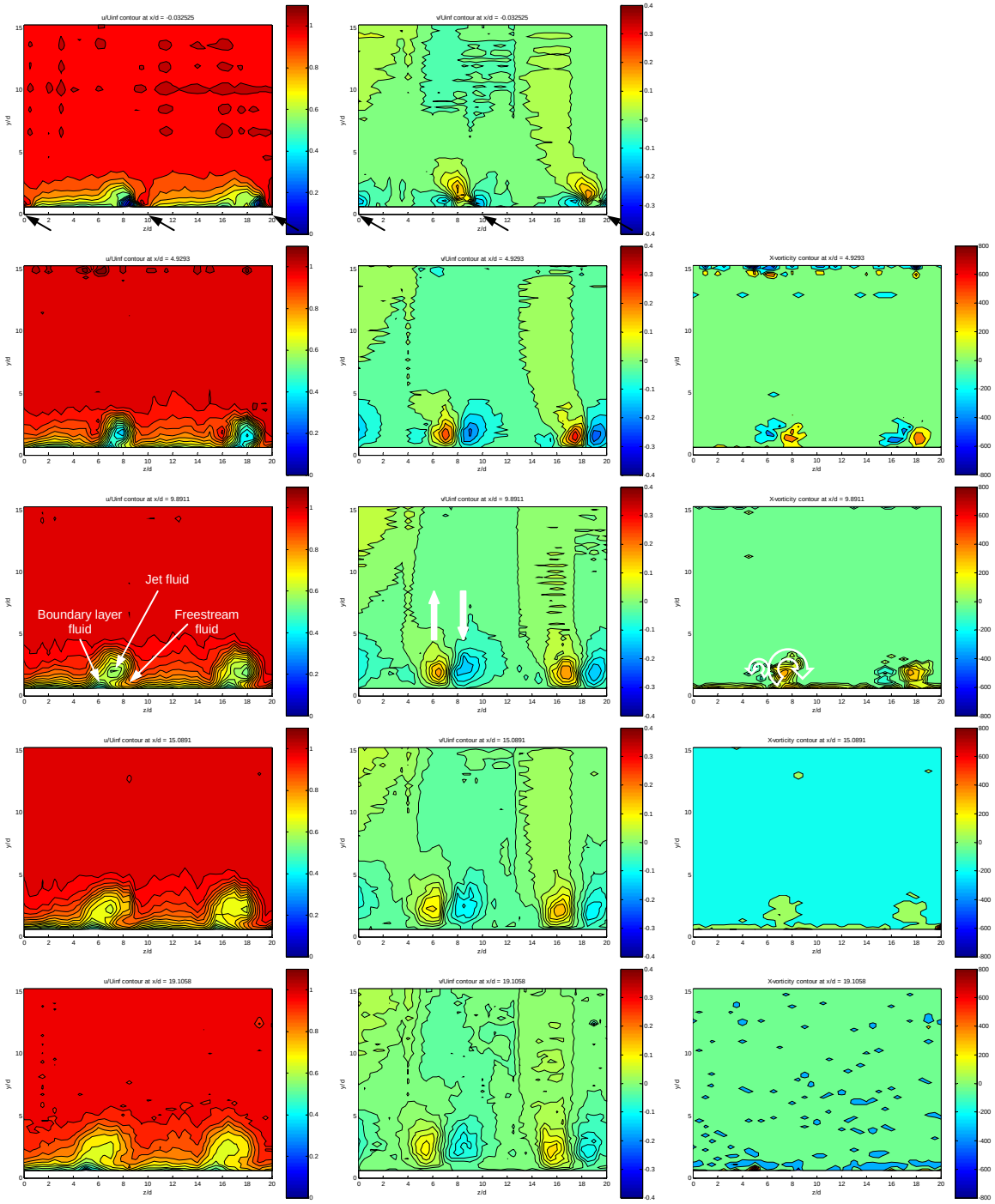


**Figure 3-4**. Contour maps of streamwise velocity (left column), wall normal velocity (center column) and out-of-plane vorticity (right column) showing vortex development at streamwise positions of x/d ≈ 0, 5, 10, 15 and 20. Steady, angled jet injection into zero pressure gradient with B = 2. Looking in the positive x direction. Black arrows indicate jet injection points.

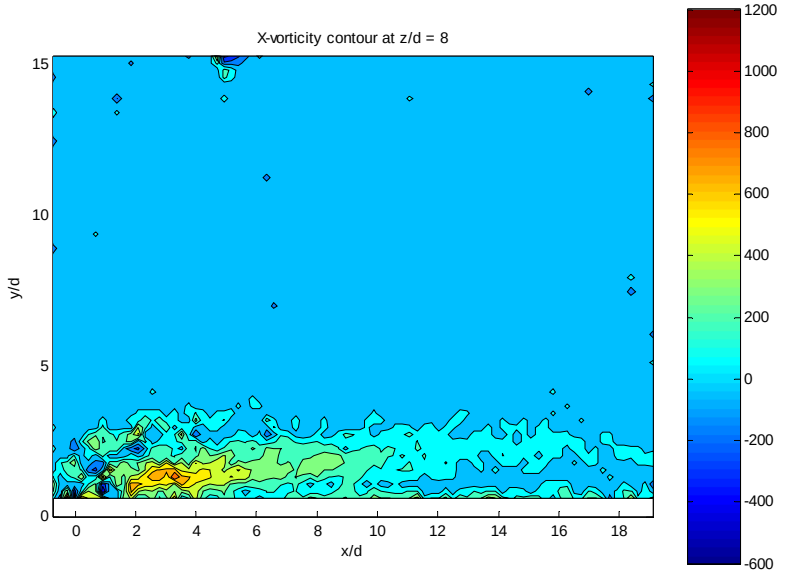


**Figure 3-5**. Streamwise vorticity contour shown in the x-y plane at z/d = 8. Steady, angled jet injection into zero pressure gradient with B = 2. Looking in the negative z direction.

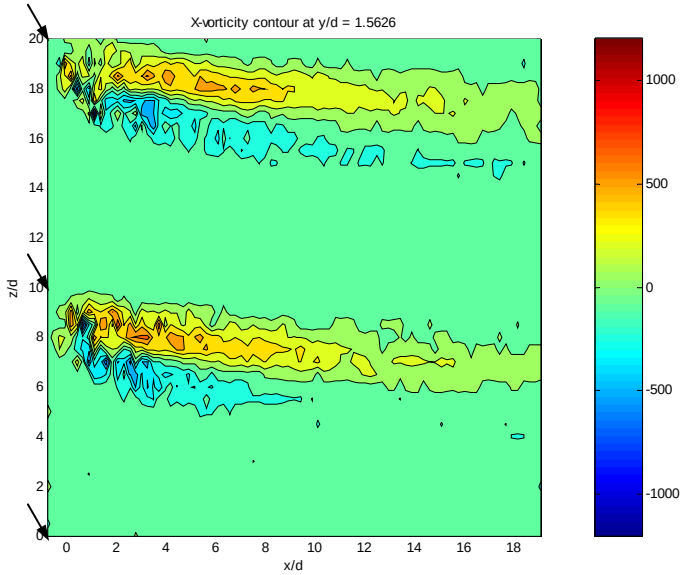


**Figure 3-6.** Streamwise vorticity contour shown in the x-z plane at y/d = 1.5. Steady, angled jet injection into zero pressure gradient with B = 2. Looking in the positive y direction.

As before, lobes of low u-velocity fluid indicate the presence of jet fluid, but it is clear that the trajectory of the angled jet is different from that of the normal jet. Because of the angle of injection, the jet fluid penetrates only half as far out from the wall as the normal jet, the center of the jet fluid reaching a maximum y/d of only 2.25 at x/d = 20 (Figures 3-5 and 3-6) . There is, however, considerable migration in the spanwise direction, as the jet fluid travels to a position over 3 diameters in z from the injection point (Figure 3-6).

The development of streamwise vortices is also apparent from Figure 3-4. The angled jet creates a double vortex, with the dominant positive vortex becoming much stronger and larger than the negative vortex (right column). It is clear that the vortex caused by the angled jets migrates significantly in the spanwise direction, as fluid is forced out from the wall at 2.5 z/d from the injection point and then circulates back towards the wall. As in the case of normal injection, the vortex grows in size as it travels downstream. However, the primary vortex caused by the angled jets is a coherent structure for a longer distance. At a distance of 15 diameters downstream, the magnitude of the vorticity is reduced by only 45% (Figure 3-6).

Both the trajectory of the primary vortex and the logarithmic streamwise decay of peak vorticity found in this research are comparable to the results of Rixon and Johari[8]. Figure 3-7 plots the wall normal vortex migration and peak streamwise vorticity (vorticity normalized by $\delta/U_{inf}$) as a function of streamwise distance from the jet injection point normalized by $\delta$. Although Rixon and Johari studied jets injected into a turbulent boundary layer at a 45° pitch and 90° skew angle, similar trends can be seen.

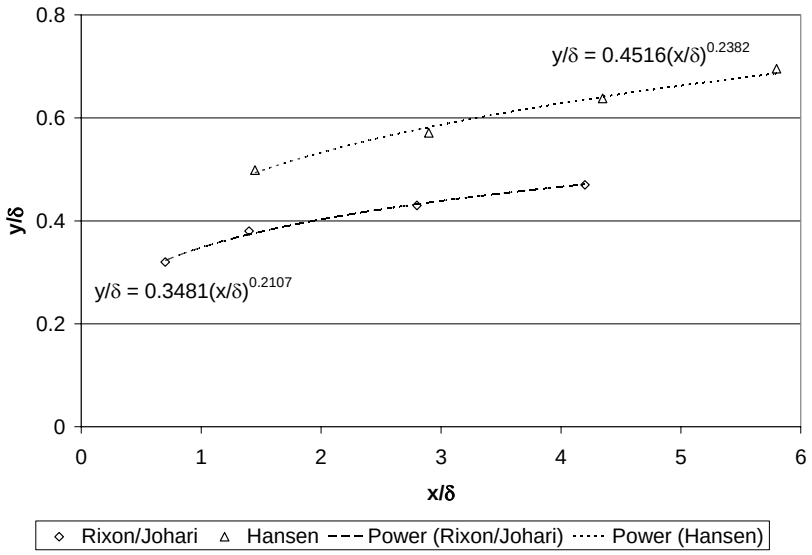


(a) Vortex migration

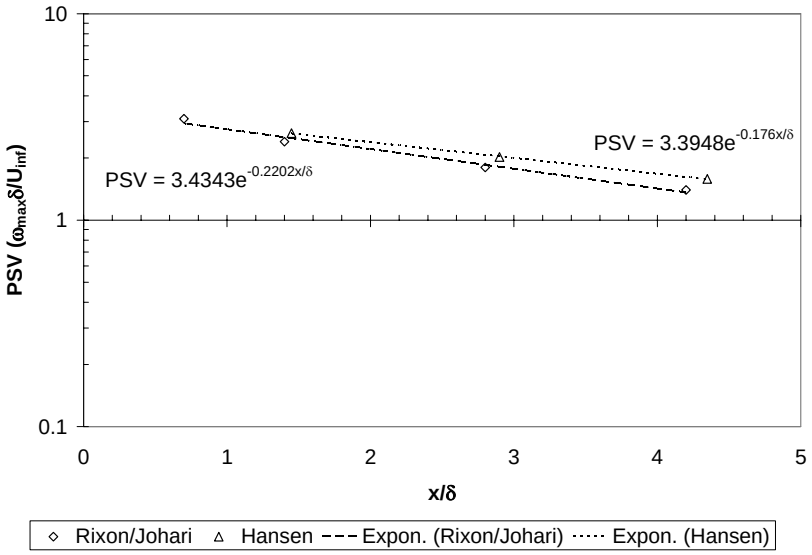


(b) Peak streamwise vorticity

**Figure 3-7**. Comparison of vortex migration and peak streamwise vorticity between current study and the results of Rixon and Johari.

Another phenomenon of interest is displayed more clearly in a three-dimensional plot of the flow field. Figure 3-8 shows the surface where the u-velocity component is 60% of the freestream velocity ($u/U_{inf} = 0.6$). The jet injection location is indicated by arrows along the z axis, and the ensuing vortical effect is evident as the flow travels downstream. The plot is colored by surface height in the y-direction.

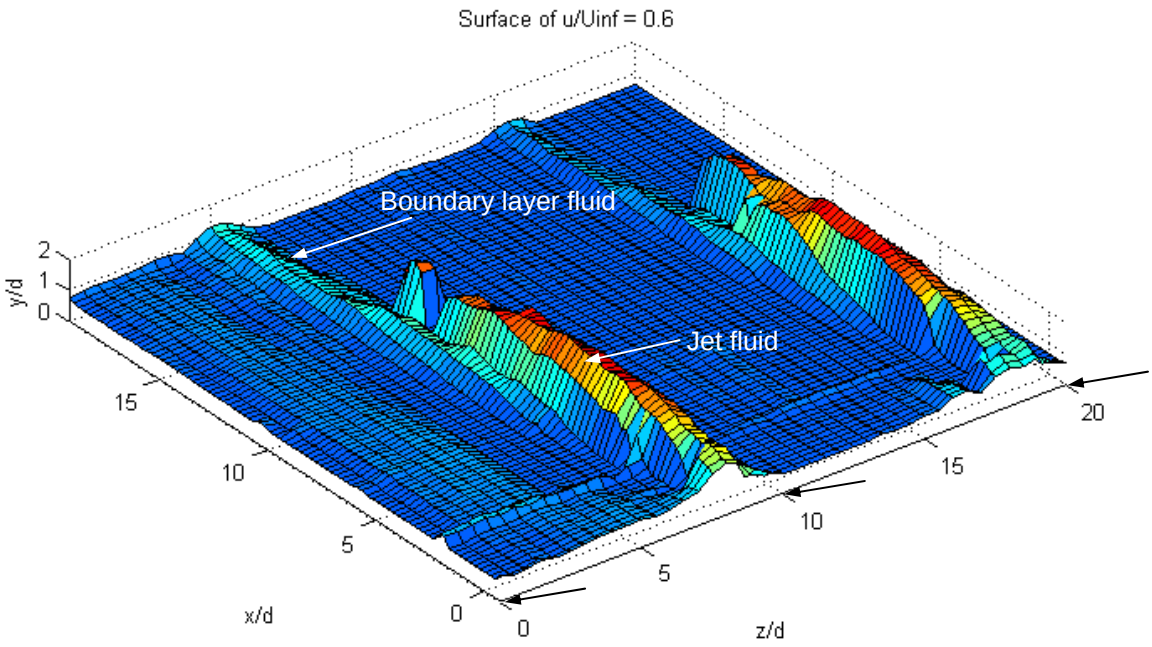


**Figure 3-8**. 3-D surface of streamwise velocity where u = 0.6Uinf. Steady, angled jet injection into zero pressure gradient with B = 2. The surface is colored by height in the y direction. Black arrows indicate jet injection points.

The dominant characteristic in Figure 3-8 is the double hump-like feature that develops downstream of each jet injection point. The larger of the humps is the low-velocity jet fluid. After the fluid exits the hole, obstructing the freestream flow, it is gradually entrained by the main flow. By x/d = 14, the lobe of jet fluid has been

accelerated to above 60% $U_{inf}$, and its presence in the surface contour in Figure 3-8 disappears.

A second low-velocity hump located closer to the wall extends farther in the x-direction. This is indicative of boundary layer fluid being drawn out from the wall. The streamwise vortices caused by the angled jets occur sufficiently close to the wall that they pull low momentum fluid up from the boundary layer. This behavior is also evident in Figure 3-4, where a small pocket of low velocity fluid can be seen rising up from the wall at the position where the vortex has its highest outward movement ($z/d \approx 6.5$). Likewise, the return motion of the cycling vortex brings high momentum freestream fluid back down close to the wall on the other side (at $z/d \approx 8.5$). This behavior is consistent with the findings of Khan and Johnston[6], who also discovered a thinning and thickening of the boundary layer on opposite sides of the vortex. The high momentum fluid brings with it turbulent fluctuations generated by the jet shear layers, creating ingredients for flow transition in the wake of the jet (as discussed by Volino[14]).

### 3.2. Pulsed Jet Injection

Pulsed jet injection produced results comparable to steady jet injection. The jet fluid followed a similar trajectory and produced similar vortical structures. The disturbance is not as extensive, however, as air is only injected into the flow for 25% of the time. Evidence of this is shown in Figure 3-9, in which surface plots of streamwise velocity are displayed for six different points corresponding to phases 1-4, 6 and 8 of the pulsing cycle (see Figure 2-12). The left column shows the surface of $u = 0.8U_{inf}$ where

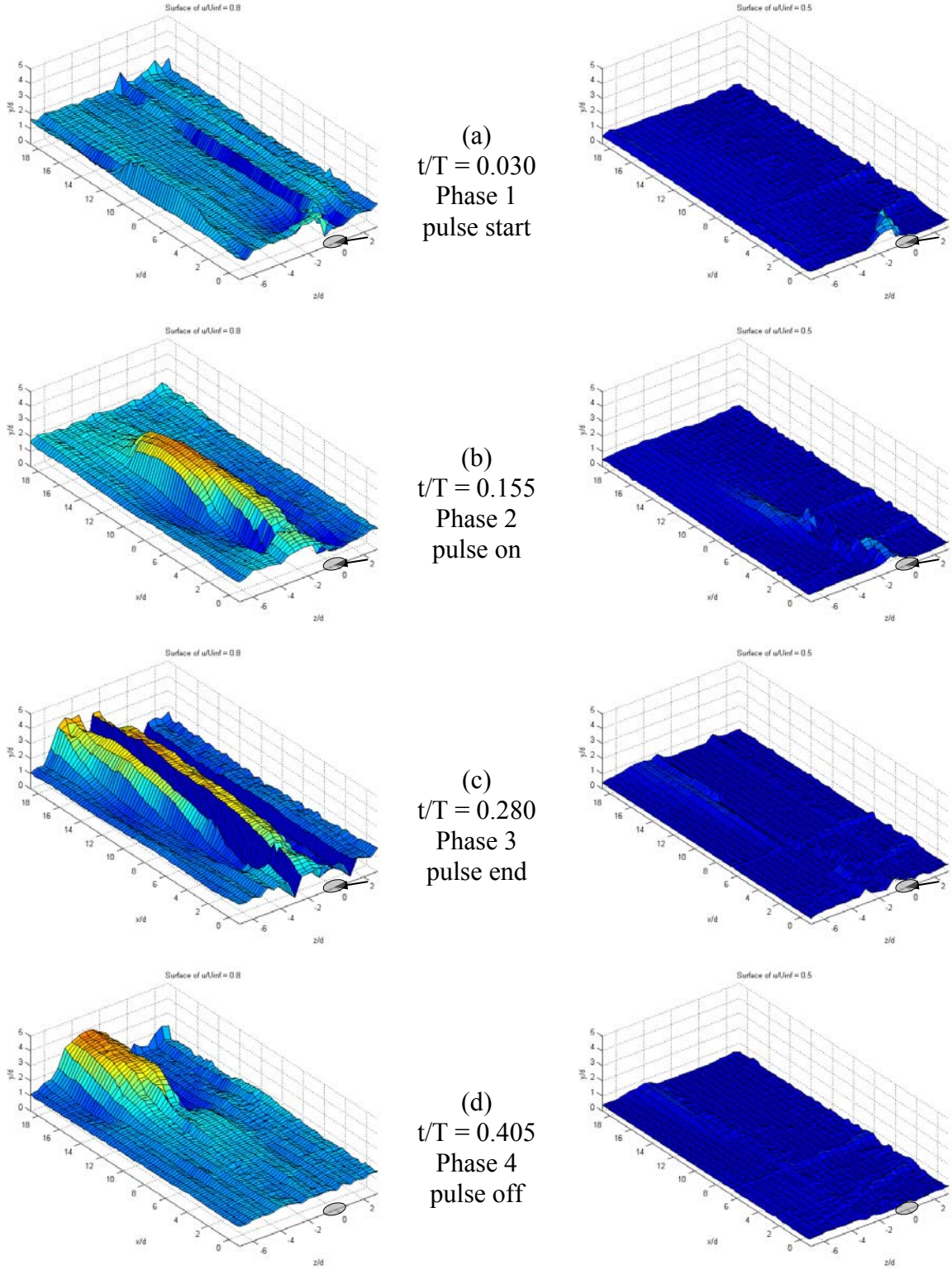


(a)
t/T = 0.030
Phase 1
pulse start

(b)
t/T = 0.155
Phase 2
pulse on

(c)
t/T = 0.280
Phase 3
pulse end

(d)
t/T = 0.405
Phase 4
pulse off

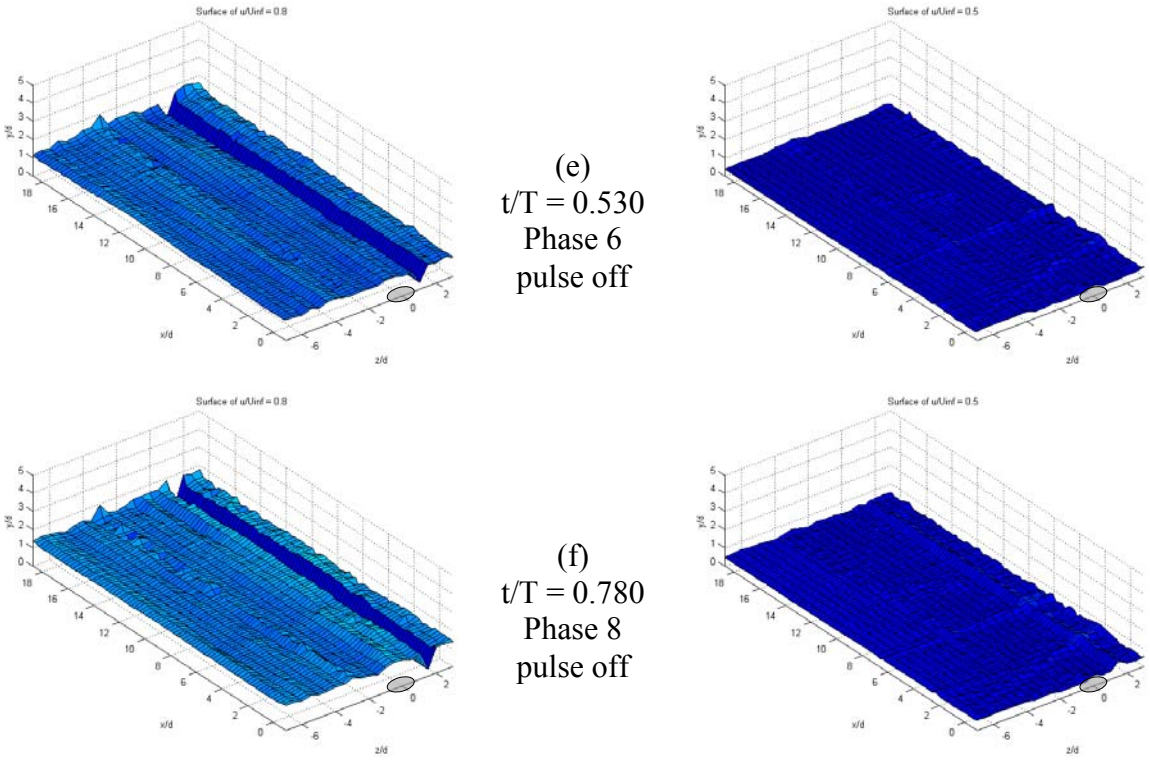


**Figure 3-9**. 3-D surfaces of streamwise velocity where $u = 0.8U_{inf}$ showing jet movement (left column) and $u = 0.5U_{inf}$ showing boundary layer behavior (right column) taken at 6 discrete points in the pulsing cycle. Pulsed, angled injection into zero streamwise pressure gradient at 5 Hz and 25% duty cycle with maximum B = 2.5. VGJ holes are shown as gray ovals, with black arrows indicating the presence and position of the jet pulse.

the jet fluid can be seen, while the surface of $u = 0.5U_{inf}$ shown in the right column shows the boundary layer behavior during the cycle.

The position of the jet fluid through the pulsing cycle is evident from the plots in the left column of Figure 3-9. When the jet is first turned on (Figure 3-9a), a disturbance is seen to start, indicating the entrance of the VGJ fluid. The jet fluid can then be followed in its path downstream as it continues to be injected into the flow during the next two phases (Figures 3-9b and c). Although the jet has been turned off by phase 4 (Figure 3-9d), there is still some remaining jet fluid that has not yet left the field of view.

The last two phases (Figures 3-9e and f) clearly show the absence of jet fluid while the jet is turned off.

The presence of streamwise vortices can be deduced from the right column of Figure 3-9, as the sweeping up of the boundary layer can be seen as previously noted for the steady, angled jets. This secondary hump appears first during phase 2 (Figure 3-9b), and travels downstream with the vortices caused by the jet disturbance (Figures 3-9c and d). After the jet fluid, and likewise the streamwise vortices, has left the flow field, the boundary layer returns to its original state.

These results, both for the steady and pulsed jets, lend validity to the freestream entrainment theory for the application of angled jets with no freestream pressure gradient. The structure and migration of the streamwise vortices indicate that high momentum freestream fluid is brought down close to the wall, effectively energizing the low momentum boundary layer. However, these observations are for a non-separating boundary layer. This leads to the following questions: (1) How does the previously discussed development of streamwise vortices affect boundary layer separation? and (2) Is the jet development altered by the decelerating flow? Further results described in the following sections describes the efforts made to answer these questions.

# 4. FLAT PLATE WITH APPLIED STREAMWISE PRESSURE GRADIENT (WEDGE)

## 4.1. Boundary Layer Modification

Before exploring the effect of the jets on flow in the wedge configuration, the difference between the separating and non-separating boundary layer was verified. To do this, PIV images were taken at 21 z-locations over one hole pitch for the low Reynolds number case in the wedge configuration. This was compared to similar data taken previously in the flat plate (no pressure gradient) configuration. The laminar boundary layer development for these uncontrolled (B = 0) cases is shown below in Figure 4-1.

These contour plots are produced by averaging the x-y planes at all 21 z/d locations into a single plot. The effect of the presence of the inserted wedge is apparent in Figure 4-1b. For the wedge case, the streamwise deceleration of the freestream flow produces a rapid increase in the boundary layer thickness and a near wall region of low momentum (separated) fluid (note the dashed white line at $u/U_{inf} = 0.2$). By comparison, the boundary layer for the original flat plate flow shows little perceptible streamwise development (Figure 4-1a). The difference in the x/d = 0 boundary layer thickness between the two plots is due to the rapid acceleration upstream of the jet location in the wedge configuration.

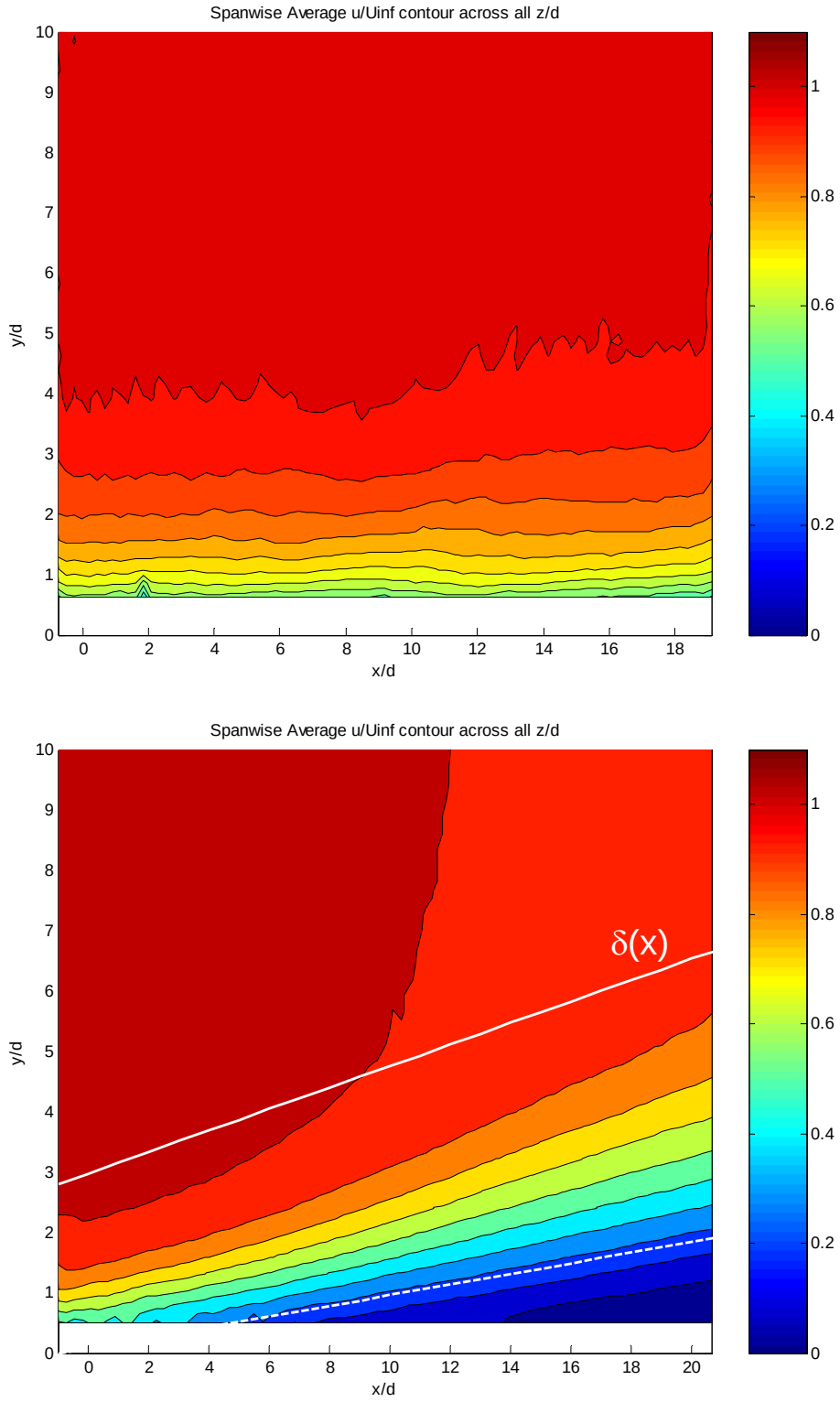


**Figure 4-1**. Spanwise averaged plots of the streamwise component of velocity for the uncontrolled (B = 0) cases: (a) no streamwise pressure gradient and (b) applied adverse streamwise pressure gradient.

## 4.2. Pulsed Jet Injection

### 4.2.1. Normal Injection

The results of normal, pulsed VGJs on a flat plate with an applied adverse pressure gradient are displayed in Figure 4-2. As in the zero pressure gradient case, three dimensional surface plots at $u = 0.8U_{inf}$ in the left column show the jet fluid while plots in the right column at $u = 0.5U_{inf}$ show the behavior of the boundary layer. The uncontrolled case is shown first (Figure 4-2a), followed by the respective flow fields for the eight phases within the pulsing cycle (Figure 4-2b-i).

The uncontrolled flow shown in Figure 4-2a coincides with the $c_p$ data found in Figure 2-4, as the separated zone (denoted by the dramatic rise in the $u/U_{inf} = 0.5$ surface) begins shortly after the jet injection point. This separated zone grows steadily through the flow domain, reaching a maximum thickness of about y/d = 3 at x/d =20.

The trajectory of the jet fluid can be clearly followed in Figure 4-2 (left column). The jet can be seen entering, traveling through, and leaving the flow field in Figures 4-2 b-d, respectively. When the off portion of the cycle is reached (Figures 4-2 e-f) there is still a residual disturbance in the flow as a result of the passage of the jet. This disturbance dies down and there is little change in the surface during the last three phases of the pulsing cycle (Figures 4-2 g-i).

The resulting boundary layer behavior is shown in the right column of Figure 4-2. At the start of the jet pulse (Figure 4-2b), the separated region is already significantly smaller than the uncontrolled case, a residual effect of the previous jet pulse. When the pulse is on (Figure 4-2c), the separated area can be seen beginning about 10 diameters downstream of the jet injection point and growing to a maximum thickness of about y/d =

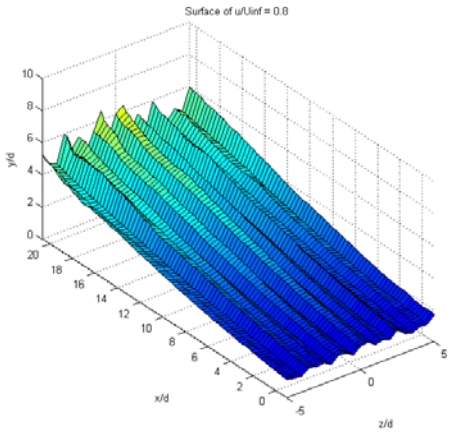


(a)
uncontrolled
B = 0

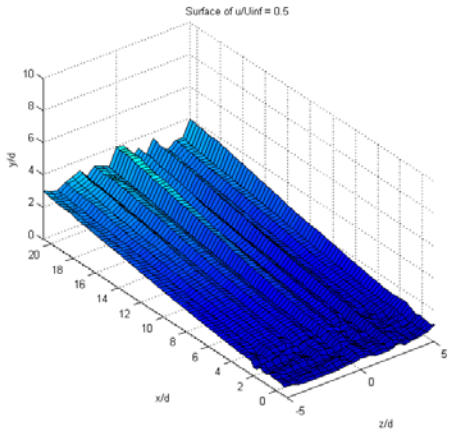


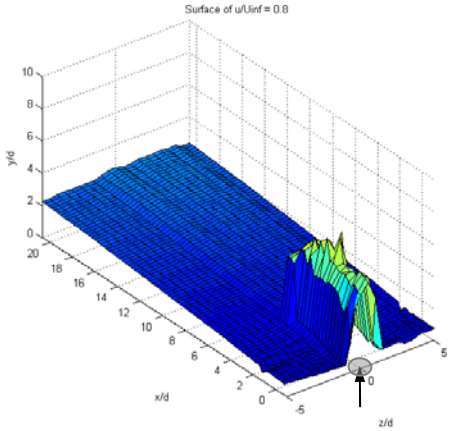


(b)
t/T = 0.025
Phase 1
pulse start

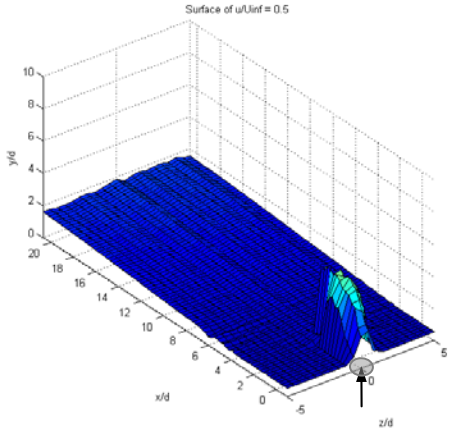


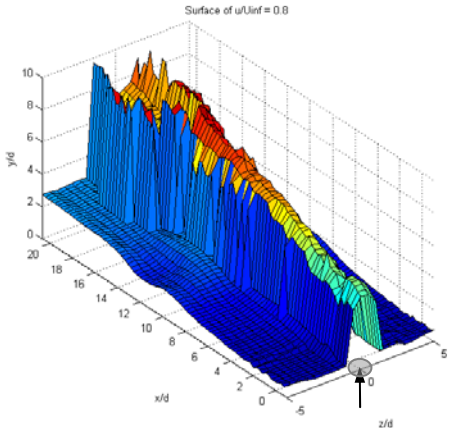


(c)
t/T = 0.150
Phase 2
pulse on

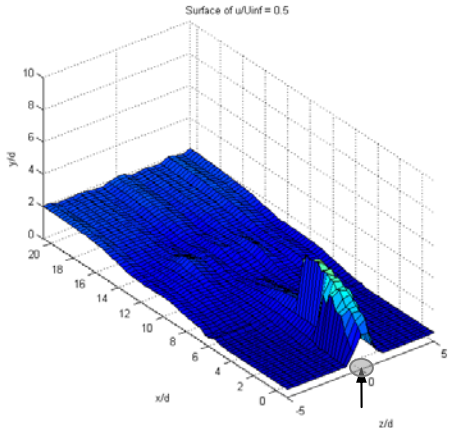

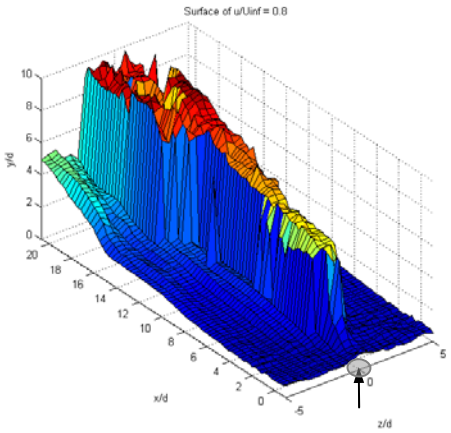


(d)
t/T = 0.275
Phase 3
pulse end

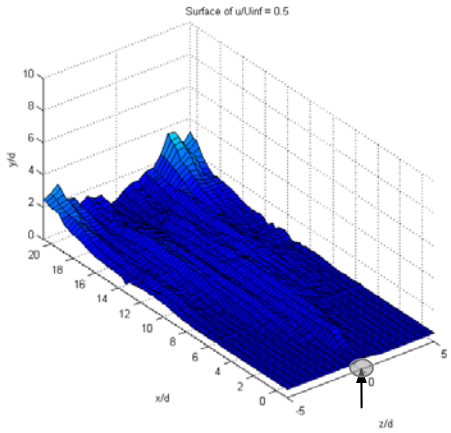


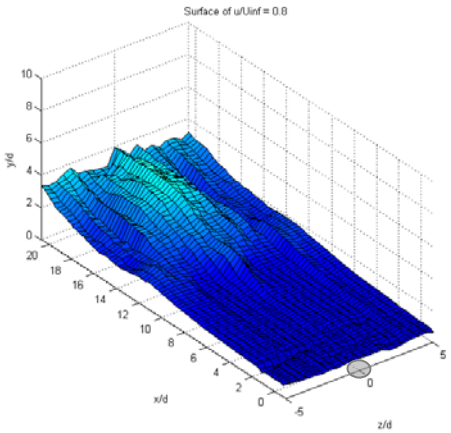


(e)
t/T = 0.400
Phase 4
pulse off

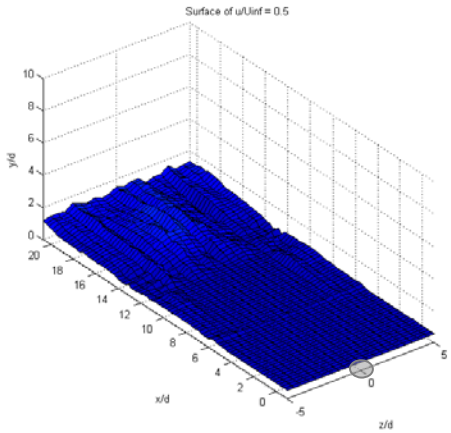


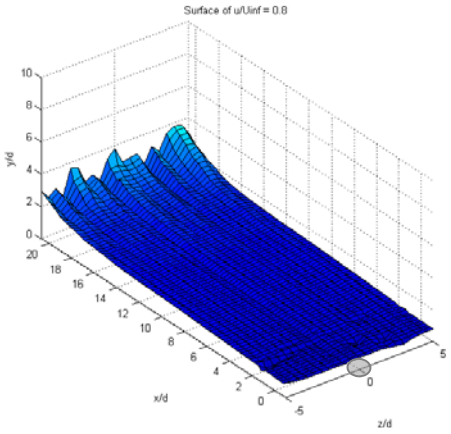


(f )
t/T = 0.525
Phase 5
pulse off

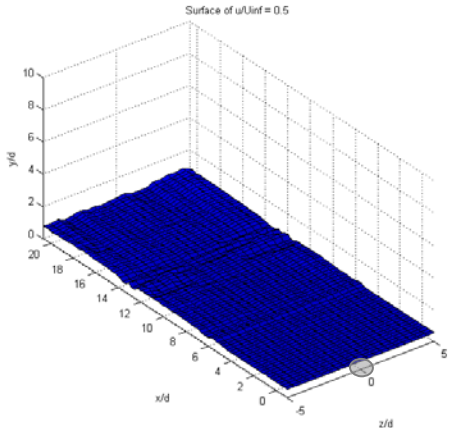

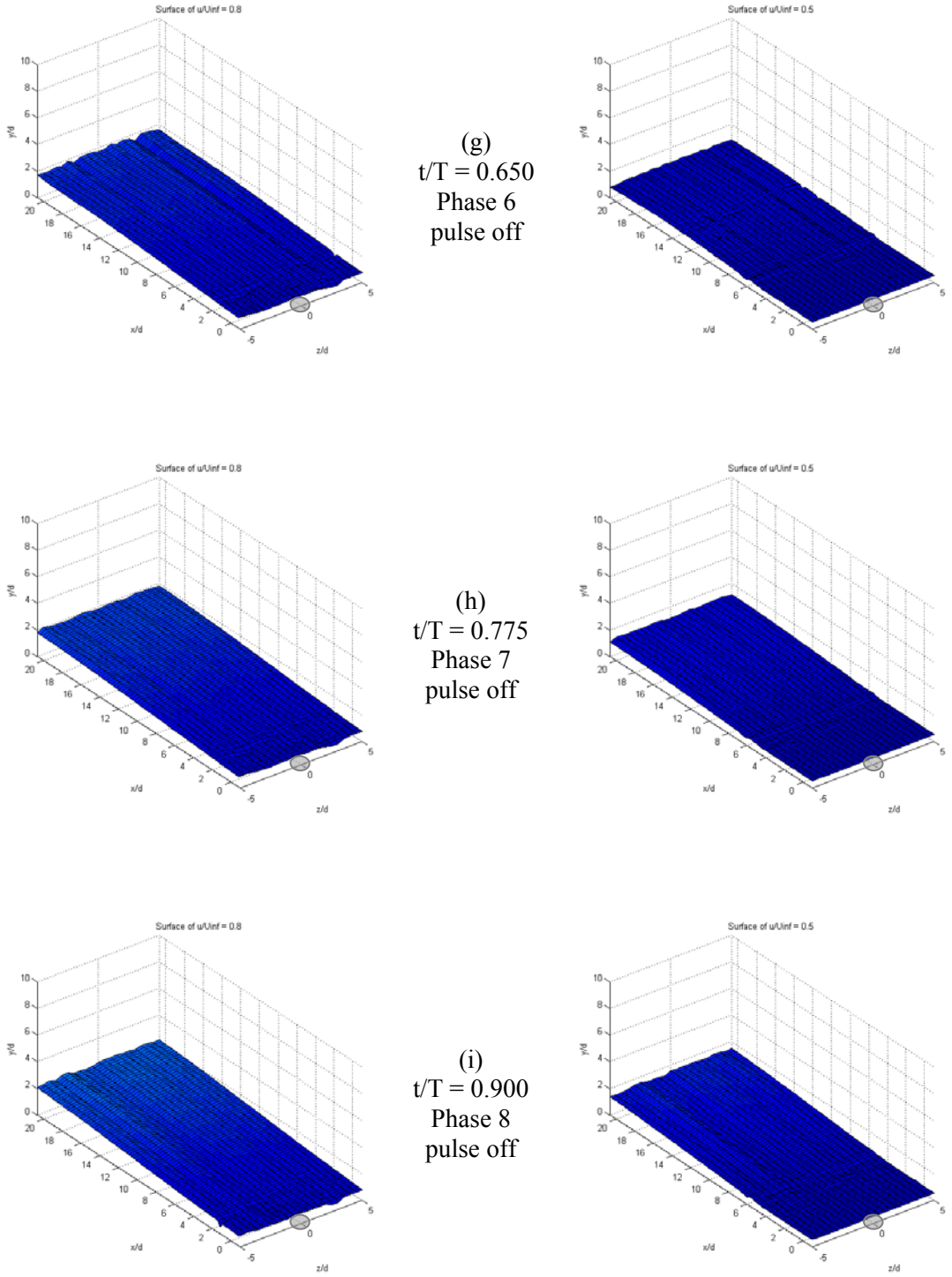


**Figure 4-2**. 3-D surfaces of streamwise velocity where $u = 0.8U_{inf}$ showing jet movement (left column) and $u = 0.5U_{inf}$ showing boundary layer behavior (right column) taken at 8 discrete points in the pulsing cycle. Pulsed, normal injection into applied streamwise pressure gradient at 5 Hz and 25% duty cycle with maximum B = 2.5. VGJ holes are shown as gray ovals, with black arrows indicating the presence and position of the jet pulse.

2 at the downstream end of the figure. This is the maximum extent reached by the separation zone before the next pulse traverses the entire flow domain. The subsequent reduction in size of the separated zone proceeds through the remainder of the pulse (Figure 4-2d) before almost completely disappearing (Figure 4-2g). It is not until the final phases (Figures 4-2 h-i) that the separation area begins to grow again, though it never reaches the uncontrolled state. The next pulsing cycle begins before the flow field can return to the uncontrolled condition.

### 4.2.2. Angled Injection

The effect of pulsed, angled VGJs is shown in Figure 4-3. Again, three dimensional surface plots of $u = 0.8U_{inf}$ (left column) and $u = 0.5U_{inf}$ (right column) are plotted to show the behavior of the jet and boundary layer fluid.

The general similarity between the normal and angled jet injection is evident in Figure 4-3. The disruption and subsequent increase in the boundary layer is evident while the jet pulse is passing through the flow field (Figures 4-3 b-d). As before, the boundary layer decreases to a minimum (Figure 4-3f) before slowly returning towards the uncontrolled state (Figures 4-3 g-i).

There are some differences between normal and angled jet injection, however, that are worth noting. First, during the "on" portion of the pulsing cycle (Figures 4-2c and 4-3c), the effect of the jet on the boundary layer is distinct for normal and angled jets. The normal jet causes a minimal effect on the boundary layer, while the angled jet reduces the extent of the separation by pushing the beginning of the separation zone back to x/d = 10. When the pulse is turned off (Figures 4-2d and 4-3d), both normal and

angled jets produce a significant reduction in the size of the separated area. A close inspection of the width of the boundary layer at the end of the flow domain shows an area of boundary layer control localized at z/d = 0 for the normal jets and a broader but less effective area of flow control for the angled jets. Also visible in Figure 4-3d is the familiar hump of low momentum boundary layer fluid being swept up by the vortical structures created in the flow. It is further evident that the normal jet travels more quickly as the tail end of the angled jet fluid is present in the flow domain for a longer period of time (Figures 4-2e and 4-3e). Finally, the boundary layer more quickly recovers from the disturbance caused by the angled jets than from the normal jets (Figures 4-2e and 4-3e).

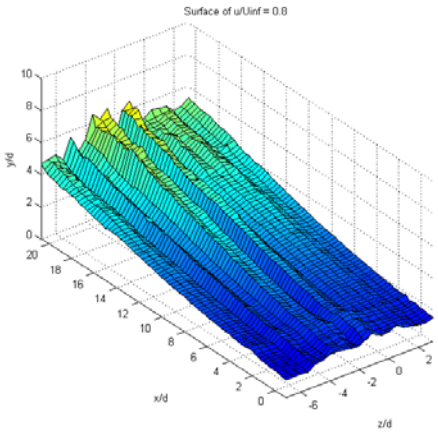


(a)
uncontrolled
B = 0

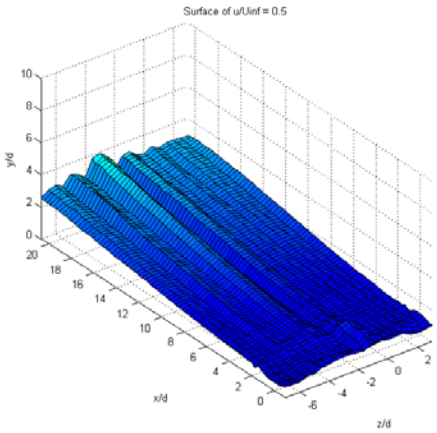


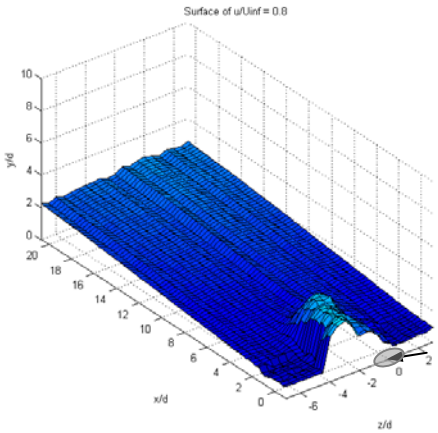


(b)
t/T = 0.025
Phase 1
pulse start

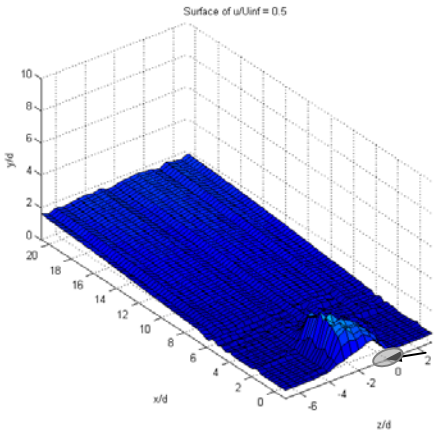


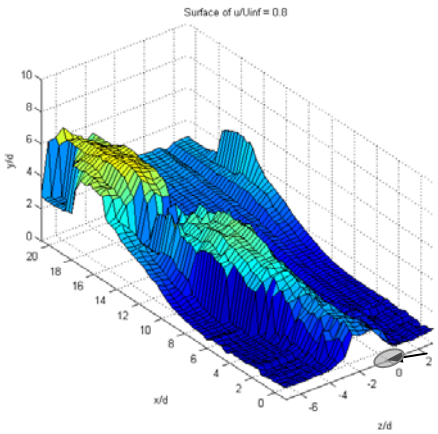


(c)
t/T = 0.150
Phase 2
pulse on

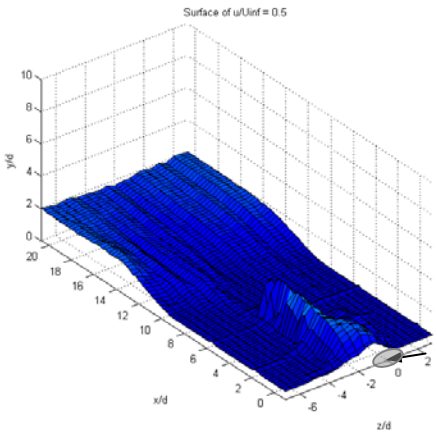

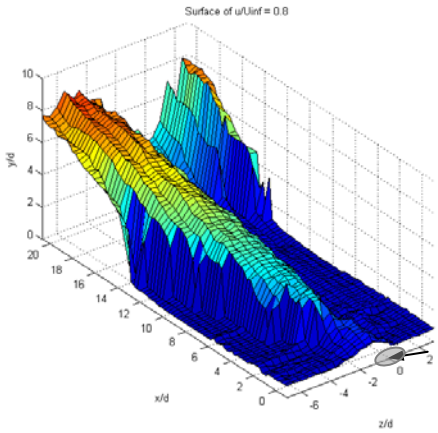


(d)
t/T = 0.275
Phase 3
pulse end

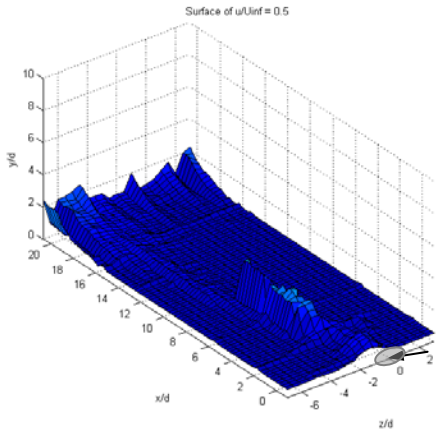


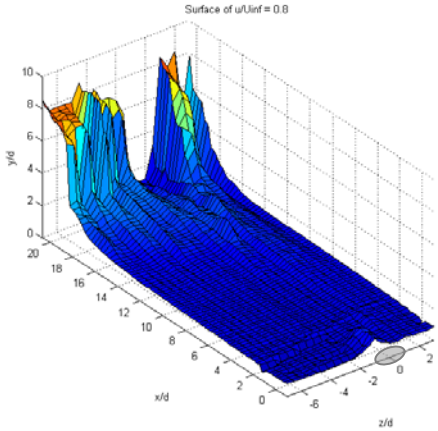


(e)
t/T = 0.400
Phase 4
pulse off

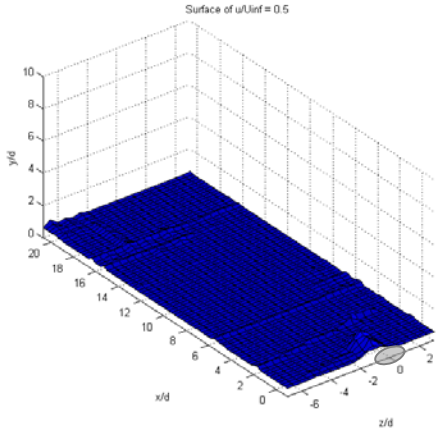


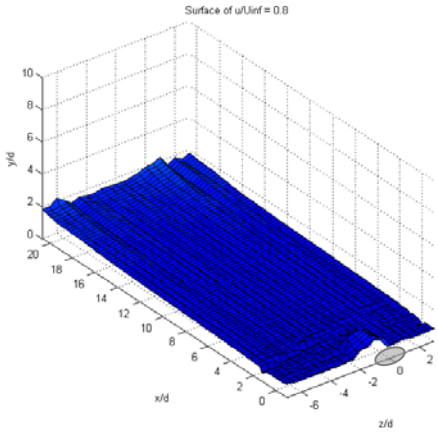


(f )
t/T = 0.525
Phase 5
pulse off

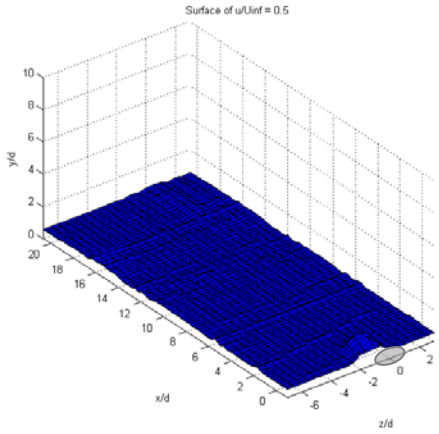

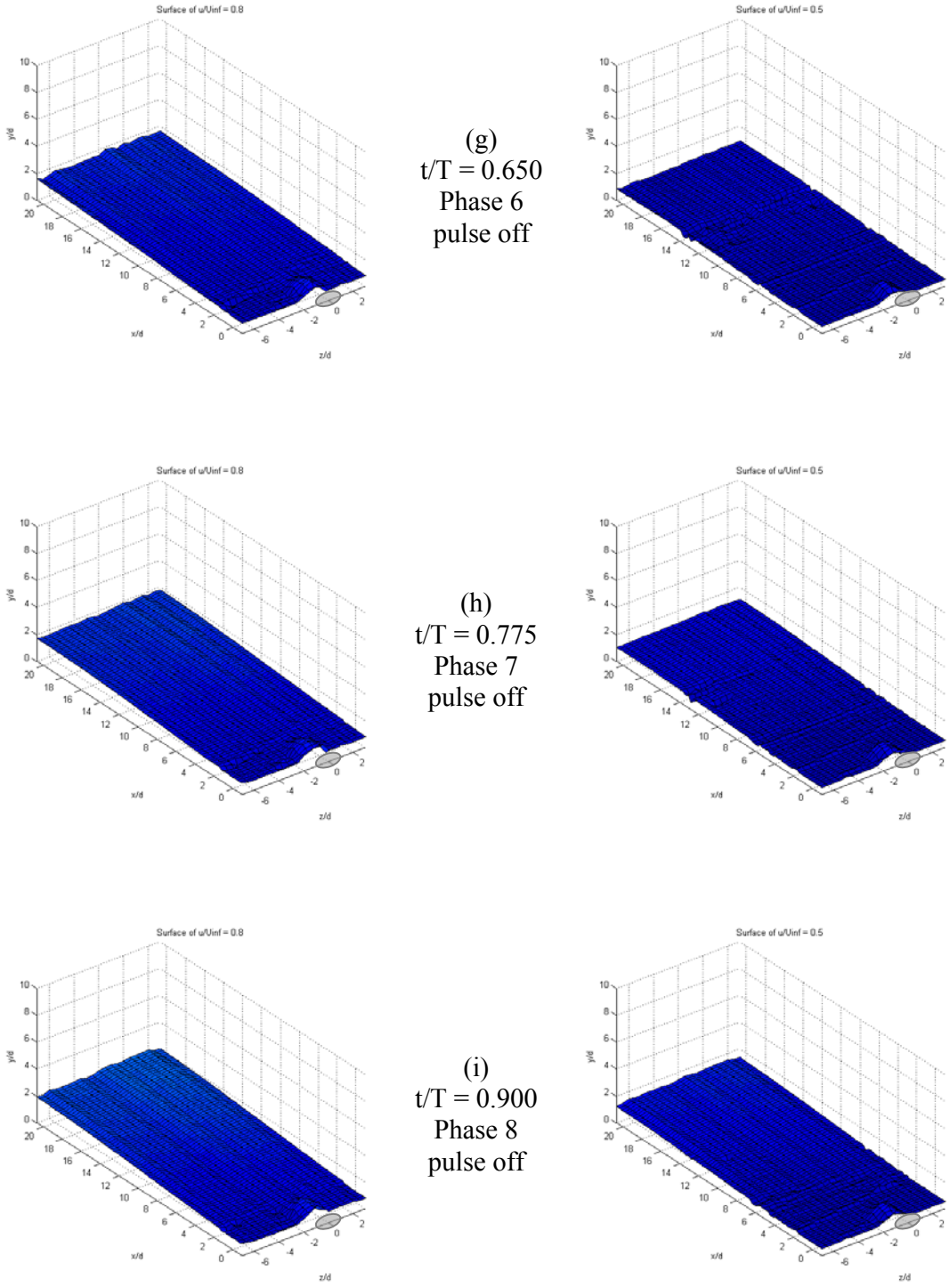


**Figure 4-3**. 3-D surfaces of streamwise velocity where u = $0.8U_{inf}$ showing jet movement (left column) and u = $0.5U_{inf}$ showing boundary layer behavior (right column) taken at 8 discrete points in the pulsing cycle. Pulsed, angled injection into applied streamwise pressure gradient at 5 Hz and 25% duty cycle with maximum B = 2.5. VGJ holes are shown as gray ovals, with black arrows indicating the presence and position of the jet pulse.

### 4.3. Loss Coefficient

In order to measure the effectiveness of the VGJs, it is important to quantify the boundary layer separation losses. Previous researchers have done this using integrated total pressure measurements across the wake of the turbine blade (Figure 4-4a).

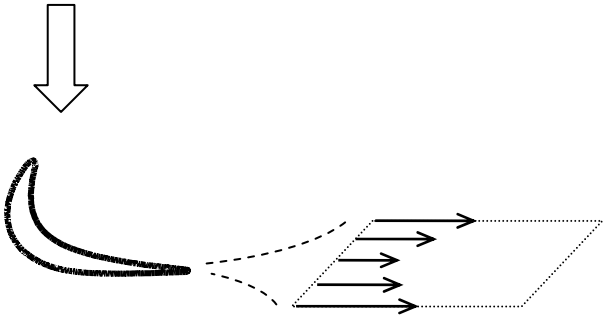

(a) Integrated wake loss pressure coefficient

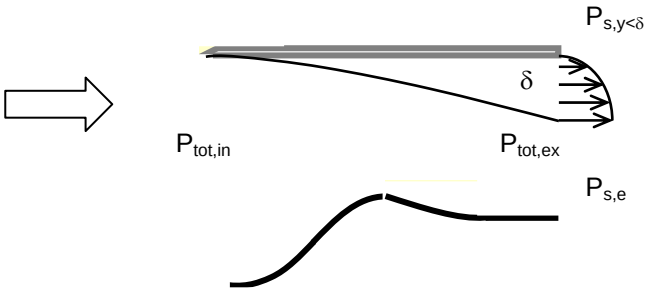


(b) Integrated boundary layer momentum flux coefficient

**Figure 4-4**. Schematics of loss coefficient calculation for a) wake loss and b) boundary layer

Since the flat plate/wedge test facility has no blade wake, a boundary layer parameter comparable to the integrated wake pressure loss coefficient, $\phi$ (Eq. 2), was evaluated.

$$\phi = \int_{mid-passage}^{mid-passage} \frac{P_{tot,i} - P_{tot,w}}{P_{tot,i} - P_{s,i}} dy \tag{2}$$

If the static pressure is assumed to be constant across the boundary layer and the total pressure in the freestream ($y>\delta$) is constant, $\phi$ can be written as $\Gamma$, Eq. 3, for low speed (incompressible), steady flow (Figure 4-4b). This modified version of the integrated wake loss coefficient is referred to in this study as the integrated boundary layer momentum flux loss coefficient.

$$\Gamma = \int_0^{\delta} \frac{u_e^2 - u^2}{u_i^2} dy \tag{3}$$

The calculation of $\Gamma$ is performed at the trailing edge of the PIV data domain using the spanwise averaged streamwise velocity data (for example, Figure 4-1). Figure 4-5 shows $\Gamma$ normalized by $\Gamma_o$ (the loss coefficient of the uncontrolled case) for each phase of the pulsing cycle. A normalized loss coefficient of 1 indicates that the measured separation losses are equivalent to those of the uncontrolled case. The pulsing cycle is also shown at the bottom of the figure for ease of comparison.

A complication in the interpretation of Figure 4-5 is encountered because of the time lag of the flow disturbance. The loss coefficient is calculated from the data taken at the farthest downstream point of the flow field (x/d = 20). Therefore, this data does not correspond in time with the jet pulse shown in the figure. For example, the loss coefficient calculated with the data taken during the first phase of the pulsing cycle is not

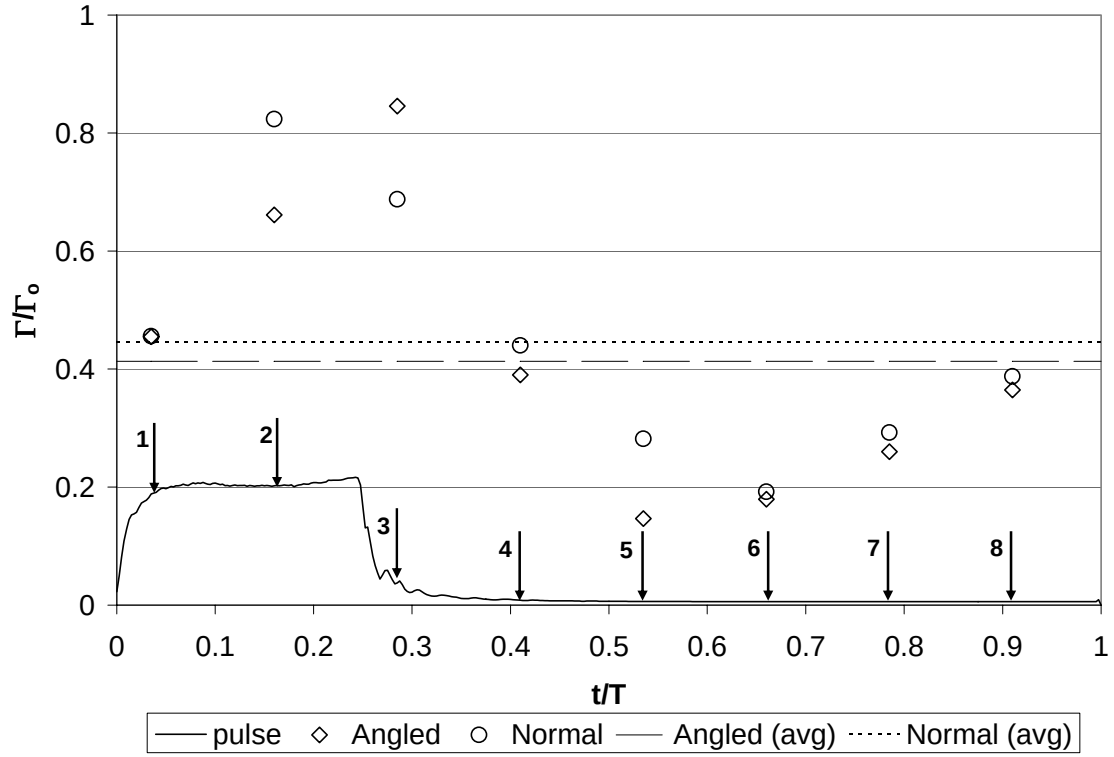


**Figure 4-5**. Integrated boundary layer momentum flux loss coefficient during the pulsing cycle. Normalized by the loss coefficient with B = 0. Pulsed injection into wedge flow at 5 Hz and 25% duty cycle.

indicative of the disturbance being caused at that moment by the initiation of the jet. Rather, it quantifies the losses associated with the preceding disturbance. Though the convective time of the disturbance is difficult to quantify precisely, it is roughly equivalent to $t/T \approx 0.1$ in Figure 4-5. So, the effect of the pulse shown in the lower part of the figure appears at the trailing edge ($x/d = 20$) approximately $t/T \approx 0.1$ later.

There are several observations that can be made from Figure 4-5. First, there appears to be very little difference in the cycle-averaged loss coefficient for both jet orientations; each has a value slightly greater that 0.4. Although the cycle-averaged loss coefficient for the angled jet is lower than that calculated for the normal jets, the

difference is small, suggested that neither orientation has a significant advantage over the other for these flow conditions.

It is evident from Figure 4-5 that the angled and normal jet configurations produce similar disturbances (as previously noted in the surface plots of Figures 4-2 and 4-3). The loss coefficient is increasing sharply when the jet fluid enters the domain, and then decreases as the jet influence is felt downstream. The latter end of the pulsing cycle is characterized by a gradual return to uncontrolled conditions.

Of particular interest are the relative convection speeds of the disturbance. Figure 4-5 shows that the decline in loss coefficient calculated from the normal jets occurs sooner than the corresponding reduction from the angled jets. By phase 2, while the jet pulse is still on, the loss coefficient for the normal jets reaches a maximum, and proceeds to decline during the following three phases. The angled jets do not reach a maximum loss coefficient until phase 3. This behavior is reasonable when considered in terms of the steady jet migration discussed earlier. The steady normal jets (Figure 3-2) penetrated twice as far out from the wall as the angled jets (Figure 3-5). Thus, the normal jets are carried out farther towards the higher velocity freestream flow. Meanwhile, the angled jets remain closer to the wall and the low velocity boundary layer fluid, where they are convected downstream at a slower speed.

Although the normal jet flow control is carried downstream at a faster velocity, Figure 4-5 (with 4-2e and 4-3e) suggests that the angled jet flow control is more effective because it provides control of the same magnitude within a shorter period of time. This is seen by the speed at which the loss coefficient is reduced from its maximum to minimum state. The angled jets have a much steeper decline in loss coefficient, as the maximum-

to-minimum reduction is completed in only two phases (phases 3-4). The normal jets, however, require four phases (phases 2-6) to reach the minimum loss coefficient.

The more rapid control generated by the angled jets may be related to the stronger streamwise vorticity development observed in the steady jet data. The jet-induced boundary layer thickening in Figure 4-3d was seen previously in Figures 3-8 and 3-9 b-d and is evidence of streamwise vortex generation. This feature is not as prominent as it was for the flat plate case (Figure 3-9 b-d), suggesting that the separating boundary layer may lift the vortex away from the wall, possibly reducing its effectiveness. The normal jet injection surface at the same t/T (Figure 4-2d) also shows evidence of a boundary layer disturbance in the wake of the injected jet. In this case, the surface shows a double hump directly downstream of the jet injection location, from $6 < x/d < 16$. Clearly, this is due to the formation of a double vortex, as seen in the steady jet data (Figure 3-1). Beyond $x/d = 16$, the $u/U_{inf} = 0.5$ surface is brought down to the wall, indicating a strong boundary layer reattachment before the trailing edge of the data domain. By comparison, the angled jet surface shows a much broader spatial influence of the jet vortices.

## 4.4. Summary

Before proceeding with the more complex three-blade cascade, it is helpful to summarize what has been learned from the flat plate cases.

Data have shown that steady jets produce vortical structures that grow in size while decreasing in strength as they travel downstream. For normal jets, a double vortex develops with rotations of equal magnitude and opposite sign, while the angled VGJs produce a single dominant vortex. It is clear that the normal jets penetrate out from the

wall twice as far as the angled jets while maintaining the same spanwise position. The angled jets, however, migrate significantly in the spanwise direction. The vortex created by the normal VGJs deteriorates faster as the vorticity is reduced by 75%, while the vorticity generated by the angled jets is only reduced by about 50% at the same position. Because the angled vortex is located closer to the wall and remains a coherent structure for a longer distance, it is concluded that the angled VGJs have greater potential for flow control through freestream entrainment than the normal VGJs.

Pulsed jets show improved flow control capabilities. Both normal and angled jets provided similar cycle-averaged separation reduction, suggesting that it is not the orientation of the jet, but rather the disturbance created by the pulsing that best controls the flow. However, the different jet orientations do produce distinct disturbances. Since the normal jets penetrate farther out into the higher momentum freestream flow, the flow-controlling mechanism is carried downstream at a faster rate. The vortex created by the angled VGJs remains closer to the wall, so although its effect travels downstream more slowly, it can provide the same amount of flow control in a shorter period of time.

# 5. THREE-BLADE CASCADE

## 5.1. Separation Bubble Analysis (B = 0)

Before the effects of the VGJs on the boundary layer separation could be studied, the extent of the separation bubble produced by the L1M cascade had to be determined. PIV measurements were made at Reynolds numbers of 20,000 and 50,000 for the uncontrolled (B = 0) case. These are the same operating conditions used for the cascade $c_p$ data shown in Figure 2-6. Contour plots depicting these results are shown below in Figure 5-1. The plots represent spanwise averages of velocity magnitude normalized by the cascade inlet velocity. The flow is from left to right and the black mask in the upper left corner is due to the blocking of the laser sheet by the trailing edge of the adjacent blade. The black area along the lower edge of Figure 5-1 is the approximate contour of the L1M blade (compare to Figure 2-9) from 50% $c_x$ to the trailing edge. The apparent jagged surface of the blade contour is due to the masking algorithm of the PIV system. Because of surface reflections in the near wall region, data could only be gathered starting at about 2mm (roughly one jet diameter) from the blade surface.

Both the Re = 50,000 and 20,000 cases show the expected acceleration of the flow as it passes around the blade. The area of low velocity near the wall just following the peak passage velocity suggests the presence of flow separation. The extent of the separation is clearly larger for the Re = 20,000 case, as the separation begins earlier on the blade and the suction surface wake is substantially increased. Corresponding contour

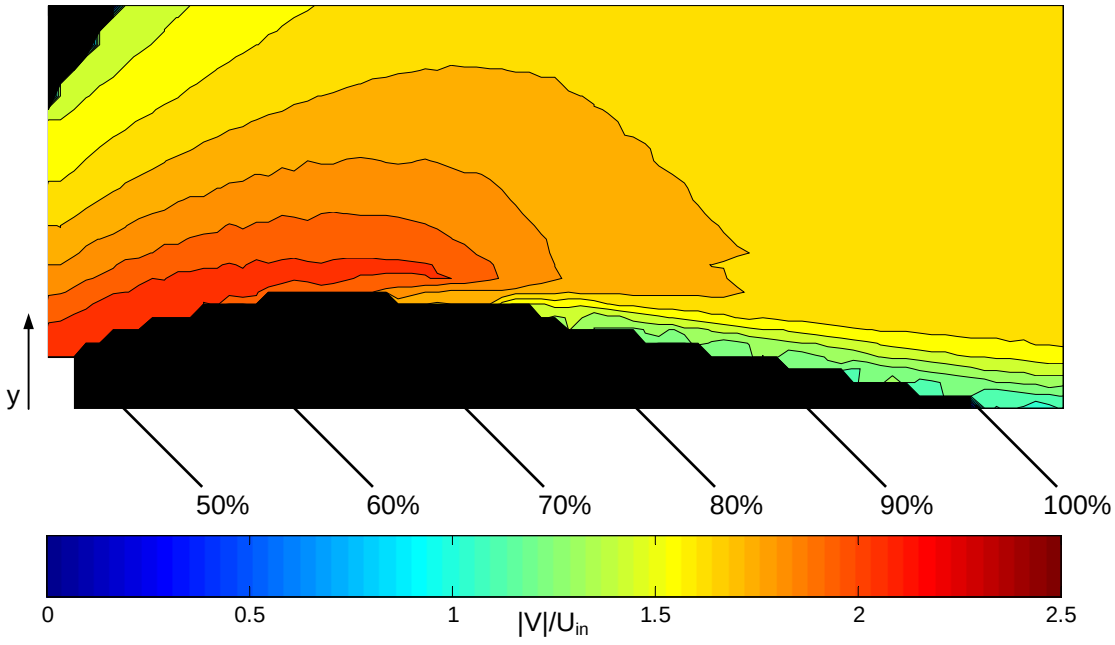


(a) Velocity magnitude contours for Re = 50,000.

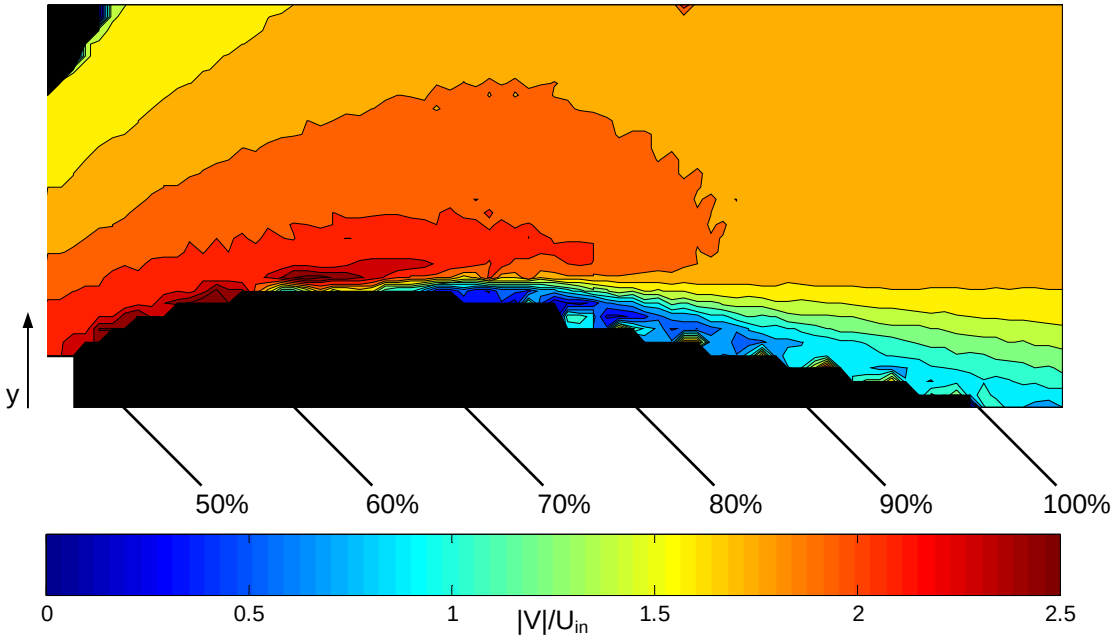


(b) Velocity magnitude contours for Re = 20,000.

**Figure 5-1**. Spanwise averaged contour plots of velocity magnitude normalized by cascade inlet velocity for B=0 at a) Re=50,000 and b) Re=20,000. A mask covering the blade is visible in the bottom of the plots. Data are presented looking up the span of the blade in the –z direction.

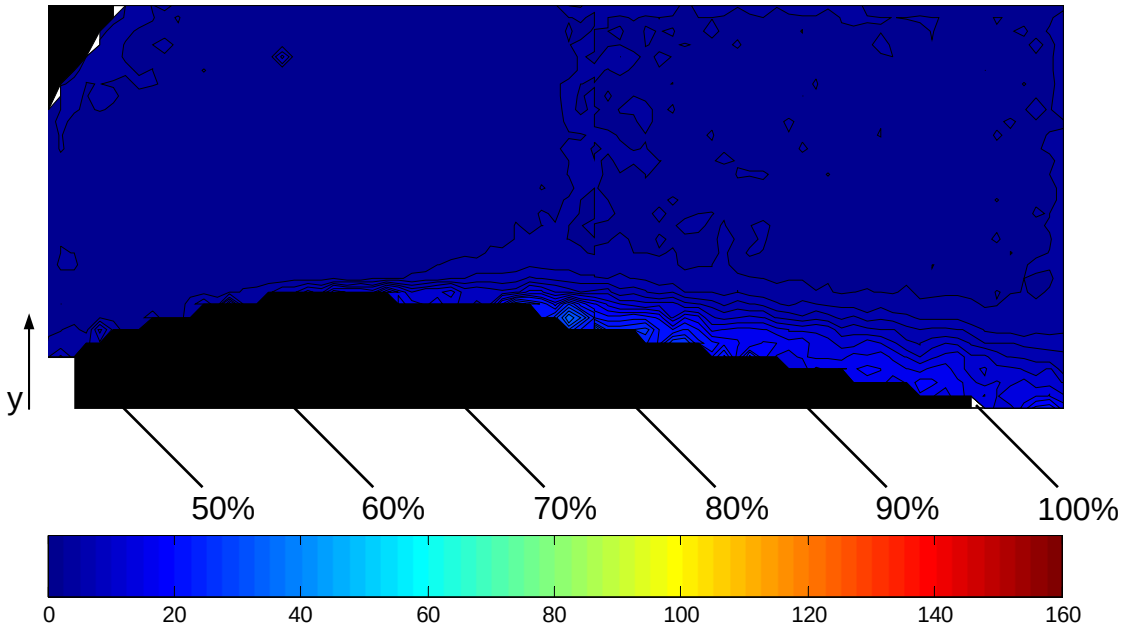


(a) Turbulence contours for Re = 50,000.

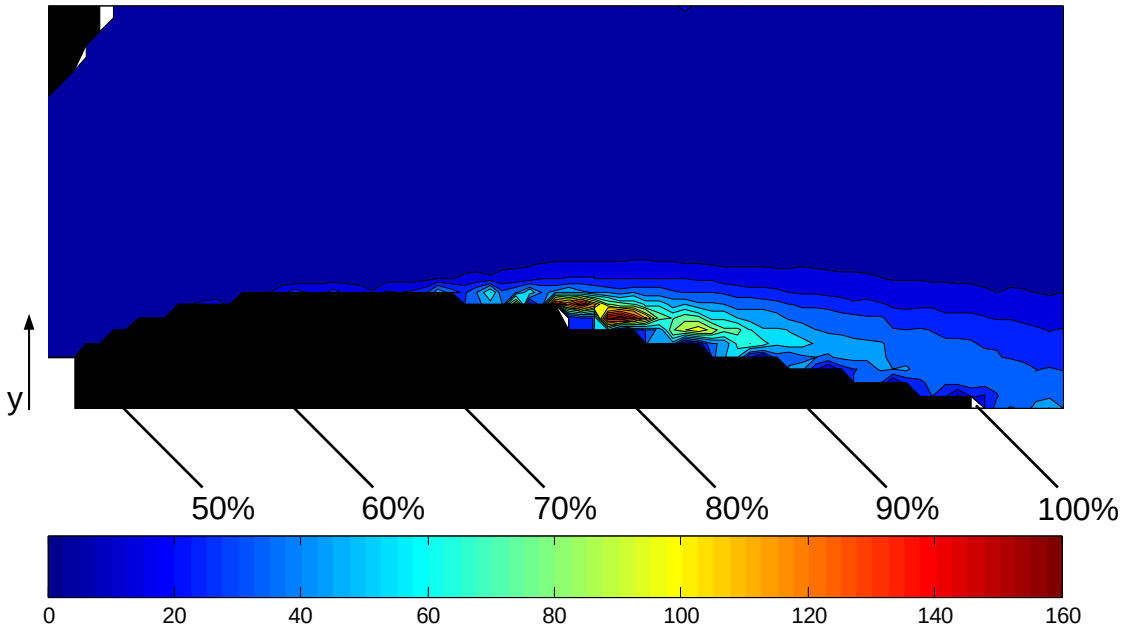


(b) Turbulence contours for Re = 20,000.

**Figure 5-2**. Spanwise averaged contour plots of turbulence levels for B=0 at a) Re=50000 and b) Re=20000. A mask covering the blade is visible in the bottom of the plots. Data are presented looking up the span of the blade in the –z direction.

plots of local turbulence level ($u'/U_{loc}$) shown in Figure 5-2 highlight this region of unsteady, separated flow.

Although Figures 5-1 and 5-2 are instrumental in providing an overall picture of the extent of the separation around an LPT blade, further detail is necessary to quantify the behavior of the boundary layer in this complicated flow. Specifically, it would be helpful in future LPT design to be able to establish criteria by which the extent of the separation bubble and the points of transition to turbulence can be determined. Separation and transition are both complex flow characteristics, and thus they are difficult to quantify precisely; however, the following discussion describes the efforts made to do so.

Figure 5-3 shows the velocity profiles generated at Re = 20,000 at 36 chord positions between the jet injection point (50% $c_x$) and the trailing edge of the L1M blade (100% $c_x$). The velocity values have been normalized by the cascade inlet velocity as before. The position of the blade has also been subtracted from the plots, so that the abscissa represents the blade surface, with each velocity point placed at its relative y/d-position out from the blade. Due to the masking algorithms of the PIV system, the range at which the first velocity vector closest to the blade was determined went from between about 1mm to 3.9mm from the surface. It is for this reason that the first data point for each velocity profile in Figure 5-3 appears at a different y/d position.

The plots in Figure 5-3 show the development of the uncontrolled flow as it separates, transitions from laminar to turbulent and reattaches to the blade surface. The laminar boundary layer at 50% $c_x$ is evident, with a shear layer remaining close to the blade surface. Between 60% and 70% $c_x$, inflection points begin to develop in the

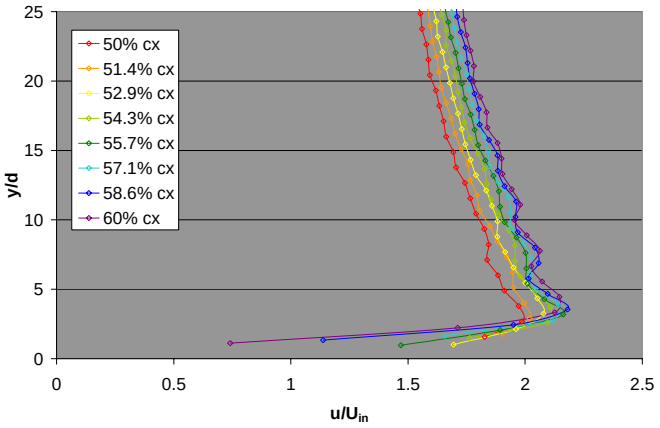


(a) 50% to 60% $c_x$

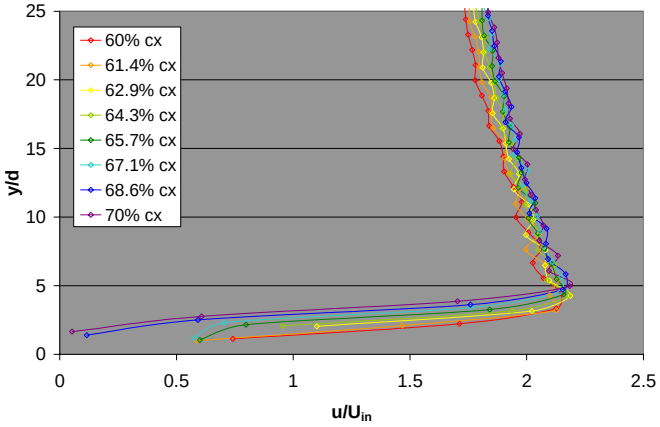


(b) 60% to 70% $c_x$

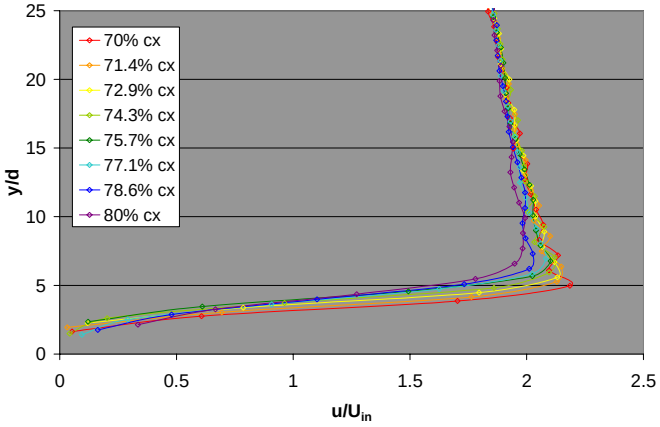


(c) 70% to 80% $c_x$

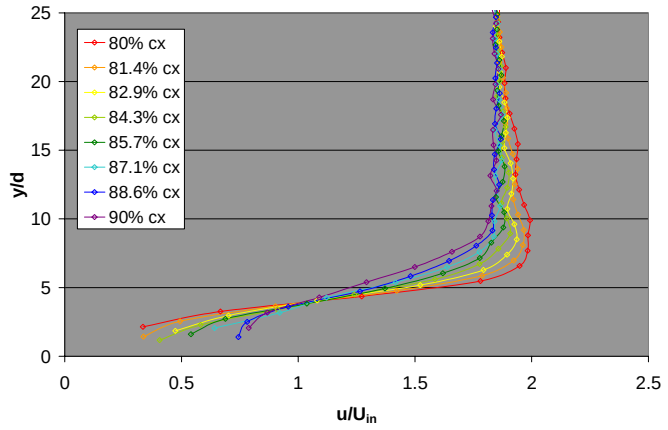


(d) 80% to 90% $c_x$

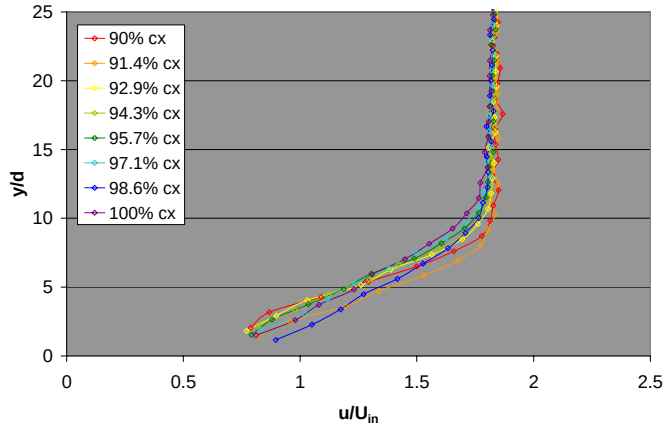


(e) 90% to 100% $c_x$

**Figure 5-3**. Plots of $u/U_{in}$ for Re = 20,000 at chord positions between 50% and 100% $c_x$.

velocity profiles, indicating the potential for the development of instabilities in the flow, resulting in a transition to turbulence. After 70% $c_x$, the flow is likely separated, as the velocity profiles suggest the possibility of reverse flow at the wall (though it could not be measured). By the trailing edge of the blade, it is clear that the flow has become turbulent, as the boundary layer has grown substantially and is fuller.

Analogous to Figure 5-3 are $u/U_{in}$ profiles for a Reynolds number of 50,000 shown in Figure 5-4. Again the thin shear layer at 50% $c_x$ indicates laminar flow, and the inflection points seen after 60% $c_x$ designate the possibility of separation. The flow is also turbulent by the trailing edge of the blade, although the boundary layer is not as large at Re = 50,000 as it was for Re = 20,000 (see Figure 5-3e).

In spite of the instructive nature of the velocity profiles in Figures 5-3 and 5-4, the points of flow separation and reattachment remain somewhat elusive. This is due in part to the scarcity of data points in the near-surface region. The following procedure was used to determine, at least approximately, the position of the separation bubble. A linear least-squares fit was made to the velocity points from the surface to the edge velocity (point of maximum velocity in the profile) at each chord position. A linear fit was chosen because of its simplicity and adequate approximation of the shear layer. This line was extrapolated to the surface in order to approximate the likely near-wall values of velocity that could not be measured experimentally. The value of $u/U_{in}$ at which the trend line crossed the y = 0 line, named $(u/U_{in})_{ext}$, was then plotted for each chord position as demonstrated in Figure 5-5. It is important to note that the extrapolation procedure used does not suggest that the velocity is not equal to zero at the wall; rather, it is simply an indication as to whether the profile suggests forward or reverse flow in the near-wall region.

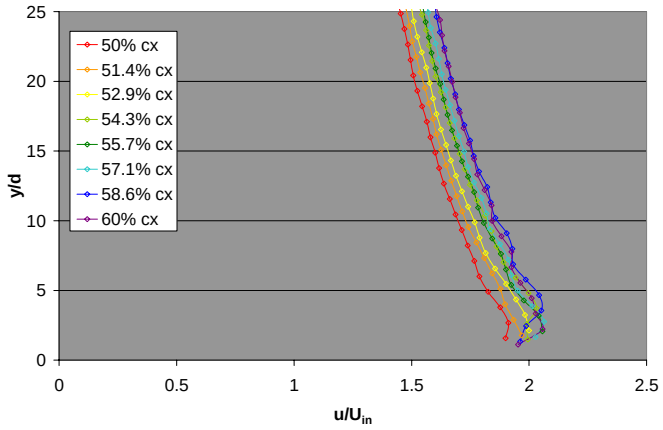


(a) 50% to 60% $c_x$

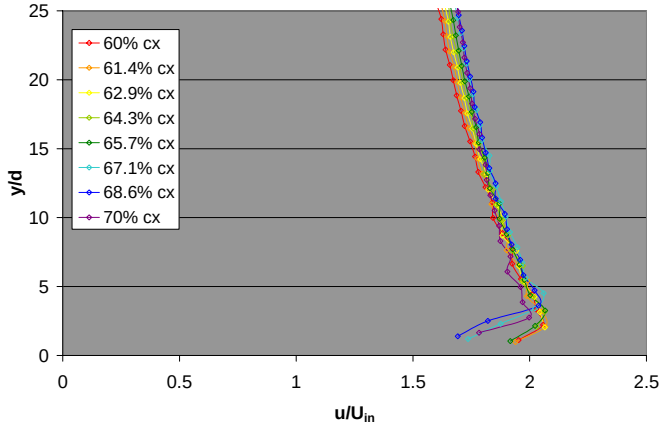


(b) 60% to 70% $c_x$

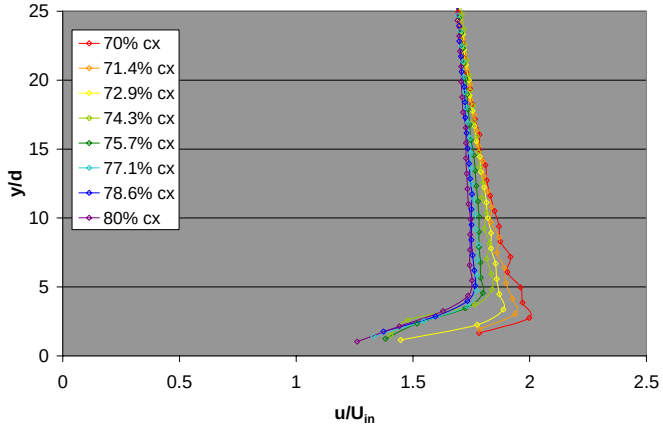


(c) 70% to 80% $c_x$

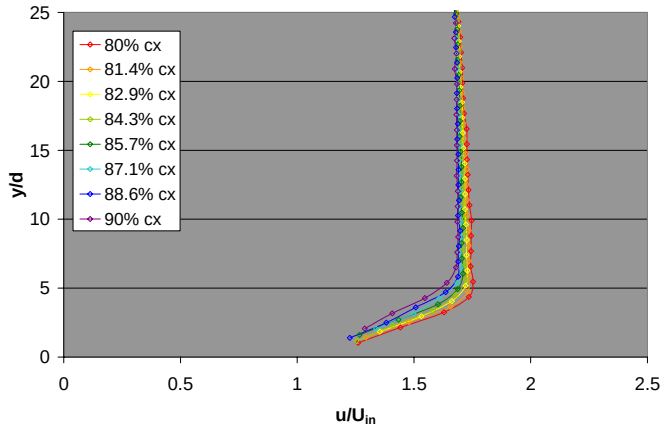


(d) 80% to 90% $c_x$

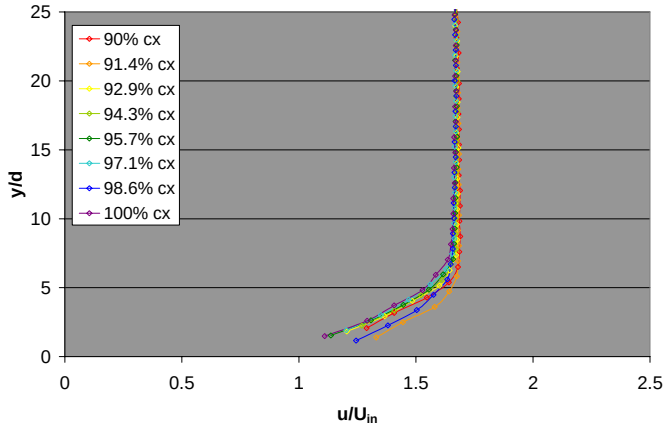


(e) 90% to 100% $c_x$

**Figure 5-4**. Plots of $u/U_{in}$ for Re = 50,000 at chord positions between 50% and 100% $c_x$.

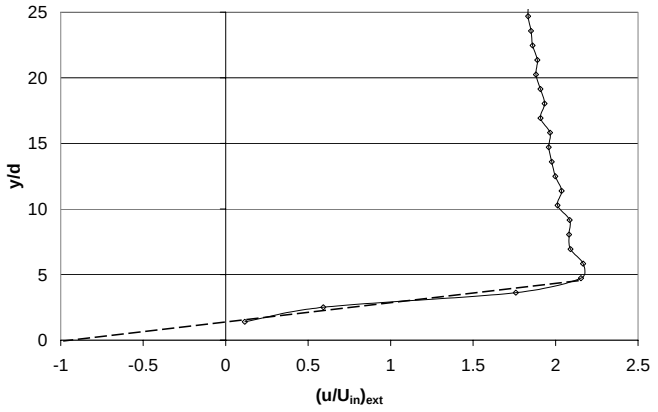


(a) $(u/U_{in})_{ext} < 0$

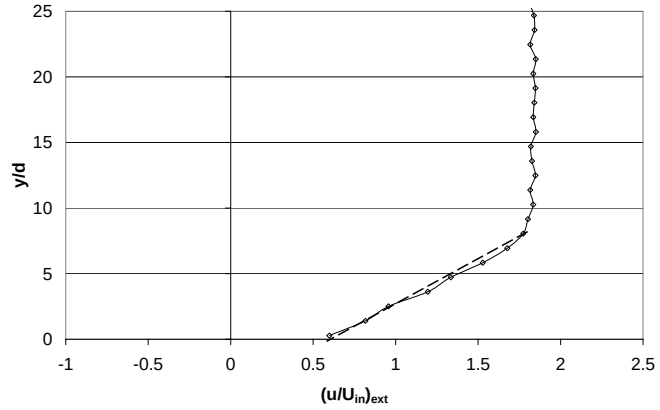


(b) $(u/U_{in})_{ext} > 0$

**Figure 5-5**. Example of linear least-squares fit used to determine the value of $u/U_{in}$ extrapolated to the surface

The results of this extrapolation procedure are shown in Figure 5-6, where the value of $(u/U_{in})_{ext}$ at both Reynolds numbers is plotted for each chord position. For Re = 20,000, $(u/U_{in})_{ext}$ is positive at 50% $c_x$ and gradually decreases as the flow at the surface of the blade slows down. At 61% $c_x$, the value of $(u/U_{in})_{ext}$ becomes negative, suggesting the presence of a reverse flow area close to the blade surface. $(u/U_{in})_{ext}$ remains negative

until 83% $c_x$, where it becomes positive again, and remains positive for the remainder of the flow domain. This analysis yields the result that separation begins at 61% $c_x$, with reattachment occurring at 83% $c_x$. This estimation of the separation bubble length is surprisingly consistent with the $c_p$ data (Figure 2-6) where the separation bubble was defined between about 60% and 86% $c_x$.

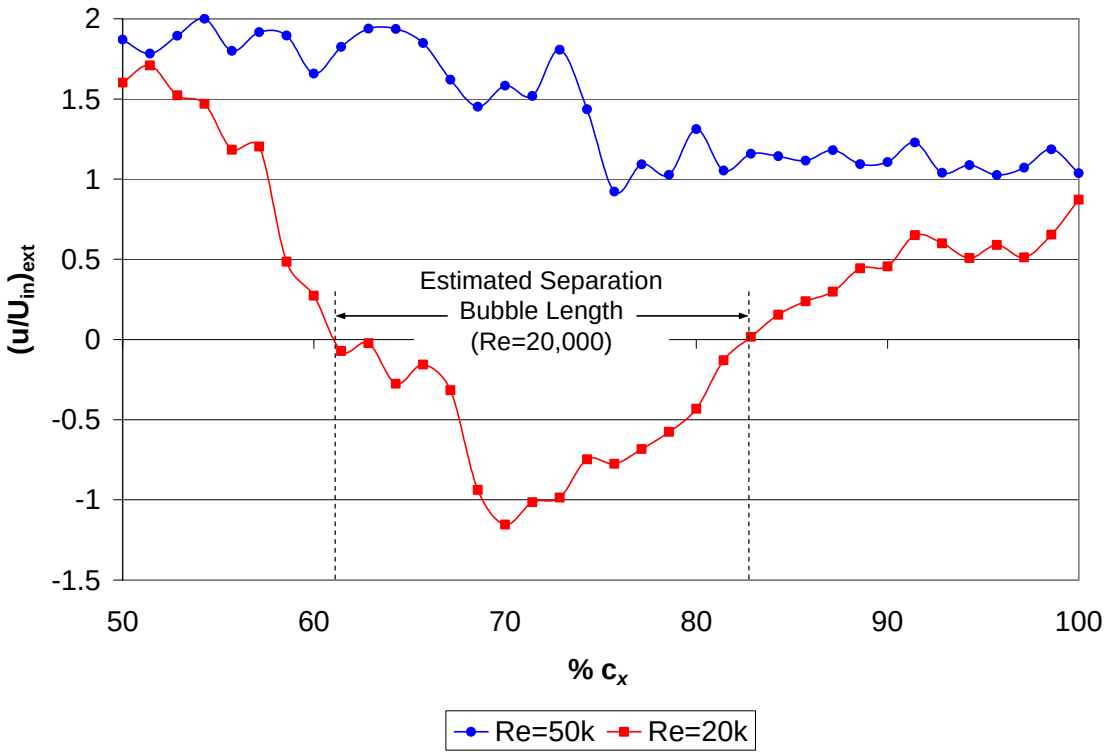


**Figure 5-6**. Values of $u/U_{in}$ extrapolated to the blade surface at chord positions between 50% and 100% $c_x$ for Re = 50,000 and 20,000.

Figure 5-6 also shows the extrapolated $u/U_{in}$ values at Re = 50,000. In contrast to the lower Reynolds number case, $(u/U_{in})_{ext}$ never crosses zero. Because the $c_p$ measurements (Figure 2-6) clearly indicate the presence of separated flow, the results of

the extrapolation suggest that the process used to approximate the length of the separation bubble is less effective at higher Reynolds numbers.

The shape factor, H, provides support to the conclusions drawn from Figure 5-6. The shape factor is defined as the ratio of the displacement thickness to momentum thickness, and can be used to determine the susceptibility of a flow to separation. An increase in shape factor indicates the increasing susceptibility to separation of the flow. For example, a laminar boundary on a flat plate has a shape factor of 2.59, which is higher than the corresponding shape factor of 1.25 for a turbulent boundary layer. The Falkner-Skan flow with incipient separation has a shape factor of 3.94.

The shape factor is evaluated by first determining the displacement and momentum thicknesses according to the following equations:

$$\delta^* = \int_0^{y_e} (1 - \frac{u}{U_e}) dy \tag{4}$$

$$\theta = \int_0^{y_e} \frac{u}{U_e} (1 - \frac{u}{U_e}) dy \tag{5}$$

These parameters were calculated using spanwise averages of $u/U_e$ profiles and the integration was performed numerically using the trapezoid method. The limits of integration extended from the point of maximum velocity (edge velocity) to the wall. The results of the shape factor calculation are shown in Figure 5-7. The shape factor was not able to be calculated until about 60% $c_x$ because of the thinness of the boundary layer and the scarcity of data points in the near-wall region.

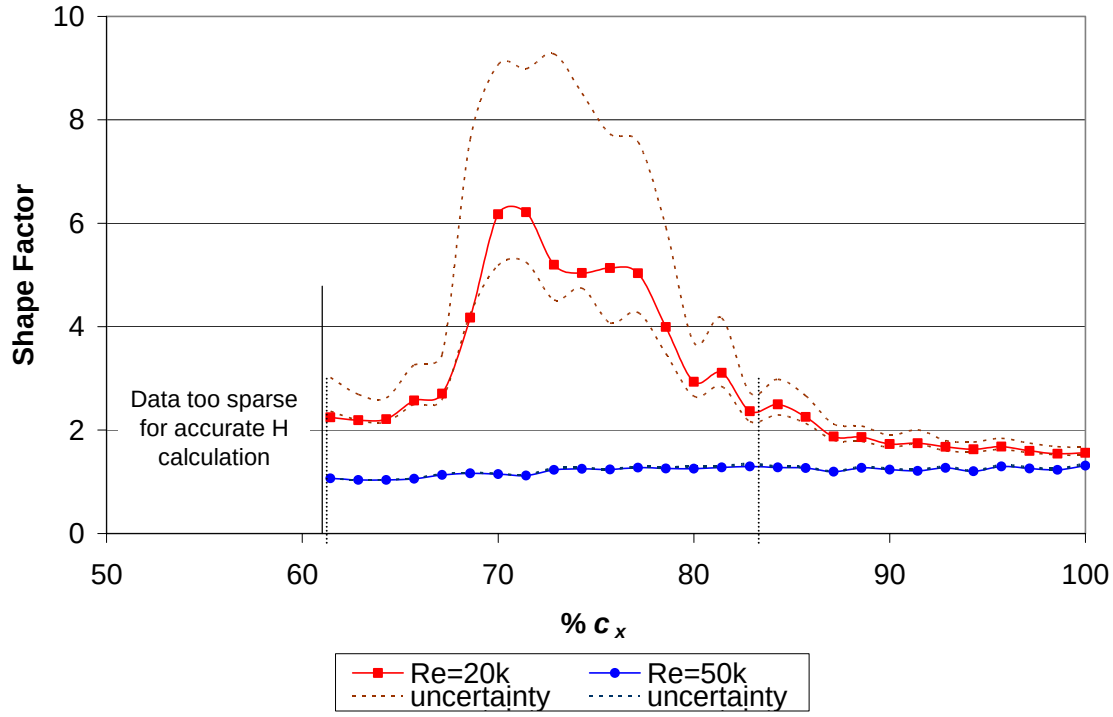


**Figure 5-7**. Shape factor for Re = 50,000 and 20,000 at chord positions from 50% to 100% $c_x$. The estimated separation bubble length for Re = 20,000 determined from Figure 5-6 is noted by the dashed black lines.

At a Reynolds number of 20,000, an increase in shape factor can be seen to begin at about 65% $c_x$, and it increases to a maximum value of 6.5 at 70% $c_x$. The shape factor remains high, indicating that the flow is separated, until decreasing to a final stable value of 1.6. The calculation of the shape factor supports the previous estimated length of the separation bubble, as the increase and decrease of the shape factor coincide with the estimated separation (at 61% $c_x$) and reattachment (at 83% $c_x$) positions.

Separation does not appear to occur for a Reynolds number of 50,000, as the shape factor remains nearly constant across the blade. Again, it is expected that this method of estimating the position of the separation bubble is not as effective for the

higher Reynolds number case. Thus, it was decided to do all further testing and analysis at a Reynolds number of 20,000, as the effect of the VGJs would be more prominent, and likewise easier to measure, on a more separated flow.

Also of interest in Figure 5-7 are the shape factors at the separation and attachment points (at Re = 20,000). It appears that the shape factors at the edges of the separation bubble are roughly equivalent, and that the maximum shape factor occurs near the starting point of transition. This behavior was also found by McAuliffe and Yaras[20] in a study of separation bubble transition over an airfoil at low Reynolds numbers. Whether this is a more general result is as yet unknown; however, future research in this area may provide further understanding of this curious peculiarity.

Another parameter helpful in analyzing the flow around the LPT blade is u', the fluctuating component of the streamwise velocity, which is defined as

$$u' = \sqrt{\frac{1}{n-1}\sum_{i=1}^{n}(u_i - u_{avg})^2}\ . \qquad (6)$$

The presence of turbulent fluctuations can be used to determine if a boundary layer is laminar, transitioning, or turbulent. Laminar boundary layers have low fluctuations because of the relative stability of the flow. Conversely, turbulent boundary layers are characterized by high levels of u' close to the surface, with corresponding high u' values extending out from the wall through the boundary layer. Transition can be identified by a dramatic increase in u' as the laminar flow becomes increasingly unsteady. When transition occurs in a separated shear layer, these high u' levels grow away from the surface and then spread back towards the surface, eventually causing reattachment. It is

understood that an average of only forty images is unlikely to produce very accurate u' values. However, the trends that can be seen in u' as the flow progresses downstream are useful in determining transition.

Figure 5-8 shows u' normalized by the boundary layer edge velocity at the same chord locations used previously. As expected, the data suggest a laminar boundary layer at 50% $c_x$, as the u' values in the near-surface region are very low. Transition to turbulence begins to develop between about 55% and 65% $c_x$, just after the separation location in Figure 5-6, as the u' values start to increase significantly in the separated shear layer. This transition continues to 85% $c_x$ (Figure 5-8 b-d) where the turbulent fluctuations begin to increase more rapidly and spread down to the surface. After 85% $c_x$ (Figure 5-8 d-e), the turbulent boundary layer is reattached and u' grows with increasing distance from the blade surface.

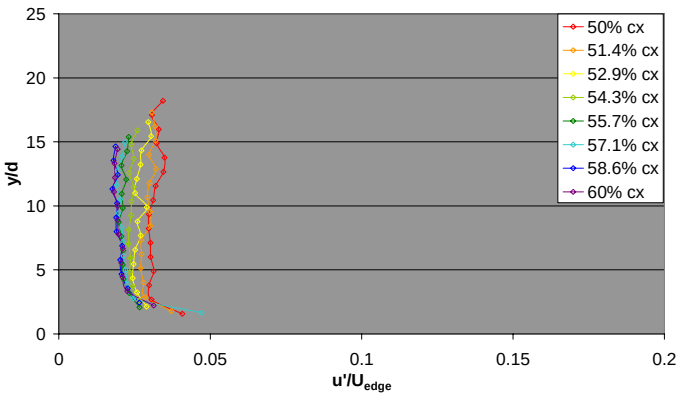


(a) 50% to 60% $c_x$

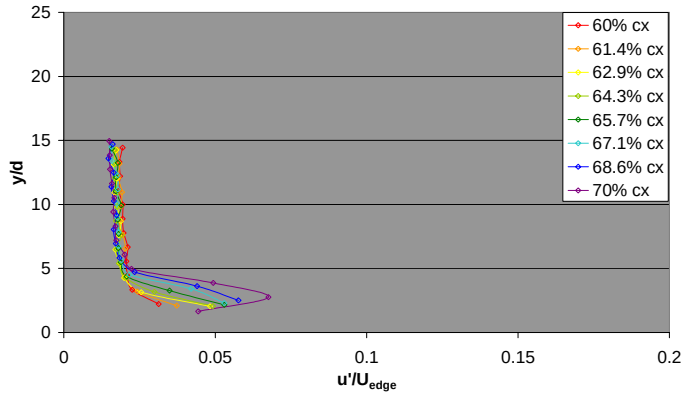


(b) 60% to 70% $c_x$

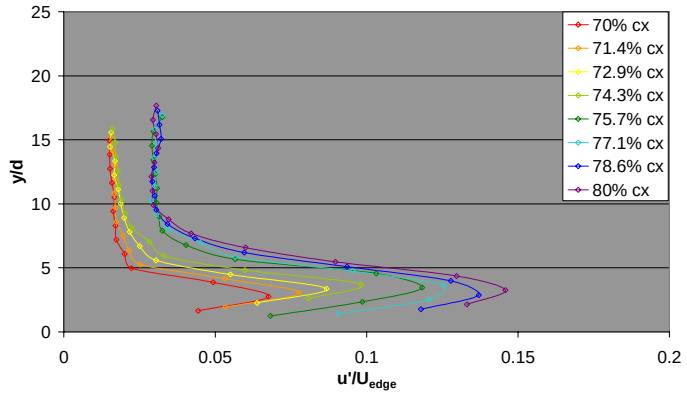


(c) 70% to 80% $c_x$

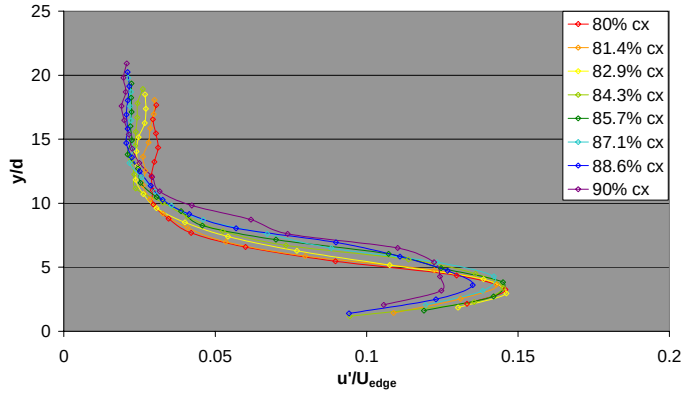


(d) 80% to 90% $c_x$

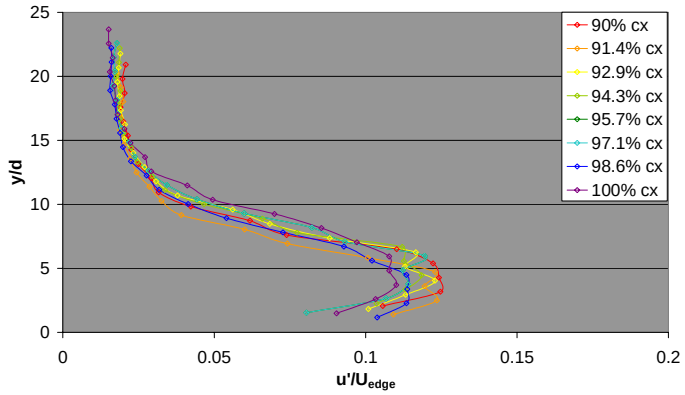


(e) 90% to 100% $c_x$

**Figure 5-8**. Plots of u'/$U_e$ for Re = 20,000 at chord positions between 50% and 100% $c_x$.

The values of u' were then squared and integrated in order to estimate turbulent kinetic energy. The integration was performed numerically using the trapezoid method. The limits of integration extended from the edge of the boundary layer to the blade surface. The result of this integration is shown in Figure 5-9. It is again recognized that this calculation does not necessarily provide an accurate value for the turbulent kinetic energy due to the low number of averaged images. Also, because the time between the images is relatively large, only the long wavelength disturbances in the energy spectrum are captured. Therefore, the usefulness of this calculation lies in the trend that is found rather than in the specific numerical values.

Figure 5-9 clearly shows the difference between the laminar and turbulent conditions of the flow. Initially the flow is laminar and the associated energy is very low. As the flow begins to transition, turbulent fluctuations develop and are accompanied by the drastic increase in turbulent kinetic energy seen between 70% and 80% $c_x$. Once the boundary layer reattaches, the flow remains turbulent for the remainder of the flow field.

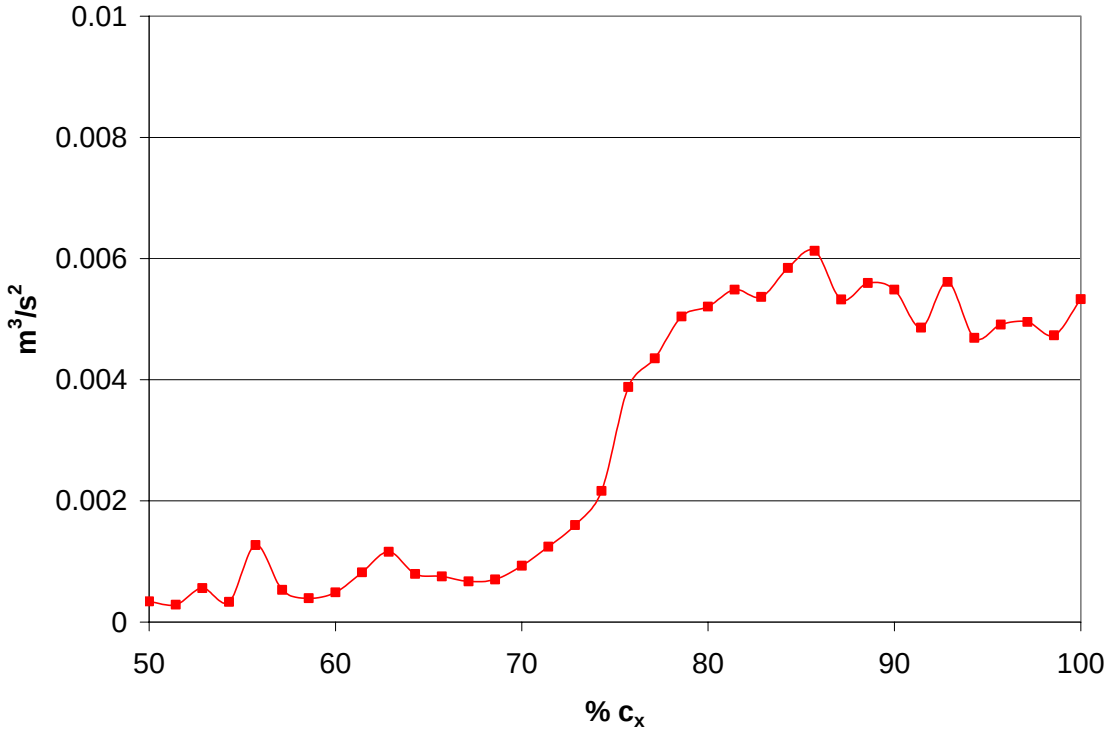


**Figure 5-9**. Turbulent kinetic energy at chord positions between 50% and 100% $c_x$.

## 5.2. Steady Injection

Once the uncontrolled flow had been analyzed (as described previously), a comparison between the uncontrolled and steady jet control at B = 2 could be made. Figure 5-10 displays the effect of steady VGJs on the separating boundary layer. The jets were operated at a blowing ratio of 2 and were injected at 50% $c_x$ with 30° pitch and 90° skew angles. Spanwise averaged contour plots analogous to those shown in Figure 5-1 are seen again for Re = 50,000 and 20,000. The flow control produced by the jets is clearly evident as the size and magnitude of the separated area is dramatically reduced. Though the PIV data indicate the possibility of a slight separation bubble remaining at

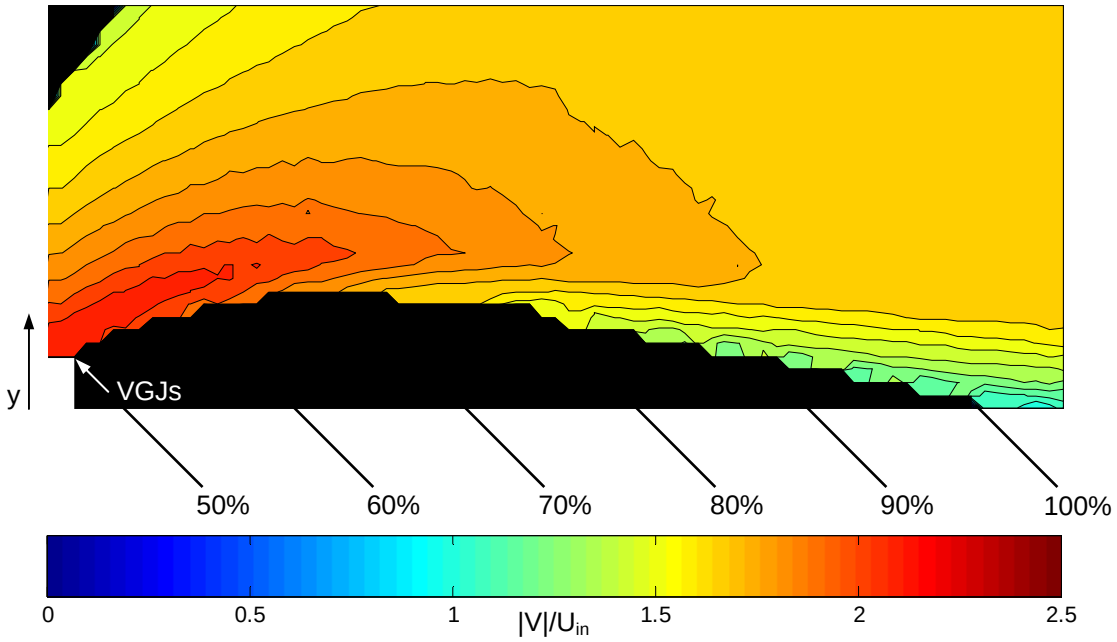


(a) Velocity magnitude contours for Re = 50000, B = 2.

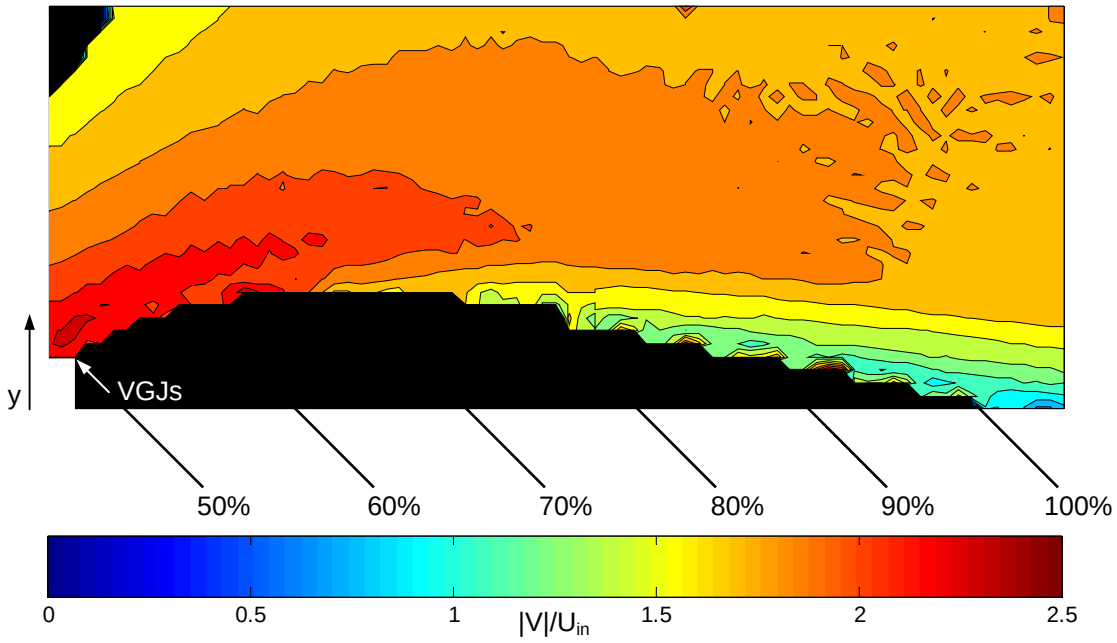


(b) Velocity magnitude contours for Re = 20000, B = 2.

**Figure 5-10**. Spanwise averaged contour plots of velocity magnitude normalized by cascade inlet velocity for B=2 at a) Re=50000 and b) Re=20000. A mask covering the blade is visible in the bottom of the plots. Data are presented looking up the span of the blade in the –z direction.

70% $c_x$, the $c_p$ data offer no evidence of separation. The absence of a significant separation bubble reduces the trailing edge boundary layer thickness and increases the peak velocity (peak $c_p$) through the passage.

The evolution of steady VGJ control over the blade surface can be seen in Figure 5-11, where contour plots similar to those shown in Figure 3-4 are shown. Again, the x- and y-components of velocity, with the out-of-plane vorticity are shown at varying chord positions between 50% and 70% $c_x$. The black mask at the bottom of each plot represents the position of the blade surface at each chord location. Because of the streamwise acceleration caused by the blades (a speed-up of a factor of 2), the velocity values were normalized by the constant cascade inlet velocity, instead of by the local freestream value used for the steady jets in the flat plate (zero pressure gradient) configuration.

The lobes of low velocity fluid shown in the top row of Figure 5-11 are evidence of the jet fluid. The penetration depth of the jet can be seen to be about 2.5 diameters from the blade surface, which is in agreement with Figure 3-4. However, the jet migrates significantly in the spanwise direction, to a position about 8 diameters away from the injection point, as compared to the spanwise migration of only 3 diameters seen on the flat plate (zero pressure gradient).

The v-component of velocity, showing the fluid motion out from and towards the blade surface (shown in the middle row of Figure 5-4) again indicates the creation of streamwise vorticity in the flow (bottom row of Figure 5-4). The primary vortex develops at the jet injection point and gradually migrates in the negative spanwise direction, while growing in diameter and decaying in strength. The vortex is no longer distinguishable after about 75% $c_x$.

As previously discussed, further evidence of streamwise vortex motion in the boundary layer includes the thickening of the boundary layer on the upwash side of the vortex, with a corresponding thinning on the opposite side. These phenomena signal that it is the freestream entrainment that is ultimately responsible for the elimination of the separation bubble in the steady jet case. From the data gathered from the flat plate, zero pressure gradient tests, it is likely that much of the boundary layer distortion occurs in the near-surface region where PIV data could not be collected. Because of the inability of the PIV system to collect data close to the curved blade surface, the thickening and thinning of the boundary layer around the vortex is not as noticeable in Figure 5-4. However, a closer inspection shows this familiar behavior at 60% $c_x$ (and less prominently at 64% $c_x$).

The results from the steady jet injection were then analyzed in the same manner which was described for the uncontrolled case. Figure 5-12 shows the $u/U_{in}$ profiles for B = 2. A comparison of the plots in Figure 5-12 to those shown in Figure 5-3 for the uncontrolled case shows the effectiveness of the flow control. The separated area is clearly reduced as the near-surface velocities remain high, and no evidence of flow reversal can be seen. Extrapolation of the velocity profile to the blade surface (Figure 5-13) yielded only positive $(u/U_{in})_{ext}$ values, indicating that separation never occurred.

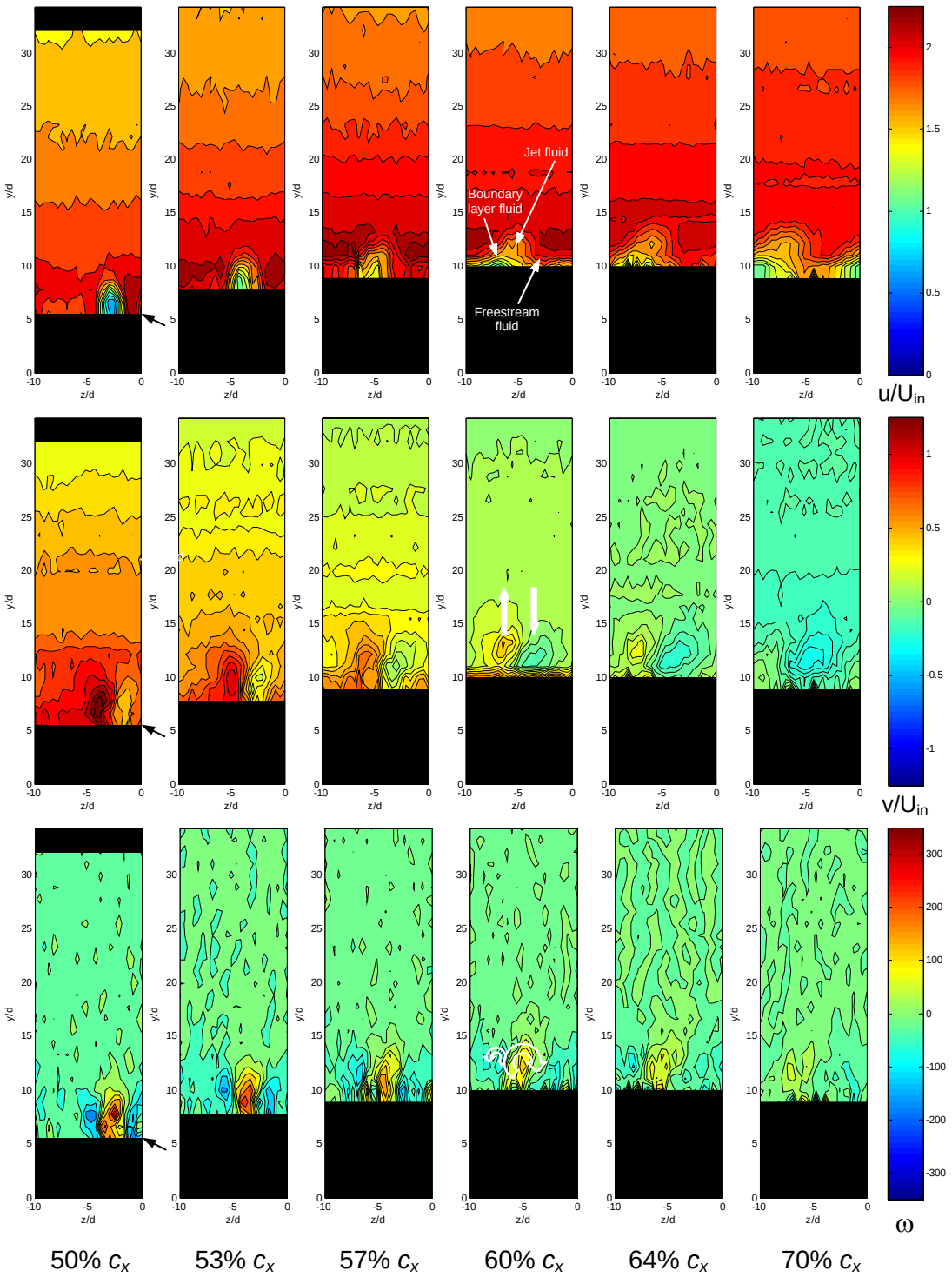


**Figure 5-11**. Contour maps of streamwise velocity (top row), wall normal velocity (middle row) and out-of-plane vorticity (bottom row) showing vortex development at streamwise positions between 50% and 70% $c_x$. Steady jet injection into three-blade cascade with B = 2. Velocities are normalized by the cascade inlet velocity. Looking in the positive x direction. Black arrows indicate jet injection points.

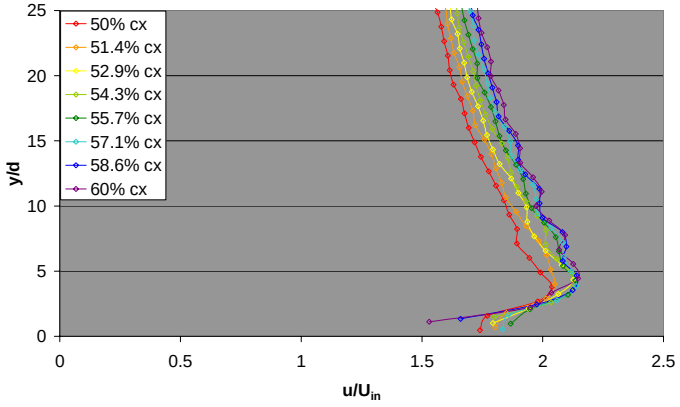


(a) 50% to 60% $c_x$

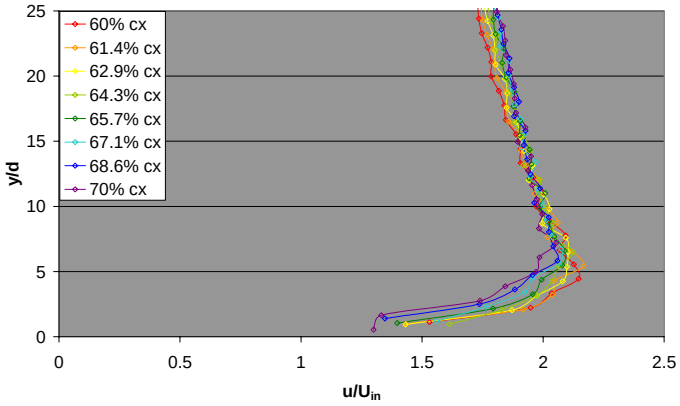


(b) 60% to 70% $c_x$

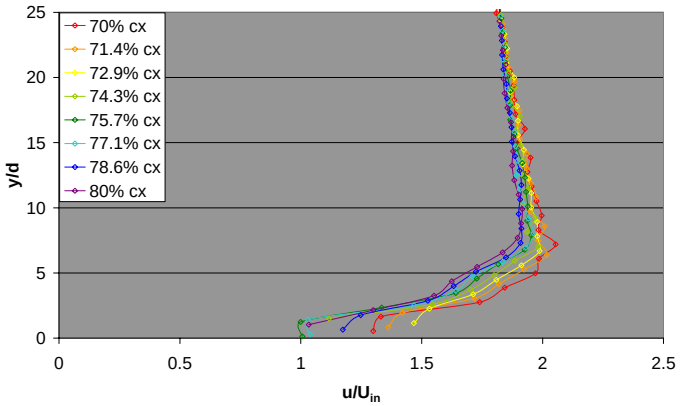


(c) 70% to 80% $c_x$

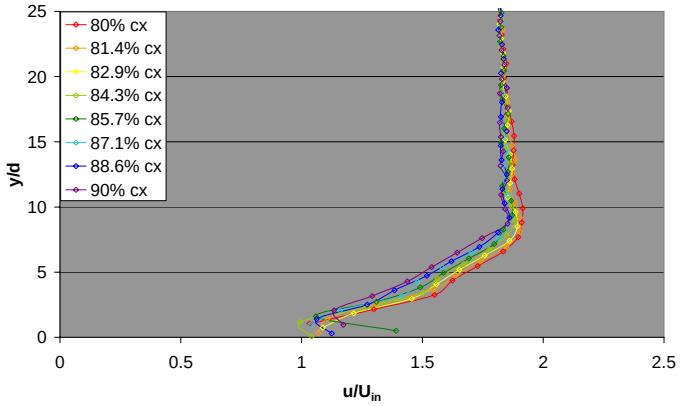


(d) 80% to 90% $c_x$

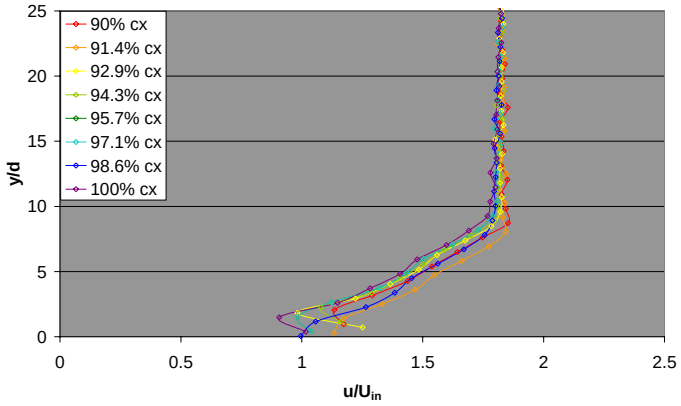


(e) 90% to 100% $c_x$

**Figure 5-12**. Plots of $u/U_{in}$ for B = 2 at chord positions between 50% and 100% $c_x$.

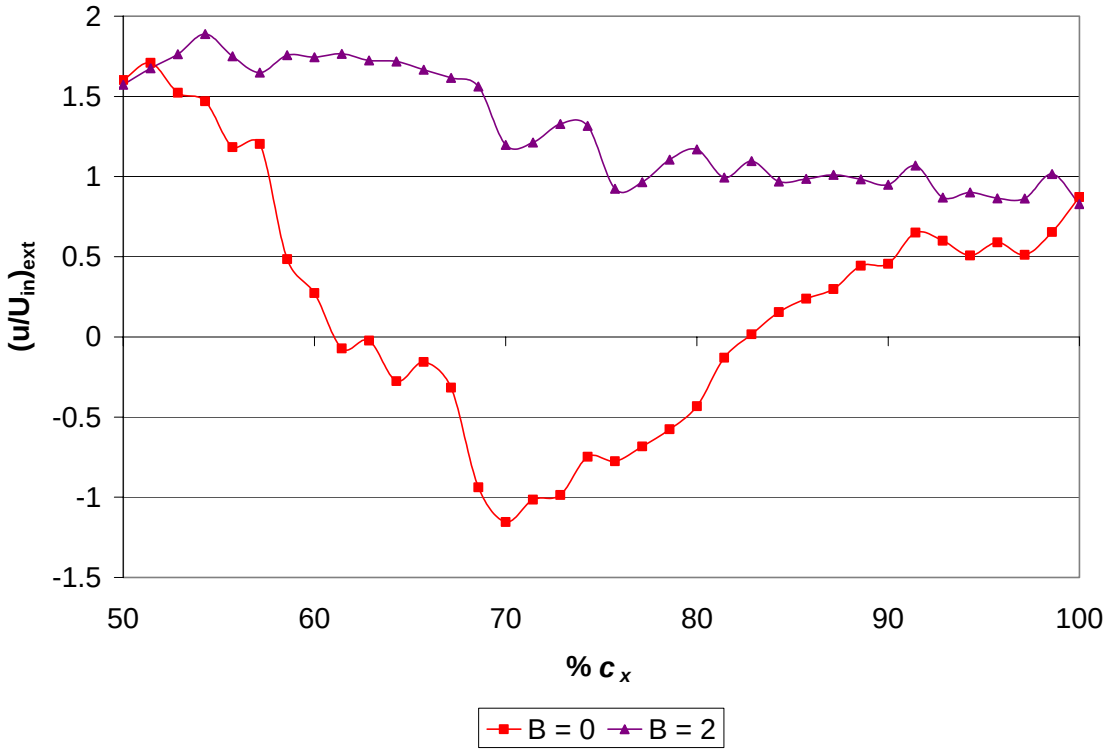


**Figure 5-13.** Values of $u/U_{in}$ extrapolated to the blade surface at chord positions between 50% and 100% $c_x$ for B = 0 and B = 2.

A comparison of the shape factor between the controlled and uncontrolled cases was also made. The shape factor was calculated at the same 36 chord positions as before, following the procedure previously described. The results of this calculation are plotted (with the data from Figure 5-7) in Figure 5-14.

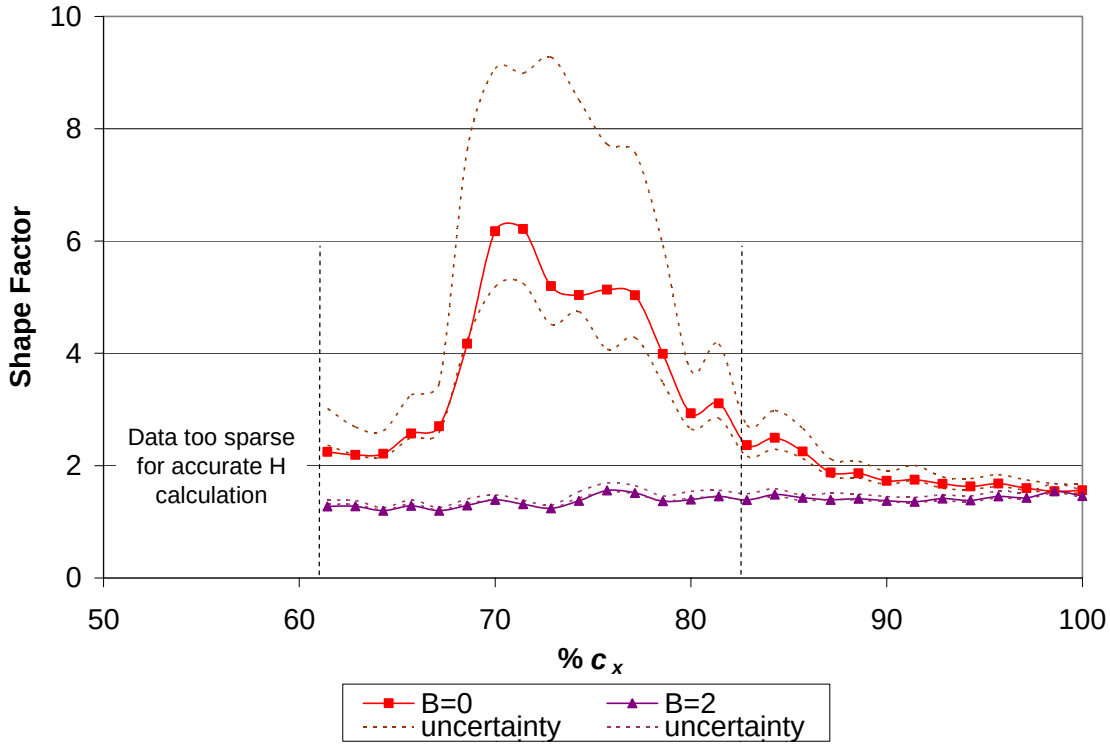


**Figure 5-14**. Shape factor for B = 0 and B = 2 for steady jet injection at chord positions from 50% to 100% $c_x$. The estimated separation bubble length determined from Figure 5-6 is noted by the dashed black lines.

It is clear from Figure 5-14 that steady jets at B = 2 effectively reduce the separation in the flow. The shape factor remains low and fairly constant through the entire separated zone, indicating that the separation bubble is removed. It is also important to note that the shape factor at 100% $c_x$ is essentially equal for the both the controlled and uncontrolled cases.

## 5.3. Pulsed Jet Injection

Further insights for future blade design with integrated VGJs were gained through the study of pulsed jet flow control. The results are best displayed in three-dimensional

surface plots of the flow field. Figure 5-15 shows the surface where the u-velocity component is 75% of the cascade inlet velocity. The jet injection is in the negative z-direction with the center of the hole located at z/d = 0. To aid in the visualization of the flow separation, the y-coordinate of the blade contour was subtracted from the velocity surface shown in Figure 5-15. Thus, the velocity surface elevations are relative to the local blade contour. This is different than the presentation in Figures 5-1, 2, 10, and 11 where the blade contour is covered by a black mask. The approximate chord location is indicated at the left of the figure. The plot is colored by the velocity surface height in the y-direction.

The uncontrolled case (B = 0) is shown first (Figure 5-15a), followed by the flow fields of the 8 individual phases of the pulsing cycle (Figures 5-15 b-i). Due to the flow acceleration in the blade passage (an acceleration of roughly twice the inlet velocity), the $0.75U_{in}$ velocity surface identifies a region that is in the lower 50% of the suction surface boundary layer in the PIV flow domain. Thus, locations where this surface is substantially removed from the wall indicate separated flow. Accordingly, Figure 5-15a provides support to the pressure measurements in Figure 2-6 and the estimates made in Figure 3-6, as the separation bubble is seen to stretch from about 65% to 90% $c_x$.

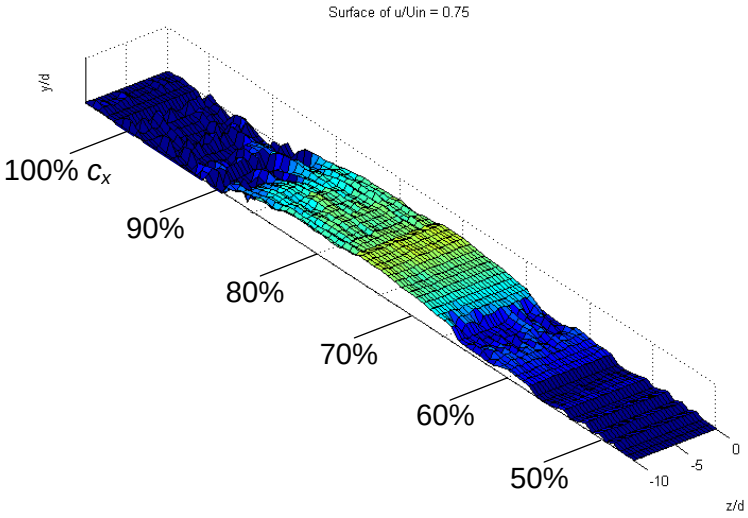


(a)
uncontrolled
B=0

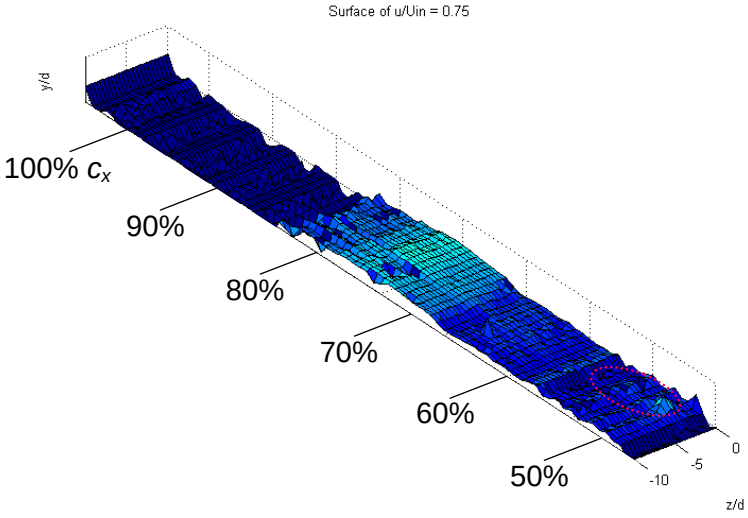


(b)
t/T=0.025
Phase 1
pulse start

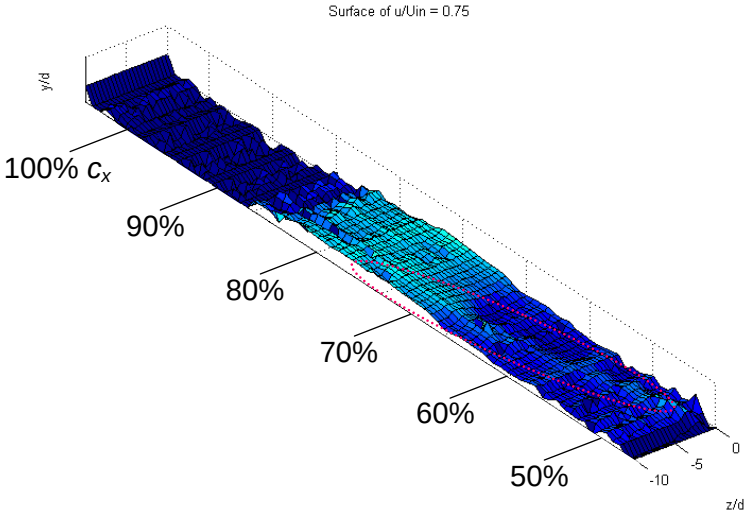


(c)
t/T=0.150
Phase 2
pulse on

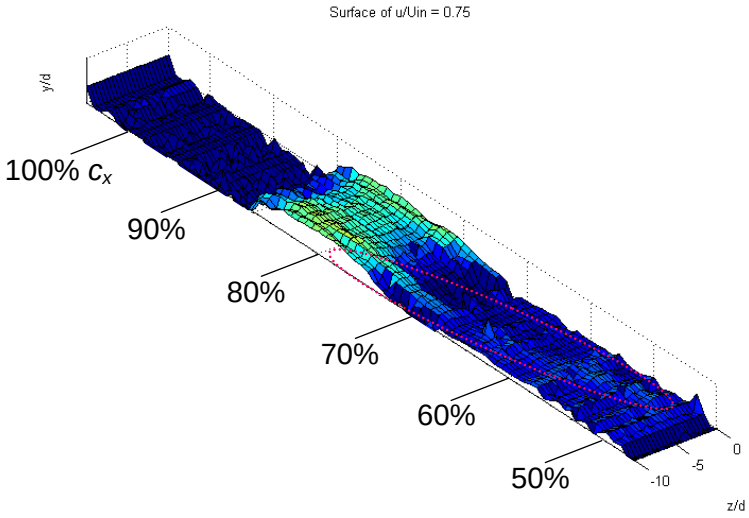


(d)
t/T=0.275
Phase 3
pulse end

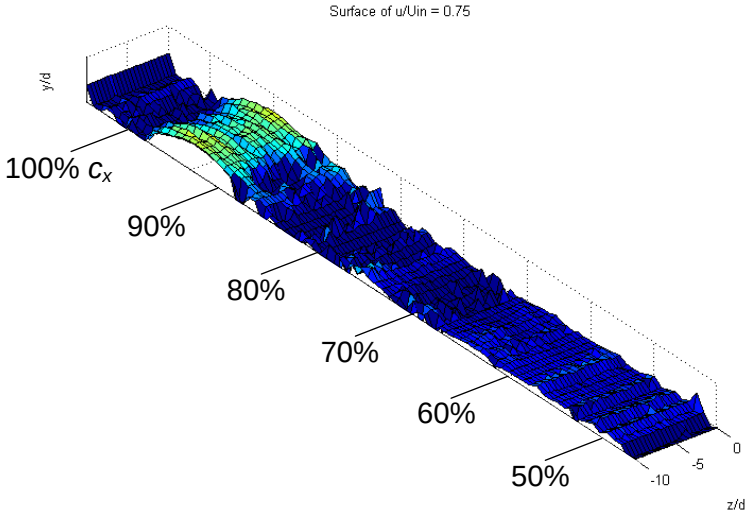


(e)
t/T=0.400
Phase 4
pulse off

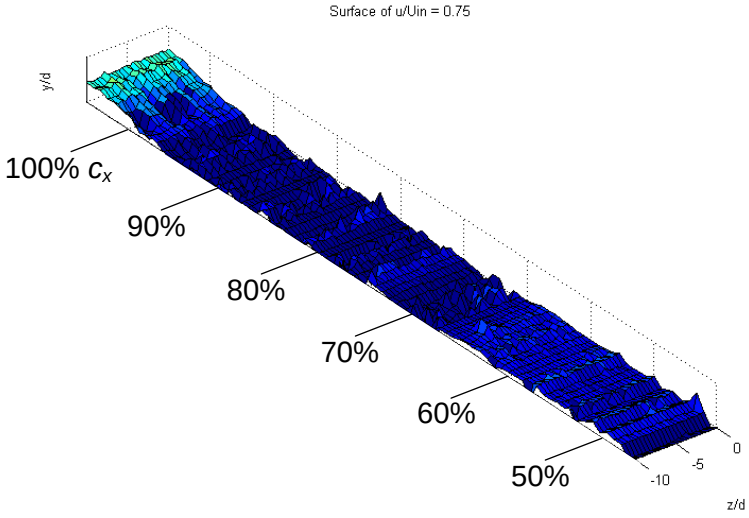


(f )
t/T=0.525
Phase 5
pulse off

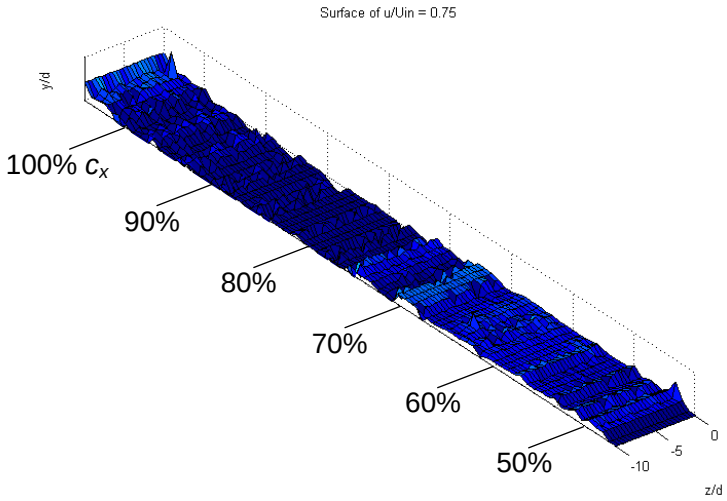


(g)
t/T=0.650
Phase 6
pulse off

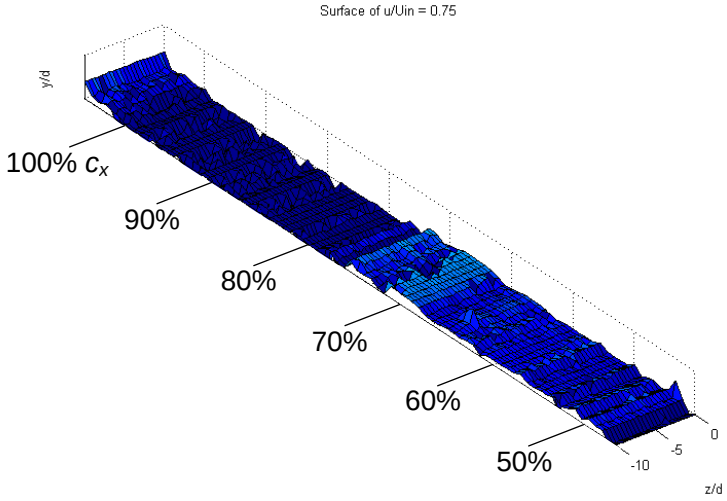


(h)
t/T=0.775
Phase 7
pulse off

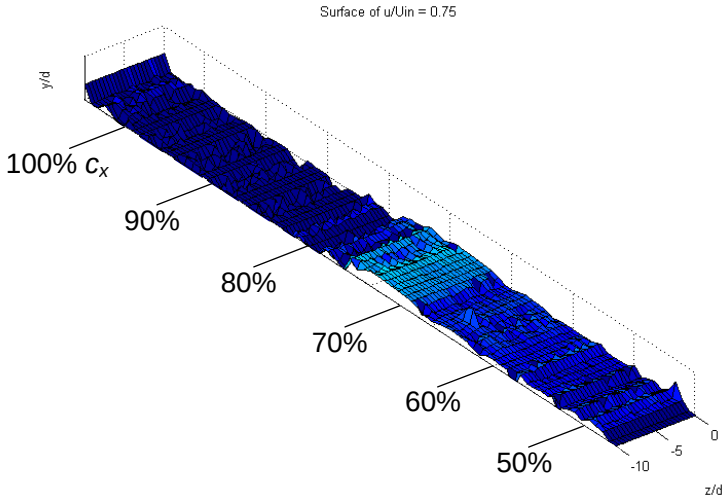


(i)
t/T=0.900
Phase 8
pulse off

**Figure 5-15**. 3-D surfaces of streamwise velocity where $u = 0.75U_{in}$ taken at 8 discrete points in the pulsing cycle. Pulsed, angled injection into 3-blade cascade at 5 Hz and 25% duty cycle with maximum B = 2. The approximate position of the jet fluid is marked by a pink oval.

The phase-locked surface plots in Figure 5-15 b-i provide significant new information regarding the unsteady interaction of the pulsed VGJ with the separation bubble on the L1M blade suction surface. First, the presence of the jet fluid is evident in the flow domain. During phase 1 (Figure 5-15b) when the jet is being turned on, the jet fluid is just visible as it enters the flow field (as indicated by the dotted pink line). This is evident in the small hump that develops just downstream of the jet exit. The amount of jet fluid in the flow domain has increased significantly by phase 2 (Figure 5-15c). The jet pulse is turned off just before phase 3 (Figure 5-15d), so the jet fluid is no longer visible entering the flow domain. The jet fluid continues to convect downstream but is obstructed from view by the moving separation bubble from 80% to 90% $c_x$. The slight depression in the velocity surface at z/d = -5 and between 70% and 75% $c_x$ is evidence of jet-induced vorticity. As seen previously, the injected jet creates a positive vortex that thins the boundary layer on the downwash side of the vortex (to the right of the jet fluid, looking downstream) through the entrainment of freestream fluid down to the wall. Also visible is the spanwise migration of the jet fluid. The jet migrates in the negative z direction to about z/d = -8 before exiting the flow domain. This is consistent with the jet migration noted in Figure 5-11 for steady injection at B = 2, but about 25% larger than that reported by Eldredge and Bons[7] for steady jet injection at B = 2 on the Pack B blade. Once the jet has been turned off, the remaining jet fluid travels downstream and disappears from the field of view for the remaining phases of the pulsing cycle.

The shape and behavior of the separation bubble seen in Figure 5-15 is also worthy of discussion. Although the disturbance of the jet and the ensuing vortical structures completely disappear upon entering the separated area, the effect of this

disturbance on the extent of separation is significant. During phase 2 (Figure 5-15c), when the jet fluid reaches 70% $c_x$, the separation bubble is drastically reduced, as seen by the reduction in the velocity surface elevation. Phases 3 and 4 (Figure 5-15 d-e) show the downstream movement of the separation bubble, with the leading edge of the bubble moving from 85% to nearly 100% $c_x$. At the same time, the trailing edge of the separation bubble moves from about 75% to 90% $c_x$, indicating that the trailing edge of the bubble actually moves faster than the leading edge. It is this behavior that creates a more arched separation bubble surface in Figure 5-15e. The flow becomes reattached after the separation bubble passes through the flow domain in phases 3-5 (Figure 5-15 d-f), a phenomenon that squeezes the bubble off the surface of the blade. When the bubble has left the domain (Figure 5-15g), the entire surface of the blade has become reattached. It is only during the last two phases of the pulsing cycle (Figures 5-15 h-i) that the separation zone begins to grow again.

Of particular interest during this entire process is that with the exception of the depression seen beside the jet fluid seen in phase 3 (Figure 5-15d), there is no evidence of a jet-induced distortion in the separation bubble. Instead, the phase-locked separation bubble motion appears to be a two-dimensional spanwise-uniform fluid event. This result coincides with the findings of Postl et. al[11,12], who predicted that flow control is achieved (on a Pack-B blade) by the development of two-dimensional spanwise waves, rather than through freestream entrainment caused by vortex generation. This wave-like behavior was not observed for the pulsed jets on a flat plate with an applied adverse pressure gradient (Figure 4-3). It is possible that the spanwise wave is a result of the

blade curvature, but further research will be necessary to determine the cause of the wave and whether it is a more general phenomenon.

The dimensionless forcing frequency, $F^+$ (defined as the ratio of the forcing frequency to the average freestream velocity divided by the surface distance from the jet injection point to the trailing edge), was also calculated. This parameter describes the relationship between the frequency of the jet pulse and the frequency of the disturbance caused by the jet. The $F^+$ value was found to be about 0.5, so the separation bubble does not return to its fully uncontrolled state before the next jet pulse is initiated. The relaxation time of the separation bubble is therefore longer than the 150ms interval between periods of jet injection. Thus it is likely that the frequency and duty cycle of the jet pulse could be reduced while still providing adequate separation control.

# 6. CONCLUSIONS

The effect of vortex generator jets in low Reynolds number flows was studied. A flat plate (zero pressure gradient), a flat plate with an applied pressure gradient and a three-blade cascade were employed as a basis for future LPT blade experiments.

The flat plate scenario was designed to give insight into the structure and movement of the vortical structures. Steady jets were injected normally and at an angle (30˚ pitch and 90˚ skew) to the freestream flow. The normal jet created a double vortex structure that grew in size while diminishing in strength as it traveled downstream. The vortices gradually migrated out from the wall, but maintained the same spanwise position. In contrast, the angled jet created a single vortex that migrated both up and out from the wall while remaining coherent for a longer distance than did the vortices generated by the normal jet. The vortices were observed to pull boundary layer fluid out from the wall and bring freestream fluid down close to the wall. This behavior was not as prominent when the jets were injected normally. These results show that the vortices produced by angled VGJs are structured in a way to more effectively promote freestream entrainment. Pulsed, angled jets were also applied to the flat plate flow. The results were comparable to the steady, angled jets. The lingering boundary layer effects caused by the streamwise vortices after the jet pulse had passed suggests that the flow control does not end immediately when the pulse is turned off.

The flat plate with an applied pressure gradient provided a separating boundary layer in which to test the effectiveness of pulsed VGJs. Normal and angled jets were again injected into the flow, and the reaction of the flow field was captured at eight discrete points in the pulsing cycle. The integrated loss coefficient was calculated to provide a quantitative basis for comparison. It was found that the cycle averaged loss coefficient for both normal and angled jets was nearly equivalent. The normal jets initiated a disturbance to control the separation earlier in the pulsing cycle, while the angled jets produced a disturbance later in the pulsing cycle, but that reacted more quickly to control the flow. The data also suggest that the development of the streamwise vortices is modified when the jets are injected into a separating boundary layer.

Once the basic flow physics of the VGJs was understood, the three-blade cascade configuration was employed to provide more realistic data and a better application to future LPT design. Both steady and pulsed jets injected at 30° pitch and 90° skew angles were introduced into a separating boundary layer induced by flow across an L1M blade. The steady jet injection was successful in reducing boundary layer separation through streamwise vortex formation and the accompanying freestream entrainment. With pulsed jets, however, reattachment of the boundary layer occurred rapidly as the separation bubble is pushed downstream as a two-dimensional, spanwise occurrence. After the bubble has passed through the flow domain and the boundary layer has been reduced to its minimum state, the separation bubble begins to redevelop. However, the boundary layer never reaches the uncontrolled, separated state because a new jet pulse is initiated before the separation bubble can fully return.

A more quantitative analysis of the boundary layer was performed by examining the streamwise velocity profiles and the turbulent fluctuations at varying chord positions for the uncontrolled case. This analysis was able to provide estimates of the positions along the blade surface of separation and reattachment, as well as the point where transition to turbulence begins. This provides a systematic method of comparing and analyzing the effectiveness of VGJ flow control.

## REFERENCES


[1] Sharma, O., 1998, "Impact of Reynolds Number on LP Turbine Performance," *Proceedings of 1997 Minnowbrook II Workshop on Boundary Layer Transition in Turbomachines*, NASA/CP-1998-206958.

[2] Lake, J. P., King, P. I., and Rivir, R. B., "Reduction of Separation Losses on a Turbine Blade with Low Reynolds Number," AIAA 99-0242.

[3] Volino, R. J., 2003, "Passive Flow Control on Low-Pressure Turbine Airfoils," ASME GT2003-38728.

[4] Johnston, J. P., "Pitched and Skewed Vortex Generator Jets for Control of Turbulent Boundary Layer Separation: A Review," *Proceedings of the 3rd ASME/JSME Joint Fluids Engineering Conference*, FEDSM99-6917.

[5] Sondergaard, R., Bons, J. P., and Rivir, R. B., 2002, "Control of Low-Pressure Turbine Separation Using Vortex Generator Jets," *AIAA Journal of Propulsion and Power*, Vol. 18, No. 4, pp. 889-895. Jul/Aug 2002.

[6] Khan, Z. U. and Johnston, J. P., 2000, "On Vortex Generating Jets," *International Journal of Heat and Fluid Flow*, Vol. 21, pp. 506-511.

[7] Eldredge, R. G. and Bons, J. P., 2004, "Active Control of a Separating Boundary Layer with Steady Vortex Generating Jets—Detailed Flow Measurements," presented at the AIAA Aerospace Sciences Meeting, Reno, Nevada, Jan. 5-8, 2004.

[8] Rixon, G. S. and Johari, H., 2003, "Development of a Steady Vortex Generator Jet in a Turbulent Boundary Layer." *ASME Journal of Fluids Engineering*, Vol. 125, pp. 1006-1015.

[9] Johari, H. and Rixon, G. S., 2003. "Effects of Pulsing on a Vortex Generator Jet." *AIAA Journal*, Vol. 41, No. 12, pp. 2309-2315.

[10] Bons, J. P., Sondergaard, R., and Rivir, R. B., 2001, "Turbine Separation Control Using Pulsed Vortex Generator Jets," *ASME Journal of Turbomachinery*, Vol, 123, pp. 198-206.

[11] Postl, D., Gross, A., and Fasel, H. F. "Numerical Investigation of Low-Pressure Turbine Blade Separation Control," AIAA 2003-0614.

[12] Postl, D., Gross, A., and Fasel, H. F. "Numerical Investigation of Active Flow Control for Low-Pressure Turbine Blade Separation," AIAA 2004-0750.

[13] Bons, J. P., Sondergaard, R., and Rivir, R. B., 2002, "The Fluid Dynamics of LPT Blade Separation Control Using Pulsed Jets," *ASME Journal of Turbomachinery*, Vol. 124, pp. 77-85.

[14] Volino, R. J., "Separation Control on Low-Pressure Turbine Airfoils Using Synthetic Vortex Generator Jets," *Proceedings of the ASME Turbo Expo 2003*, GT2003-38729.

[15] Reshotko, E., Saric, W. S., and Nagib, H. M., 1997, "Flow Quality Issues for Large Wind Tunnels," AIAA 97-0225.

[16] Volino, R. J. and Hultgren, L. S., "Measurements in Separated and Transitional Boundary Layers Under Low-Pressure Turbine Airfoil Conditions," *ASME Turbo Expo 2000*, 2000-GT-0260.

[17] Sondergaard, R., Bons, J. P., and Rivir, R. B., 2002, "Reducing Low-Pressure Turbine Stage Blade Count Using Vortex Generator Jet Separation Control," presented at the 2002 International Gas Turbine Institute (IGTI) Conference in Amsterdam, The Netherlands, GT-2002-30602.

[18] Youngren, H., 1991, "Analysis and Design of Transonic Cascades with Splitter Vanes," MS Thesis, Massachusetts Institute of Technology.

[19] Giles, M. and Drela, M., 1987, "A Two-Dimensional Transonic Aerodynamic Design Method," *AIAA Journal*, Vol. 25, pp. 1199-1206.

[20] McAuliffe, B. R. and Yaras, M. I., "Separation-Bubble-Transition Measurements on a Low-Re Airfoil Using Particle Image Velocimetry," *Proceedings of the ASME Turbo Expo 2005*, GT2005-68663.

# APPENDIX

This program imports raw data from DaVis, merges upstream and downstream files, calculates vorticity, and creates 2- and 3d plots. Also allows writing of spanwise averaged files and importing of text files for turbulence calculations.

Title: PIVplotjpb9b.m

```
clear all;
holediam=0.0023; %m

% Import data files
fprintf('Data filename format must be: prefixN.txt where N is an integer.\n');
fprintf('N values start at the top and go down in the tunnel.\n');
filepref=[];
filepref=input('Enter filename prefix for upstream window <csg>: ','s');
if isempty(filepref)
   filepref='csg';
end

fileprefd=input('Enter filename prefix for downstream window <csq>: ','s');
if isempty(fileprefd)
   fileprefd='csq';
end

zind=[];
zind=input('Enter number of z data files, N <24>: ');
if isempty(zind)
   zind=24;
end
zspace=[];
zspace=input('Enter distance between z elevations <1mm>: ');
if isempty(zspace)
   zspace=1;
end
zspace=zspace/1000; %convert from mm to meters

fprintf('It is assumed that the data files have a single line of text as a header.\n');
fprintf('This initial header is followed by an m row x 5 column matrix of data.\n');
mrow=[];
mrow=input('Enter m number of rows in data files <1377>: ');
if isempty(mrow)
   mrow=1377;
end

fprintf('\n\n...loading in data...\n\n');
for i=1:zind
   filid=fopen([filepref,num2str(i),'.txt'],'rt');
```

```
   str1=fscanf(filid,'%c',68);  %Strip the header consisting of 68 characters
   dat=fscanf(filid,'%g',[5,mrow]);     % Data file is read in backwards
   dat=rot90(dat);
   dat=flipud(dat);       % Flip matrix so it reads y rows by x columns

   filidd=fopen([fileprefd,num2str(i),'.txt'],'rt');
   str1d=fscanf(filidd,'%c',68);  %Strip the header consisting of 68 characters
   datd=fscanf(filidd,'%g',[5,mrow]); % Data file is read in backwards
   datd=rot90(datd);
   datd=flipud(datd);   % Flip matrix so it reads y rows by x columns

% The data files should all have the same x and y positions so read these in only once
         x and y distances are in mm, velocities are in m/s
   if i==1
      xcol=dat(:,1);
      ycol=dat(:,2);
      xind=max(find(ycol==ycol(1)));
      Xposraw=xcol(1:xind);
      yind=length(ycol)/xind;
      for j=1:yind
         yposraw(j)=ycol(1+(j-1)*xind);
      end
   end
   xposstart=Xposraw(1);
   for k=1:xind
      Xposraw(k)=Xposraw(k)-xposstart;
      Xpos=Xposraw/(1000*holediam);
   end
   Xposd=Xpos;
   for k=1:xind
      Xposd(k)=Xposd(k)+Xpos(xind);
   end
   xposadj=[Xpos;Xposd];
   xposadj(86,:)=[]; xposadj(85,:)=[]; xposadj(84,:)=[]; xposadj(83,:)=[];
xposadj(82,:)=[]; xposadj(81,:)=[];
   yposstart=yposraw(1);
   for j=1:yind
      Yposadj(j)=abs(yposraw(j)-yposstart);
      yposadj=Yposadj/(1000*holediam);
   end

% Now read in the velocity data
   for j=1:yind
      for k=1:xind
         uvel(i,j,k)=dat(xind-(k-1)+(j-1)*xind,3);
         vvel(i,j,k)=dat(xind-(k-1)+(j-1)*xind,4);
```

```
          wvel(i,j,k)=dat(xind-(k-1)+(j-1)*xind,5);
          uveld(i,j,k)=datd(xind-(k-1)+(j-1)*xind,3);
          vveld(i,j,k)=datd(xind-(k-1)+(j-1)*xind,4);
          wveld(i,j,k)=datd(xind-(k-1)+(j-1)*xind,5);
       end
    end
end

% Matrix manipulation to join up and downstream files
uvel(:,:,43)=[]; uvel(:,:,42)=[]; uvel(:,:,41)=[];  % delete last 3 x/d planes from us window
vvel(:,:,43)=[]; vvel(:,:,42)=[]; vvel(:,:,41)=[];
wvel(:,:,43)=[]; wvel(:,:,42)=[]; wvel(:,:,41)=[];
us=zeros(24,4,40);  %create matrix of 4 columns of zeros
uvel=[us,uvel]; vvel=[us,vvel]; wvel=[us,wvel]; % insert zeros to top of us window
uvel(:,36,:)=[]; uvel(:,35,:)=[]; uvel(:,34,:)=[]; uvel(:,33,:)=[]; % delete last 4 columns in
y/d from us window
vvel(:,36,:)=[]; vvel(:,35,:)=[]; vvel(:,34,:)=[]; vvel(:,33,:)=[];
wvel(:,36,:)=[]; wvel(:,35,:)=[]; wvel(:,34,:)=[]; wvel(:,33,:)=[];

uveld(:,:,1)=[]; uveld(:,:,1)=[]; uveld(:,:,1)=[];  %delete first 3 x/d planes from ds window
vveld(:,:,1)=[]; vveld(:,:,1)=[]; vveld(:,:,1)=[];
wveld(:,:,1)=[]; wveld(:,:,1)=[]; wveld(:,:,1)=[];

Uvel=cat(3,uvel,uveld);
Vvel=cat(3,vvel,vveld);
Wvel=cat(3,wvel,wveld);
Xind=80;

fprintf('Velocity data is loaded.\n');
fprintf('\nData deck consists of: \n');
fprintf('\t\t%d levels in z.\n',zind);
fprintf('\t\t%d points in y.\n',yind);
fprintf('\t\t%d points in x.\n',xind);

fprintf('y data extends from %6.4fy/d nearest the wall to %6.4fy/d in the
freestream.\n',min(yposadj),max(yposadj));
walloff=[];
walloff=input('Enter distance from nearest wall data point to wall <0mm>: ');
if isempty(walloff)
   walloff=0;
end
fprintf('Now y=0 at the wall and y increases away from the wall.\n\n');

fprintf('x data extends from %6.4fx/d downstream to %6.4fx/d
upstream.\n',min(xposadj),max(xposadj));
```

```
zdstart=[];
zdstart=input('Enter z/D coordinate of data block origin <-10>: ');
if isempty(zdstart)
   zdstart=-10;
end

fprintf('\nThe z levels are assumed to begin at z/d=0 and increase downward - opposite
the jet injection direction.\n\n');
for i=1:zind
   zposadj(i)=(i-1)*zspace/holediam;
end
zposadj=zposadj+zdstart;

uinf=abs(mean(mean(mean(uvel(:,ceil(yind/2):yind,:)))));
fprintf('Uinf calculated from the upper half of the datablock is %6.3f m/s.\n',uinf);
uinfd=[];
uinfd=input('Enter a new freestream velocity in m/s <accept default>: ');
if isempty(uinfd)==0
   uinf=uinfd;
end

% Normalize velocities by uinf
Uvel=Uvel/uinf;
Vvel=Vvel/uinf;
Wvel=Wvel/uinf;

% Positive x velocity is downstream, positive y velocity is away from wall, positive z
        velocity is down
Uvel=-Uvel; Vvel=-Vvel; Wvel=-Wvel;

% Create a 3D datablock of vorticities
fprintf('\nCalculating vorticity datablock...\n\n');
vortx3d=zeros(size(Uvel));
vorty3d=zeros(size(Uvel));
vortz3d=zeros(size(Uvel));

% For plotting of rms as % of Vmag, import spanwise averaged Vmag
ansx=[];
ansx=input('If data deck is rms, do you want to import a spanwise-avg Vmag/Uinf file?
<n>', 's');
if isempty(ansx)
   ansx='n';
end

% Calculate Vmag/Uinf
for i=1:zind
```

```
   for j=1:yind
      for k=1:Xind
         if ansx=='n'
            Vmag(i,j,k)=sqrt(Uvel(i,j,k)^2+Vvel(i,j,k)^2+Wvel(i,j,k)^2);
         else
            Vmag(i,j,k)=sqrt(Uvel(i,j,k)^2+Vvel(i,j,k)^2);
         end
      end
   end
end

if ansx=='y'
   Vmagfile=input('Enter the filename prefix of the Vmag data: ','s');
   Vmagnorm=dlmread([Vmagfile,'.txt'],'\t');
   for k=1:zind
      Vmag(k,:,:)=100*reshape(Vmag(k,:,:),yind,Xind)./Vmagnorm;          % Since
         Vmagnorm is Vmag/Uin and the rms data is currently stored in Vmag - this is Tu
   end
end

% For a 1st order approximation of the derivative
xsum=0.0;
for i=1:xind-1
   xsum=xsum+abs(Xposraw(i)-Xposraw(i+1));
end
xspace=xsum/(xind-1);

ysum=0.0;
for i=1:yind-1
   ysum=ysum+abs(yposraw(i)-yposraw(i+1));
end
yspace=ysum/(yind-1);
for i=1:zind
   zlo=i-1;
   zhi=i+1;
   dz=2*zspace;
   if i==1
      zlo=i;
      dz=zspace;
   elseif i==zind
      zhi=zind;
      dz=zspace;
   end
   for j=1:yind
      ylo=j-1;
      yhi=j+1;
```

```
      dy=2*yspace;
      if j==1
         ylo=j;
         dy=yspace;
      elseif j==yind
         yhi=yind;
         dy=yspace;
      end
      for k=1:Xind
         xlo=k-1;
         xhi=k+1;
         dx=2*xspace;
         if k==1
            xlo=k;
            dx=xspace;
         elseif k==Xind
            xhi=Xind;
            dx=xspace;
         end
         dwdy(i,j,k)=(Wvel(i,yhi,k)-Wvel(i,ylo,k))/dy;
         dvdz(i,j,k)=(Vvel(zhi,j,k)-Vvel(zlo,j,k))/dz;
         dudz(i,j,k)=(Uvel(zhi,j,k)-Uvel(zlo,j,k))/dz;
         dwdx(i,j,k)=(Wvel(i,j,xhi)-Wvel(i,j,xlo))/dx;
         dvdx(i,j,k)=(Vvel(i,j,xhi)-Vvel(i,j,xlo))/dx;
         dudy(i,j,k)=(Uvel(i,yhi,k)-Uvel(i,ylo,k))/dy;
         dvdy(i,j,k)=(Vvel(i,yhi,k)-Vvel(i,ylo,k))/dy;
         dwdz(i,j,k)=(Wvel(zhi,j,k)-Wvel(zlo,j,k))/dz;
         dudx(i,j,k)=(Uvel(i,j,xhi)-Uvel(i,j,xlo))/dx;
         dwdz(i,j,k)=(Wvel(zhi,j,k)-Wvel(zlo,j,k))/dz;
         dudx(i,j,k)=(Uvel(i,j,xhi)-Uvel(i,j,xlo))/dx;
         dvdy(i,j,k)=(Vvel(i,yhi,k)-Vvel(i,ylo,k))/dy;
         % vorticity
         vortx3d(i,j,k)=dwdy(i,j,k)-dvdz(i,j,k);
         vorty3d(i,j,k)=dudz(i,j,k)-dwdx(i,j,k);
         vortz3d(i,j,k)=dvdx(i,j,k)-dudy(i,j,k);
      end
   end
end

% With the masked data from the cascade, any cell that is in the masked portion of the
      camera field of view is assigned a velocity of 0.
% To avoid the skewing of the contour maps in Matlab, these masked regions are set to
      equal the value at the mask border.
topmask=(yind+1)*ones(Xind,1);
botmask=zeros(Xind,1);
```

```
% Since the mask is identical in all x-y camera frames, it only need be computed from 1 z
level.
for i=1:Xind
   if Uvel(1,1,i)==0
      zflag=0;
   else
      zflag=1;
   end
   for j=2:yind
      if Uvel(1,j,i)==0 & zflag==0
         zflag=0;
      elseif Uvel(1,j,i)==0 & zflag~=0
         topmask(i)=j;
         zflag=0;
      elseif Uvel(1,j,i)~=0 & zflag==0
         botmask(i)=j-1;
         zflag=1;
      else
         zflag=1;
      end
   end
end

% Botmask and Topmask now contain the bounding coordinates of the lower and upper
      masks respectively.
% Now proceed to fill this region of the velocity cube with the edge data.
for i=1:zind
   for k=1:Xind
      if topmask(k)~=yind+1
         Uvel(i,topmask(k):yind,k)=Uvel(i,topmask(k)-1,k)*ones(yind-topmask(k)+1,1);
         Vvel(i,topmask(k):yind,k)=Vvel(i,topmask(k)-1,k)*ones(yind-topmask(k)+1,1);
         Wvel(i,topmask(k):yind,k)=Wvel(i,topmask(k)-1,k)*ones(yind-topmask(k)+1,1);
      end
      if botmask(k)~=0
         Uvel(i,1:botmask(k),k)=Uvel(i,botmask(k)+1,k)*ones(botmask(k),1);
         Vvel(i,1:botmask(k),k)=Vvel(i,botmask(k)+1,k)*ones(botmask(k),1);
         Wvel(i,1:botmask(k),k)=Wvel(i,botmask(k)+1,k)*ones(botmask(k),1);
      end
   end
end

% Now compute the y values of the mask lines in x-y that will used to plot the mask later
topline=[];
botline=[];
for i=1:Xind
   topline(i)=yposadj(topmask(i)-1);
```

```
   botline(i)=yposadj(botmask(i)+1);
end

% The masked regions can be plotted as filled polygons in the x-y plane if the vertices of
the polygon are determined
topfillxy=[];
botfillxy=[];
jflag=1;
kflag=1;
for i=1:Xind
   if topmask(i)~=yind+1
      if jflag==1
         topfillxy(1,1)=xposadj(i);
         topfillxy(1,2)=yposadj(yind);
         j=2;
         jflag=0;
      end
      topfillxy(j,1)=xposadj(i);
      topfillxy(j,2)=yposadj(topmask(i)-1);
      j=j+1;
   end
   if botmask(i)~=0
      if kflag==1
         botfillxy(1,1)=xposadj(i);
         botfillxy(1,2)=yposadj(1);
         k=2;
         kflag=0;
      end
      botfillxy(k,1)=xposadj(i);
      botfillxy(k,2)=yposadj(botmask(i)+1);
      k=k+1;
   end
end
if jflag~=1
   topfillxy(j,:)=[topfillxy(j-1,1) yposadj(yind)];
end
if kflag~=1
   botfillxy(k,:)=[botfillxy(k-1,1) yposadj(1)];
end

% Plotting
ansa='y';
figind=2;
arrscale=2;
while ansa=='y'
   ansg=[];
```

```
   ansg=input('Do you want a 2 or 3 D plot? <2> ');
   if isempty(ansg)
      ansg=2;
   end
% 2D plots
   if ansg==2
      plane=[];
      plane=input('Select a plane for plotting 1=x-z, 2=x-y, 3=y-z <2>: ');
      if isempty(plane)
         plane=2;
      end
      % for y-z plots
      if plane==3
         xindplt=input('Enter a x/d position to be plotted <25>: ');
         if isempty(xindplt)
            xindplt=25;
         end
         % Create rectangular masks for the y-z view
         topfillyz=[];
         topfillyz(1,:)=[zposadj(1) yposadj(yind)];
         topfillyz(2,:)=[zposadj(1) yposadj(topmask(xindplt)-1)];
         topfillyz(3,:)=[zposadj(zind) yposadj(topmask(xindplt)-1)];
         topfillyz(4,:)=[zposadj(zind) yposadj(yind)];

         botfillyz=[];
         botfillyz(1,:)=[zposadj(1) yposadj(1)];
         botfillyz(2,:)=[zposadj(1) yposadj(botmask(xindplt)+1)];
         botfillyz(3,:)=[zposadj(zind) yposadj(botmask(xindplt)+1)];
         botfillyz(4,:)=[zposadj(zind) yposadj(1)];

         figure(figind);
         Uplot=reshape(Uvel(:,:,xindplt),zind,yind);
         Uplot=flipud(rot90(Uplot));
         contourf(zposadj,yposadj,Uplot,10)
         axis equal;
         caxis([0 2.25]);
         colorbar;
         xlim([min(zposadj) max(zposadj)]);
         ylim([min(yposadj) max(yposadj)]);
         xlabel('z/d');
         ylabel('y/d');
         title(['u/Uinf contour at x/d = ',num2str(xposadj(xindplt)),' Looking in positive x
direction.']);
         hold on;
         fill(topfillyz(:,1),topfillyz(:,2),'k');
         fill(botfillyz(:,1),botfillyz(:,2),'k');
```

```
        hold off;
        figind=figind+1;

        figure(figind)
        Vplot=reshape(Vvel(:,:,xindplt),zind,yind);
        Vplot=flipud(rot90(Vplot));
        contourf(zposadj,yposadj,Vplot,10)
        axis equal;
        caxis([-1.25 1.25]);
        colorbar;
        xlim([min(zposadj) max(zposadj)]);
        ylim([min(yposadj) max(yposadj)]);
        xlabel('z/d');
        ylabel('y/d');
        title(['v/Uinf contour at x/d = ',num2str(xposadj(xindplt)),' Looking in positive x
direction.']);
        hold on;
        fill(topfillyz(:,1),topfillyz(:,2),'k');
        fill(botfillyz(:,1),botfillyz(:,2),'k');
        hold off;
        figind=figind+1;

        figure(figind)
        Wplot=reshape(Wvel(:,:,xindplt),zind,yind);
        Wplot=flipud(rot90(Wplot));
        contourf(zposadj,yposadj,Wplot,10)
        axis equal;
        caxis([-1.5 1]);
        colorbar;
        xlim([min(zposadj) max(zposadj)]);
        ylim([min(yposadj) max(yposadj)]);
        xlabel('z/d');
        ylabel('y/d');
        title(['w/Uinf contour at x/d = ',num2str(xposadj(xindplt)),' Looking in positive x
direction.']);
        hold on;
        fill(topfillyz(:,1),topfillyz(:,2),'k');
        fill(botfillyz(:,1),botfillyz(:,2),'k');
        hold off;
        figind=figind+1;

%           Plot x-component of vorticity
        figure(figind);
        vortx=[];
        vortx=reshape(vortx3d(:,:,xindplt),zind,yind);
        vortx=flipud(rot90(vortx));
```

```
        contourf(zposadj,yposadj,vortx,10);
        caxis([-350 350]);
        colorbar;
        axis equal;
        xlim([min(zposadj) max(zposadj)]);
        ylim([0 max(yposadj)]);
        title(['X-vorticity contour at x/d = ',num2str(xposadj(xindplt)),' Looking in
positive x direction.']);
        xlabel('z/d');
        ylabel('y/d');
        hold on;
        fill(topfillyz(:,1),topfillyz(:,2),'k');
        fill(botfillyz(:,1),botfillyz(:,2),'k');
        hold off;
        figind=figind+1;

    % for x-y plots
    elseif plane==2
        zplot=[];
        fprintf('x-y planes may be plotted from z/d = %6.3f to
%6.3f.\n',zposadj(1),zposadj(zind));
        zplot=input('Enter a z/d location between these bounds <0>: ');
        if isempty(zplot)
           zplot=0;
        end
        [dum,zindplt]=min(abs(zposadj-zplot));

        ansb=[];
        ansb=input('Plot with new figures or overwrite <new>? ','s');
        if isempty(ansb)
           ansb='n';
        end
        if ansb~='n'
           figind=2;
        end

        figure(figind);
        Uavg=reshape(mean(Uvel),yind,Xind);
        contourf(xposadj,yposadj,Uavg,15);
        axis equal;
        caxis([0 2.25]);
        colorbar('horiz');
        xlim([min(xposadj) max(xposadj)]);
        ylim([0 max(yposadj)]);
        title(['Spanwise averaged urms/Uinf contour']);
        xlabel('x/d');
```

```
        ylabel('y/d');
        hold on;
        if jflag~=1
           fill(topfillxy(:,1),topfillxy(:,2),'k');
        end
        if kflag~=1
           fill(botfillxy(:,1),botfillxy(:,2),'k');
        end
        hold off;
        figind=figind+1;

        figure(figind);
        Vavg=reshape(mean(Vvel),yind,Xind);
        contourf(xposadj,yposadj,Vavg,15);
        axis equal;
        caxis([0 2.25]);
        colorbar('horiz');
        xlim([min(xposadj) max(xposadj)]);
        ylim([0 max(yposadj)]);
        title(['Spanwise averaged vrms/Uinf contour']);
        xlabel('x/d');
        ylabel('y/d');
        hold on;
        if jflag~=1
           fill(topfillxy(:,1),topfillxy(:,2),'k');
        end
        if kflag~=1
           fill(botfillxy(:,1),botfillxy(:,2),'k');
        end
        hold off;
        figind=figind+1;

        figure(figind);
        clf;
        Uplot=reshape(Uvel(zindplt,:,:),yind,Xind);
        contourf(xposadj,yposadj,Uplot,10);
        caxis([-0.5 2.5]);
        colorbar('horiz');
        axis equal;
        xlim([min(xposadj) max(xposadj)]);
        ylim([0 max(yposadj)]);
        title(['urms/Uinf contour at z/d = ',num2str(zposadj(zindplt)),' Looking in negative
z direction.']);
        xlabel('x/d');
        ylabel('y/d');
        hold on;
```

```
        if jflag~=1
           fill(topfillxy(:,1),topfillxy(:,2),'k');
        end
        if kflag~=1
           fill(botfillxy(:,1),botfillxy(:,2),'k');
        end
        hold off;
        figind=figind+1;

        figure(figind);
        clf;
        Vplot=reshape(Vvel(zindplt,:,:),yind,Xind);
        contourf(xposadj,yposadj,Vplot,10);
        caxis([0 0.5]);
        colorbar;
        axis equal;
        xlim([min(xposadj) max(xposadj)]);
        ylim([0 max(yposadj)]);
        title(['v/Uinf contour at z/d = ',num2str(zposadj(zindplt)),' Looking in negative z
direction.']);
        xlabel('x/d');
        ylabel('y/d');
        hold on;
        if jflag~=1
           fill(topfillxy(:,1),topfillxy(:,2),'k');
        end
        if kflag~=1
           fill(botfillxy(:,1),botfillxy(:,2),'k');
        end
        hold off;
        figind=figind+1;

         figure(figind);
         clf;
         Wplot=reshape(Wvel(zindplt,:,:),yind,Xind);
         contourf(xposadj,yposadj,Wplot,10);
         caxis([-2.2 -0.2]);
         colorbar;
         axis equal;
         xlim([min(xposadj) max(xposadj)]);
         ylim([0 max(yposadj)]);
         title(['w/Uinf contour at z/d = ',num2str(zposadj(zindplt)),' Looking in negative z
direction.']);
         xlabel('x/d');
         ylabel('y/d');
         hold on;
```

```
        if jflag~=1
           fill(topfillxy(:,1),topfillxy(:,2),'k');
        end
        if kflag~=1
           fill(botfillxy(:,1),botfillxy(:,2),'k');
        end
        hold off;
        figind=figind+1;

   % Plot z-component of vorticity
        figure(figind);
        clf;
        vortz=reshape(vortz3d(zindplt,:,:),yind,Xind);
        contourf(xposadj,yposadj,vortz,10);
        caxis([-0.6 0.6]);
        colorbar('horiz');
        axis equal;
        xlim([min(xposadj) max(xposadj)]);
        ylim([0 max(yposadj)]);
        title(['Z-vorticity contour at z/d = ',num2str(zposadj(zindplt)),' Looking in
negative z direction.']);
        xlabel('x/d');
        ylabel('y/d');
        hold on;
        quiver(xposadj,yposadj,Uplot,Vplot,arrscale,'k');
        if jflag~=1
           fill(topfillxy(:,1),topfillxy(:,2),'k');
        end
        if kflag~=1
           fill(botfillxy(:,1),botfillxy(:,2),'k');
        end
        hold off;
        figind=figind+1;

%           Plot spanwise average of z component of vorticity
        figure(figind);
        clf;
        vortz=reshape(mean(vortz3d),yind,Xind);
        contourf(xposadj,yposadj,vortz,15);
        caxis([-0.6 0.6]);
        colorbar('horiz');
        axis equal;
        xlim([min(xposadj) max(xposadj)]);
        ylim([0 max(yposadj)]);
        title(['Spanwise average of Z-vorticity contour']);
        xlabel('x/d');
```

```
        ylabel('y/d');
        hold on;
        if jflag~=1
           fill(topfillxy(:,1),topfillxy(:,2),'k');
        end
        if kflag~=1
           fill(botfillxy(:,1),botfillxy(:,2),'k');
        end
        hold off;
        figind=figind+1;

    % Plot x-component of vorticity
         figure(figind);
         clf;
         vortx=reshape(vortx3d(zindplt,:,:),yind,Xind);
         contourf(xposadj,yposadj,vortx,10);
         caxis([-400 300]);
         colorbar;
         axis equal;
         xlim([min(xposadj) max(xposadj)]);
         ylim([0 max(yposadj)]);
         title(['X-vorticity contour at z/d = ',num2str(zposadj(zindplt)),' Looking in
negative z direction.']);
         xlabel('x/d');
         ylabel('y/d');
         hold on;
         if jflag~=1
            fill(topfillxy(:,1),topfillxy(:,2),'k');
         end
         if kflag~=1
            fill(botfillxy(:,1),botfillxy(:,2),'k');
         end
         hold off;
         figind=figind+1;

%           Plot the spanwise averaged velocity magnitude in m/s
        figure(figind);
        clf;
        Vmagplot=reshape(mean(Vmag),yind,Xind);
        contourf(xposadj,yposadj,Vmagplot,15);
        caxis([0 160]);
        colorbar('horiz');
        axis equal;
        xlim([min(xposadj) max(xposadj)]);
        ylim([0 max(yposadj)]);
        title(['Spanwise averaged rms velocity magnitude divided by Uinf']);
```

```
        xlabel('x/d');
        ylabel('y/d');
        hold on;
        if jflag~=1
           fill(topfillxy(:,1),topfillxy(:,2),'k');
        end
        if kflag~=1
           fill(botfillxy(:,1),botfillxy(:,2),'k');
        end
        hold off;
        figind=figind+1;

%           Plot the rms velocity magnitude in m/s
        figure(figind);
        clf;
        Vmagplot=reshape(Vmag(zindplt,:,:),yind,Xind);
        contourf(xposadj,yposadj,Vmagplot,15);
        caxis([0 160]);
        colorbar('horiz');
        axis equal;
        xlim([min(xposadj) max(xposadj)]);
        ylim([0 max(yposadj)]);
         title(['Spanwise averaged velocity magnitude divided by Uinf - Looking in
negative z direction.']);
        xlabel('x/d');
        ylabel('y/d');
        hold on;
        if jflag~=1
           fill(topfillxy(:,1),topfillxy(:,2),'k');
        end
        if kflag~=1
           fill(botfillxy(:,1),botfillxy(:,2),'k');
        end
        hold off;
        figind=figind+1;

    % for x-z plots
    else
       yplot=[];
       fprintf('x-z planes may be plotted from y/d = %6.3f to
%6.3f.\n',yposadj(1),yposadj(yind));
       yplot=input('Enter a y/d location between these bounds <1.5>: ');
       if isempty(yplot)
          yplot=1.5;
       end
       [dum,yindplt]=min(abs(yposadj-yplot));
```

```
ansb=[];
ansb=input('Plot with new figures or overwrite <new>? ','s');
if isempty(ansb)
   ansb='n';
end
if ansb~='n'
   figind=2;
end

figure(figind);
Uplot=reshape(Uvel(:,yindplt,:),zind,Xind);
contourf(xposadj,zposadj,Uplot,10);
 caxis([0.6 1.2]);
colorbar;
axis equal;
xlim([min(xposadj) max(xposadj)]);
ylim([min(zposadj) max(zposadj)]);
title(['u/Uinf contour at y/d = ',num2str(yposadj(yindplt)),' Looking in positive y
direction.']);
xlabel('x/d');
ylabel('z/d');
figind=figind+1;

figure(figind);
Vplot=reshape(Vvel(:,yindplt,:),zind,Xind);
contourf(xposadj,zposadj,Vplot,10);
 caxis([-0.1 0.3]);
colorbar;
axis equal;
xlim([min(xposadj) max(xposadj)]);
ylim([min(zposadj) max(zposadj)]);
title(['v/Uinf contour at y/d = ',num2str(yposadj(yindplt)),' Looking in positive y
direction.']);
xlabel('x/d');
ylabel('z/d');
figind=figind+1;

figure(figind);
Wplot=reshape(Wvel(:,yindplt,:),zind,Xind);
contourf(xposadj,zposadj,Wplot,10);
 caxis([-0.4 0.3]);
colorbar;
axis equal;
xlim([min(xposadj) max(xposadj)]);
ylim([min(zposadj) max(zposadj)]);
```

```
        title(['w/Uinf contour at y/d = ',num2str(yposadj(yindplt)),' Looking in positive y
direction.']);
        xlabel('x/d');
        ylabel('z/d');
        figind=figind+1;

    % Plot y-component of vorticity
        figure(figind);
        vorty=reshape(vorty3d(:,yindplt,:),zind,Xind);
        contourf(xposadj,zposadj,vorty,10);
         caxis([-800 800]);
        colorbar;
        axis equal;
        xlim([min(xposadj) max(xposadj)]);
        ylim([min(zposadj) max(zposadj)]);
        title(['Y-vorticity contour at y/d = ',num2str(yposadj(yindplt)),' Looking in
positive y direction.']);
        xlabel('x/d');
        ylabel('z/d');
        hold on;
        quiver(xposadj,zposadj,Uplot,Wplot,arrscale,'k');
        hold off;
        figind=figind+1;

    % Plot z-component of vorticity
        figure(figind);
        vortz2=reshape(vortz3d(:,yindplt,:),zind,Xind);
        contourf(xposadj,zposadj,vortz2,10);
         caxis([-600 600]);
        colorbar;
        axis equal;
        xlim([min(xposadj) max(xposadj)]);
        ylim([min(zposadj) max(zposadj)]);
        title(['Z-vorticity contour at y/d = ',num2str(yposadj(yindplt)),' Looking in
positive y direction.']);
        xlabel('x/d');
        ylabel('z/d');
        figind=figind+1;

    % Plot x-component of vorticity
        figure(figind);
        vortx=reshape(vortx3d(:,yindplt,:),zind,Xind);
        contourf(xposadj,zposadj,vortx,10);
        caxis([-1200 1200]);
        colorbar;
        axis equal;
```

```
        xlim([min(xposadj) max(xposadj)]);
        ylim([min(zposadj) max(zposadj)]);
        title(['X-vorticity contour at y/d = ',num2str(yposadj(yindplt))]);
        xlabel('x/d');
        ylabel('z/d');
        figind=figind+1;
    end

% 3D plotting
  else
    vcomp=[];
    fprintf('\nSelect a velocity or vorticity component for plotting:\n');
    vcomp=input('  1=u, 2=v, 3=w, 4=vortx, 5=vorty, 6=vortz <1>: ');
    if isempty(vcomp)
      vcomp=1;
    end
    dat3d=[];
    if vcomp==1
      dat3d=Uvel;
      titstr='u/Uinf';
      unitstr=' m/s.';
    elseif vcomp==2
      dat3d=Vvel;
      titstr='v velocity';
      unitstr=' m/s.';
    elseif vcomp==3
      dat3d=Wvel;
      titstr='w velocity';
      unitstr=' m/s.';
    elseif vcomp==4
      dat3d=vortx3d;
      titstr='x vorticity';
      unitstr=' 1/s.';
    elseif vcomp==5
      dat3d=vorty3d;
      titstr='y vorticity';
      unitstr=' 1/s.';
    else
      dat3d=vortz3d;
      titstr='z vorticity';
      unitstr=' 1/s.';
    end

    fprintf('The maximum in the domain is %6.3f.\n',max(max(max(dat3d))));
    fprintf('The mean in the domain is %6.3f.\n',mean(mean(mean(dat3d))));
    fprintf('The minimum in the domain is %6.3f.\n',min(min(min(dat3d))));
```

```
    vval=[];
    vval=input('Enter a number between these bounds: ');
    ansb=[];
    ansb=input('Plot with new figures or overwrite <new>? ','s');
    if isempty(ansb)
       ansb='n';
    end
    if ansb~='n'
       figind=2;
    end
% The datablock will be traversed from the freestream toward the wall to find the first
       point at which the velocity value is crossed.
% The resulting matrix will contain the y-elevation of the crossing point or "0" if there
       was no crossing.
    yst=[];
    fprintf('The y/D data extends from %6.3f to %6.3f:\n',yposadj(1),yposadj(yind));
    yst=input('Enter a starting place for the surface scan to the wall <max>: ');
    if isempty(yst)
       yst=yind;
    else
       [dum,yst]=min(abs(yposadj-yst));
    end
    ysep=walloff/holediam;
    datsurf=ones(Xind,zind);
    datsurf=datsurf*ysep;
    for i=1:zind
       for k=1:Xind
          vdum=dat3d(i,yst,k);
          vdumi=vdum;
          for j=yst-1:-1:1
             vchk=dat3d(i,j,k);
             if (vdum>=vval & vchk<vval) | (vdum<vval & vchk>=vval)
                datsurf(k,i)=yposadj(j+1)+(vval-vdum)*(yposadj(j)-yposadj(j+1))/(vchk-
vdum);
                break
             end
             vdum=vchk;
          end
       end
    end

    figure(figind);
    surf(zposadj,xposadj,datsurf);
axis equal;
caxis([0 10]);
zlim([0 10]);
```

```
title(['Surface of ',titstr,' = ',num2str(vval)]);
xlabel('z/d');
ylabel('x/d');
zlabel('y/d');
figind=figind+1;
end

      ansc=[];
      ansc=input('Do you want another plot, y/n <y>? ','s');
      if isempty(ansc)
         ansc='y';
      end
      if ansc=='n'
         ansa='n';
      end
end

% Allow writing of spanwise averaged u data if desired
   ansb=[];
   ansb=input('Do you want to write the spanwise averaged u data to a file? <n>','s');
   if isempty(ansb)
      ansb='n';
   end

   if ansb=='y'
      datout=uinf*reshape(mean(Uvel),yind,Xind);
      fprintf('\nPrinting to file...\n');
      filido=[];
      filido=fopen([fileprefd,'Spanavg.txt'],'w');
      for i=1:yind+1
         if i==1
            fprintf(filido,'\ndatablock\t');
         else
            fprintf(filido,'\n%6.3f\t',yposadj(i-1));
         end
         for j=1:Xind
            if i==1
               fprintf(filido,'%6.3f\t',xposadj(j));
            else
               fprintf(filido,'%6.3f\t',datout(i-1,j));
            end
         end
      end
      fclose(filido);
   end
```

```
   % Allow writing of spanwise averaged Vmag/Uinf data if desired
   ansb=[];
   ansb=input('Do you want to write the spanwise averaged Vmag/Uinf data to a file?
<n>','s');
   if isempty(ansb)
      ansb='n';
   end

   if ansb=='y'
      datout=reshape(mean(Vmag),yind,Xind);
      dlmwrite([filepref,'Vspanavg.txt'],datout,'\t');
       datout=reshape(mean(Vmag),yind,xind);
       fprintf('\nPrinting to file...\n');
       filido=[];
       filido=fopen([filepref,'Vspanavg.txt'],'w');
       for i=1:yind+1
          if i==1
             fprintf(filido,'\n\t');
          else
             fprintf(filido,'\n%6.3f\t',yposadj(i-1));
          end
          for j=1:xind
             if i==1
                fprintf(filido,'%6.3f\t',xposadj(j));
             else
                fprintf(filido,'%6.3f\t',datout(i-1,j));
             end
          end
       end
       fclose(filido);
   end
```